Towards high throughput mechanical testing of cells for diagnostics and therapy

Maryam Mohammad Zadeh

Submitted for the degree of Doctor of Philosophy

Heriot-Watt University

School of Engineering and Physical Sciences

May 2017

ABSTRACT

This thesis will focus on the modelling and quantification of the mechanical properties of biological samples with the aid of Atomic Force Microscopy (AFM). The importance of studying the mechanical properties of biological samples lies in its potential use for both therapeutic and diagnostic research as well as in bioengineering fields such as designing/selecting appropriate cell sorting and separation techniques.

First part of this thesis is focused on developing a mathematical model by considering the physical properties (size and membrane thickness) of cells, to measure the size changes and Young's elastic modulus of mammalian cells. Developed model showed promising results in measuring the changes in the radius of the cells after deformation. Also, it has been showed that there is a direct relation between the shape of the indenter and obtained elastic modulus. Moreover, the Young's elastic modulus derived from fitting the developed model into force-indentation curves was in the range of MPa. This is due to measuring the elastic properties of cells on the surface elements (lipid bilayer).

Producing manufactured red blood cells (RBCs) is increasing due to the high demand for blood transfusions and lack of eligible donors. Manufactured RBCs require continuous sorting and separation process during their production, as well as at the end of the manufacturing process, where reticulocytes are formed. Selecting appropriate sorting and separation methods, which are highly efficient and have the minimum drawback, is essential. Techniques which are carry out the cell separation processes based on the mechanical and physical properties of cells shows promising results. Therefore, the second part of this thesis was designed to measure the mechanical and physical properties of CD34+ stem cells during their expansion and differentiation processes (Days 11, 14, 18 and 21) for cell purification and separation purposes. Obtained results showed that size-based techniques can be applied to sort cells at day 11 of differentiation process from the day 14, while for sorting day 14 cells from day 18 and day 18 cells from day 21, any elasticity or sized based techniques cannot provide a highly purified/sorted culture and significant contaminations would be remained. In addition, the mechanical properties of the extruded nucleus from the CD34+ cells was also quantified for studying their effects on the elastic properties of the CD34+ cells. Derived results showed that to eliminate the free-floating nucleus form the culture media, elasticity and size-based techniques can be used and provide a high efficient sorted culture (100% separation).

ACKNOWLEDGMENTS

I would like to express my sincere gratitude to my supervisors Prof Nik Willoughby and Dr Henry Bock for giving me the opportunity to pursue my PhD, for their continuous support of my PhD study and related research, for their patience, motivation and immense knowledge. Their guidance helped me in all the time of research and writing of this thesis. I could not have imagined having better supervisors for my PhD study. Thanks Nik and Henry.

Besides my supervisors, I would like to thank Dr Fiona Dempsey, for providing the biological samples and the insightful advices offered by her.

I would like to thank the Edinburgh Super-Resolution Imaging Consortium (ESRIC) for the research facilities and Dr Alison Dun for her help with the Atomic Force Microscopy.

I had the opportunity to share the time as a PhD student with the fantastic people in EPS department. Thanks Jessica, Nisha, Javier, Behnam, Ewa, Sorush, Mahmood and Atabak for your helps.

Last, but not least I would like to thank my family for their unconditional support and patience.

DEDICATION

To my family, Mahmoud Mohammad Zadeh, Mozhgan Mirzaei and Mahyar Mohammad Zadeh and to my husband Amir Deylaminezhad.

ACADEMIC REGISTRY
Research Thesis Submission

Name*:*	Maryam Mohammad Zadeh		
School:	Engineering and Physical sciences		
Version: *(i.e. First, Resubmission, Final)*	Final	Degree Sought:	Ph.D. Physics

Declaration

In accordance with the appropriate regulations I hereby submit my thesis and I declare that:

1) The thesis embodies the results of my own work and has been composed by myself
2) Where appropriate, I have made acknowledgement of the work of others and have made reference to work carried out in collaboration with other persons
3) The thesis is the correct version of the thesis for submission and is the same version as any electronic versions submitted*.
4) my thesis for the award referred to, deposited in the Heriot-Watt University Library, should be made available for loan or photocopying and be available via the Institutional Repository, subject to such conditions as the Librarian may require
5) I understand that as a student of the University I am required to abide by the Regulations of the University and to conform to its discipline.
6) I confirm that the thesis has been verified against plagiarism via an approved plagiarism detection application e.g. Turnitin.

* *Please note that it is the responsibility of the candidate to ensure that the correct version of the thesis is submitted.*

Signature of Candidate*:*		Date:	06.09.17

Submission

Submitted By *(name in capitals):*	MARYAM MOHAMMAD ZADEH
Signature of Individual Submitting:	
Date Submitted:	

For Completion in the Student Service Centre (SSC)

Received in the SSC by *(name in capitals):*			
Method of Submission *(Handed in to SSC; posted through internal/external mail):*			
*E-thesis Submitted (**mandatory for final theses**)*			
Signature:		Date:	

LIST OF PUBLICATIONS

Journal Publications

1. **Mohammad Zadeh, M.,** Guzniczak, E., Dempsey, F., Jimenez, M., Bock. H., Whyte. G., Bridle, H., Willoughby, N.A., High-throughput assessment of mechanical properties of stem cell derived red blood cells, toward cellular downstream processing. Journal of Scientific Reports. *Submitted*.

Conferences and Presentations

1. **Mohammad Zadeh, M.,** Willoughby, N.A., Bock. H., Exploiting elastic modulus of human cells for separation purposes. *10th International Conference on Advances in Experimental Mechanics*, Edinburgh, UK, 2015.

TABLE OF CONTENTS

LISTS OF FIGURES

LISTS OF TABLES

LISTS OF ABBREVIATIONS

AFM	Atomic Force Microscopy
AIDS	Acquired Immune Deficiency Syndrome
DMT	Derjaguin, Muller and Toporov
FACS	Fluorescent-Activated Cell Sorting
GMP	Good Manufacturing Practice
HBSS	Hank's Balanced Salt Solution
hESCs	human Embryonic Stem Cells
hiPSCs	human-induced Pluripotent Stem Cells
JKR	Johnson, Kendall and Roberts
MACS	Magnetic-Activated Cell Sorting
PBS	Phosphate Buffer Saline
QI	Quantitative Imaging
RBCs	Red Blood Cells
SEM	Scanning Electron Microscopy
STM	Scanning Tunnelling Microscopy

CHAPTER 1

Introduction and Literature review

Contents

1.1 Introduction

This Chapter will explain the background theory and experimentation upon which this work is based, beginning with an overview of the Atomic Force Microscopy (AFM), its operational principals and applications in measuring mechanical properties of living cells. The different mathematical models currently used to calculate the mechanical properties of the materials will also be discussed, along with the importance of the cell elasticity and

methods for measuring elasticity. Lastly, the motives and outline for this thesis will be addressed and described in relation to the significance of this research field.

1.2 Atomic Force Microscopy (AFM)

Atomic Force Microscopy (AFM) was first introduced by G. Binnig, C. F. Quate and Ch. Gerbe [1] as a combination of the principles underpinning the scanning tunnelling microscope (STM) and the stylus profilometer, with the added advantage of being able to operate at an atomic scale. In 1983, Gerd Binnig along with Heinrich Rohrer, introduced the first scanning tunnelling microscopy, whose function was to monitor the current of electrons passing between a scanning conductive tip, passing over a conductive sample, to resolve the surface structure of the sample at atomic scale [2]. However, as the conductivity of the sample was one of the important requirements of this technique, the obtained results were not accurate. Understanding the problem, which is a sample with conductivity properties and applying the scanning tunnelling microscope and the stylus profilometer principles, AFM was invented later in 1986. Due to the atomic scale at which AFM can operate, numerous biological studies have been carried to investigate and probe the various biological properties of soft biological samples. AFM has enabled biologists to study the nanomechanical properties of a wide range of biological samples such as DNA, RNA, cell proteins, phospholipids, and subcellular structures such as cell organelles within living mammalian cells and tissues [3, 4].

AFM technology has a wide range of applications in research and development. As a method, it can be used to study the mechanical, electrical and magnetic characteristics of samples both qualitatively and quantitatively [5]. It has been used to image and visualize sample surfaces both in the air and in liquid environments. Therefore, it enables the technique to be used in chemical and bioengineering researches [6-8]. Furthermore, AFM can produce three-dimensional images with near atomic level image resolutions, thus allowing for the quantification of specific sample surface properties such as surface roughness, morphology, elasticity and surface adhesion in their *in vitro* conditions [9]. Moreover, AFM has become highly useful for medical applications where small nano amounts of selected drug therapies can be deposited into target organs for pharmaceutical research [10]. Also, AFM can provide the high resolution topography of the cells and can be used to study the mechanical properties of the tissue cells [11].

1.2.1 AFM operational principles

The principle of AFM operation is based on the detection of repulsive and/or attractive forces present on the surface of a given sample. It is comprised of a probe positioned at the end of a reflective cantilever, which is controlled to move over the surface of a chosen sample, employing a piezoelectric actuator to convert electrical energy directly into linear motion (Fig. 1-1). The interaction between the sample surface and cantilever tip (probe), corresponds to the force between the atoms on the surface of the sample and those of the probe that scans its surface [12]. The cantilever is a key element in the operation of AFM. A cantilever generally contains one or more beams of silicon and/or silicon nitride with 100–500 μm lengths, ranging from 0.5–5 μm in thickness. Depending on the sample type, the selected cantilever probe should be thin and durable under the selected applied forces, and should not bend or fracture under normal forces. The cantilever and underlying probe are generally composed of the same material, and are available as either planar or triangular shapes. The available cantilever shapes are designed to allow for a greater level of flexibly and material strength, as well as optimal probe placement and secure adhesion to the cantilever [8]. The interaction between the sample surface and cantilever probe is dependent on the variation in distance between them. The interaction of the probe with the sample results in cantilever deflection, the extent of which is dependent on the surface topography of the sample. The tip-sample interaction is monitored by a laser beam reflected off the back of the cantilever toward a photodetector photodiode. The distance between the probe and the sample is kept at a certain target height value by connecting a feedback circuit to the cantilever deflection sensor. If the height of the probe changes over the sample surface, the cantilever deflections would cause variation in the applied force from the probe to the sample. As this is not desirable (for most AFM assays) the AFM uses a feedback circuit mechanism to keep the force between the cantilever probe and the sample equal. The signal feedback from the AFM indentations forms a two-dimensional matrix, which is then translated into a three-dimensional image of the samples surface (Fig. 1-1). To keep the laser beam within the margins of the receiving photodiode detector, a voltage equal to or exceeding the reflected cantilever voltage is required to change the height of the piezo, such that the acquired image of the sample surface can be constructed from each indentation point for each raster scan line. The internal AFM feedback, monitors this voltage in relation to the cantilever deflection and adjusts the z-piezo to maintain at the desired force set-point. Therefore, the scan height over the sample can be adjusted as the z-piezo height changes, which results in the rapid reaction of the

AFM towards the changes in the samples surface, thus keeping the applied force constant. This mode of operation decreases the amount of damage on the samples surface, as well as elongates a cantilever probes integrity and usage [13].

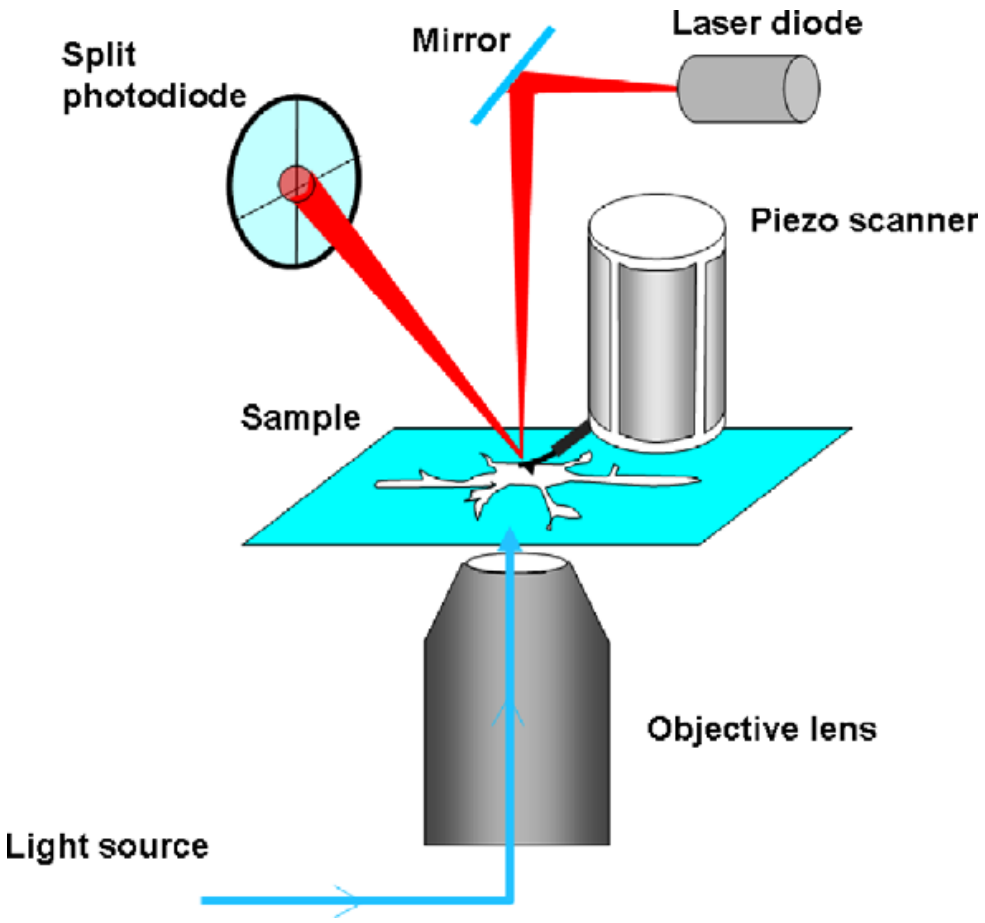

Figure 1-1. AFM operation schematic. A cantilever probe indents a sample, results in the deflection of the cantilever and thus deflection of the reflected laser beam detected by the receiving photodiode. The deflection is the processed and the deformation of the sample analysed for surface imaging or mechanical measurements [13].

One of the important applications of the AFM is the characterization and surface topography imaging of biological samples in an *in vitro* environment. In an AFM experiment, biological samples can be imaged in culture media at an appropriate temperature and CO_2 concentration. Furthermore, high resolution images of the biological samples can be obtained without the need for sample fixing, staining and/or labelling. Images from the AFM can be presented in three-dimensions with high accuracy, providing information about the height, adhesion and slope of an imaged sample in each image. However, high resolution images (i.e. 512×512 pixels) require more time to complete, around 2630 minutes. During this extended time, many physical and chemical changes can occur to the sample, particularly for live cell samples, where cell movement

and cell death can occur soon after removal from a controlled culture environment. Moreover, accumulation of debris around the cantilever probe can effect shape, sharpness and function, which as a result, will not produce the desired image resolutions required [14]. To solve this problem many efforts have been made to improve high resolution scan times by applying high speed scanners, faster amplitude detectors, faster electronic processors and smaller cantilevers. However, faster AFM scanners can only be used for non-biological materials, due to larger dimension cantilevers required with low resonant frequencies [15]. Moreover, most AFM microscopes have limited scan ranges, set at 100µm in the x and y axes and 15µm in the z axis. Lastly, AFM imaging modes are limited to imaging the sample surface, and are not able to provide topographical information on any of the internal components of a chosen sample.

Despite the abovementioned limitations, AFM is one of the most useful methods in the scanning probe microscopy family. Some of the AFM advantages include the ability of being able to measure more than one aspect of a sample during a single indentation experiment, providing mechanical information of the sample, alongside generating a high-resolution image of the samples surface. Generated AFM images are highly dependent on the size and geometry of the underlying cantilever probe as well as the applied imaging force, AFM resolution goes in to the electron microscopy rang. Therefore, AFM can provide atomic level resolution in the highly controlled conditions [16].

1.2.2 AFM operational modes

An AFM has a number of different operational modes, making it a superior form of scanning probe microscope. The operational modes available are (1) contact mode, (2) non-contact mode and (3) tapping or intermittent mode. The operational mode chosen is selected based on the sample, sample environment and the type of measurement required [17]. In this research thesis, the mode of operation selected were contact mode force mapping and quantitative imaging (QI). Both modes were used to investigate and measure the mechanical properties of living cells. Although, contact mode is not always the best option for imaging biological samples, given that the main focus of this research was the measurement of the mechanical properties of the living cells, high resolution images of the living cells was obtained using the QI tool in the AFM contact mode. Here, we only detailed this mode of operation because it was the primary mode we used for all the experiments.

1.2.2.1 Contact mode

Contact mode is the most direct imaging and force spectroscopy mode, which can be carried out in both air and fluid. In this mode, the applied force on the cantilever is kept constant, with the AFM probe and sample surface brought into contact with each other. As the probe moves over the sample surface, the interaction between the probe and sample changes as a result of surface topography variations. Changes in the cantilever deflection are detected by the photodiode deflection of the laser beam and the information feedbacks to the piezoelectric scanner. In this mode, the applied force is never within the magnitude of damaging the living cells, however, it is enough to detect the structures of the cell underlying the plasma membrane [8]. The cantilevers used for this mode must be extremely flexible and soft to image and/or indent living cells. For this purpose, silicon or silicon nitride cantilevers are mainly chosen. Other important issue is the effect of capillary force when the experiments run in the air. Capillary forces are the result of the presence of a thin layer (known as the fluid layer) of fluid containing condensed water vapour and other atmospheric contaminants, coating all surfaces in the air [18]. The absorbed water molecules can form a thin layer on the sample surface so as the tip reaches to the surface meniscus can be form, which in turn can cause an attractive force between the tip and the sample known as the capillary force. Therefore, for imaging the biological samples in the air, contact mode is not the best option while the tapping mode (also known as intermittent contact mode) is the preferred choice instead. This mode provides the oscillating cantilever tip near its natural resonance frequency with the minimum impact of the tip on the sample. When the cantilever reaches to the resonant frequency, the probe starts to contact with the sample. Images can be obtained by monitoring the changes between the tip and the sample distance, which can result in the changes in the oscillation amplitude of the cantilever. In this technique the lateral forces are reduced and the energy loss from tip-sample contact naturally generates an amplitude loss, which is measured and used to identify surface features [8].

1.2.2.2 Force spectroscopy

AFM force spectroscopy mode is designed to perform force-distance measurements at micro and nano length scales. It can provide information about the elastic properties of a biological sample under *in vitro* culture conditions. In this mode, the z position of the cantilever is scanned while the lateral position (x and y) is set at a fixed point. Vertical movements of the cantilever probe towards and against the surface results in indentation

of the sample surface and each completed extend-retract cycle produces a force-displacement curve (Fig. 1-2) [19].

One of the more important applications of this technique is to provide information aim at a greater understanding of mechanical properties of cancer cells and the mechanisms controlling their metastasis and differentiation. Other fundamental behaviours of living cells, such as cell division, senescence and apoptosis can also be studied by monitoring the mechanical changes in cell elasticity, which are mainly attributed to the cells cytoskeleton. These changes can be used as a marker for abnormal cell behaviour in various disease processes [20, 21].

In this work, force-indentation curves were obtained by indenting live cell samples with conical shaped probes, and deriving the elastic modulus of the measured cells by fitting the derived curves with the appropriate mathematical contact models. For elastic modulus calculations, the applied force, geometry of the probe and cantilever spring constant are required to accurately calculate the elastic modulus of cell sample.

1.2.2.2.1 Force mapping

Force mapping is an extension of the force spectroscopy mode, which incorporates high spatial resolution force map indexes and performs force-displacement measurements at specifically selected points across the surface of a chosen sample. Each map is constructed from an array of pixels, referred to as a force map "index". Every index within a force gathered force map provides a single force-displacement curve, from which the elastic modulus can be derived for each point of indentation. The force mapping index size can be selected to be a minimum size of 8×8 and up to maximum size of 128×128 indexes. Performing force mapping on living cells enables the user to identify the stiffer regions corresponding to the intracellular organelles such as the cell nucleus (Fig. 1-3) [22]. All acquired force maps are presented in two-dimensional and represent the stiffness of the mapped sample, and is independent of any AFM topographical image.

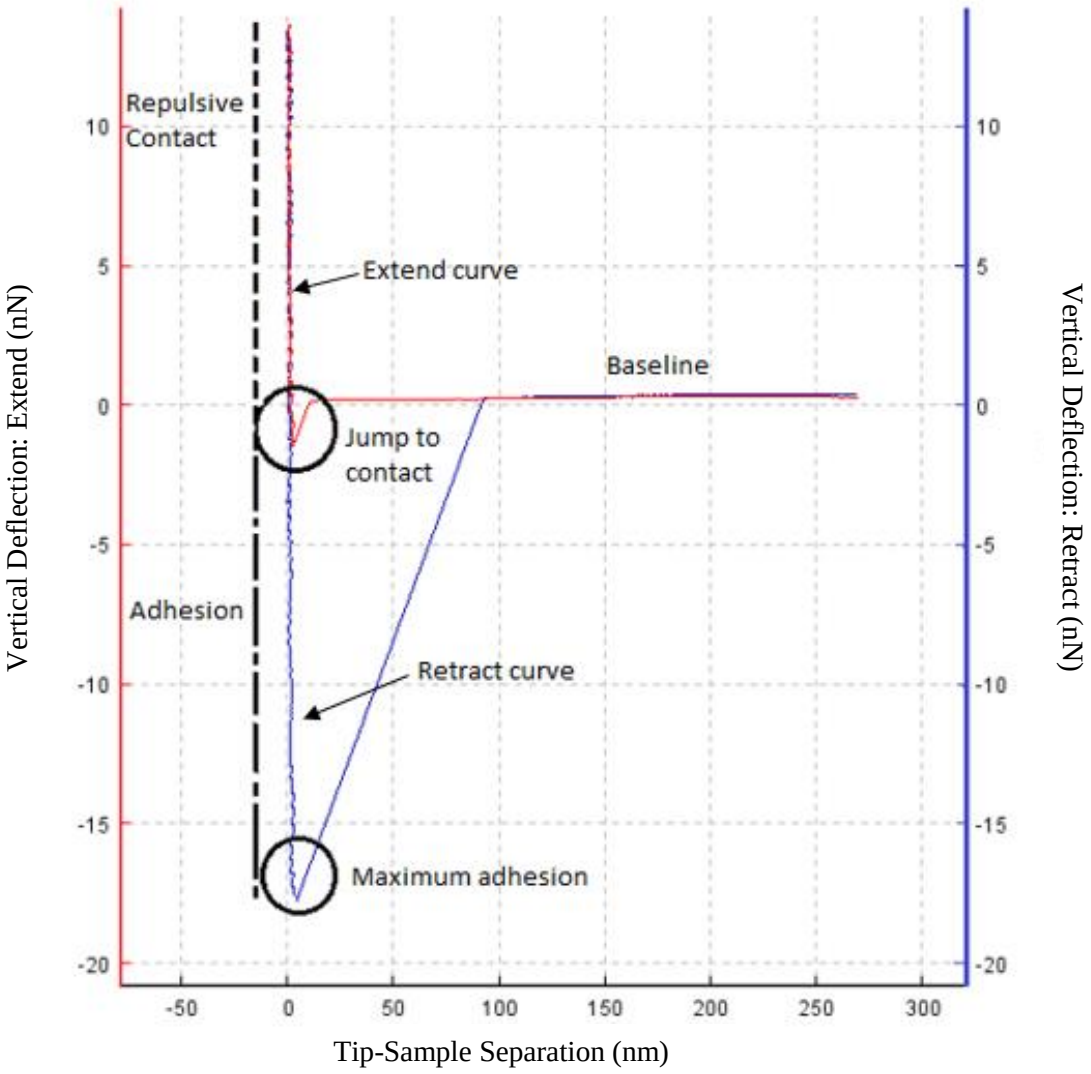

Figure 1-2. Single force-indentation curve obtained from indenting a glass substrate with a conical tip cantilever in the air. The part of the curve labelled baseline illustrates that there is no force between the tip and surface of the sample (force is equal to zero) so this region should generally be linear along the x-axis. However, the vertical deflection along the y-axis is not equal to zero due to environmental factors (e.g. debris in the media or viscosity of the media) and/or deflection of the cantilever was not set exactly to zero. The reason that the x-axis is labelled as tip-sample separation is due to height signal for the bending of the cantilever has been corrected. It means that the deflection of the cantilever has been removed from the height signal, and only the movement of the cantilever towards the sample was taken in to account. The small jump on the extend curve, shown circled in black, is the result of the capillary forces from the liquid media surrounding the sample. Also, the maximum adhesion, shown circled in black, is the point before tip can be retracted from the sample surface [23].

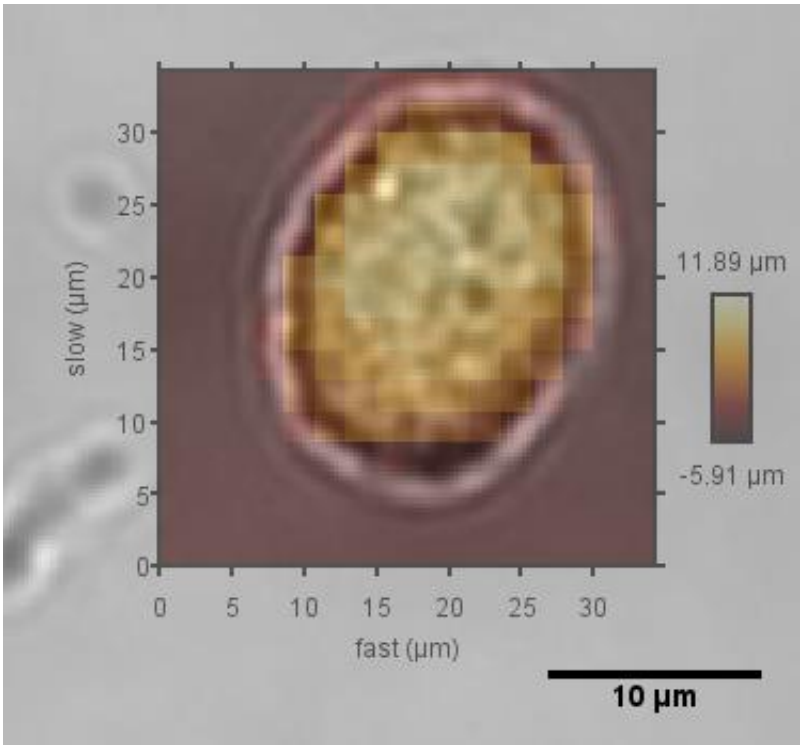

Figure 1-3. An example of an acquired force mapping image for a murine J774 macrophage cell. Overlaying the two AFM images makes it possible to observe and investigate the different intracellular regions with varying stiffness's across a cell. In this image, the lighter index squares, represent the highest region of the cell following indentation, which may likely be the cell nucleus. The gridded square in the centre of the image represents the force map and the Young's modulus values can be obtained from each index. In this example 35×35µm grid used to produce the force map, however resolution can be increased or decreased by choosing the larger or smaller grids for the force mapping.

Force-indentation curves obtained from force mapping live cells in liquid are slightly different in shape from the ones obtained on a glass substrate (Fig. 1-2). The gradient of the approach curve obtained in liquid is smoother and there is a gap between the baseline portions of the extend and retract curves, due to the viscosity of the liquid media (Fig. 1-4). Furthermore, working in liquid can cause some noise fluctuations in the force indentation measurements, which is due to the thermal fluctuations arising from the heating stage of the liquid media. These fluctuations produce small pulses of force waves in the liquid media. The severity of the thermal fluctuations can vary based on the liquid temperature of the cell media, and the spring constant of the cantilever (soft cantilevers can produce a greater amount of noise fluctuations) [24].

Force curves obtained during a force-indentation experiment typically have four important parts/sections, each of which provides important information about the operation of the cantilever and force-indentation experiment. As illustrated by Fig. 1-4 the four main parts of a force-indentation curve are:

1- The approach portion: in this portion of the curve, the cantilever moves toward the surface of the sample, and there is no contact of the probe with the samples surface. For measurements carried out in liquid media, some thermal fluctuations and/or viscous forces can be observed.
2- The deflection portion: immediately after the tip contacts the surface of the sample, the cantilever probe is deflected. In this portion of the curve, the cantilever probe is in repulsive contact with the surface of the sample and is pushing/indenting into the surface of a soft biological sample.
3- The retracting portion: due to the maximal indentation force, always being defined at the beginning of the indentation approach, as the defined maximal force set point is reached, the cantilever stops the indentation and retracts away from the sample surface.
4- The adhesion portion: due to the presence of adhesion between the sample surface and the cantilever probe (this is common in live cells due to protein binding and adhesion to the cantilever probe), as the tip is retracting from the surface of the sample, complete retraction is delayed due the strength of the adhesion forces.

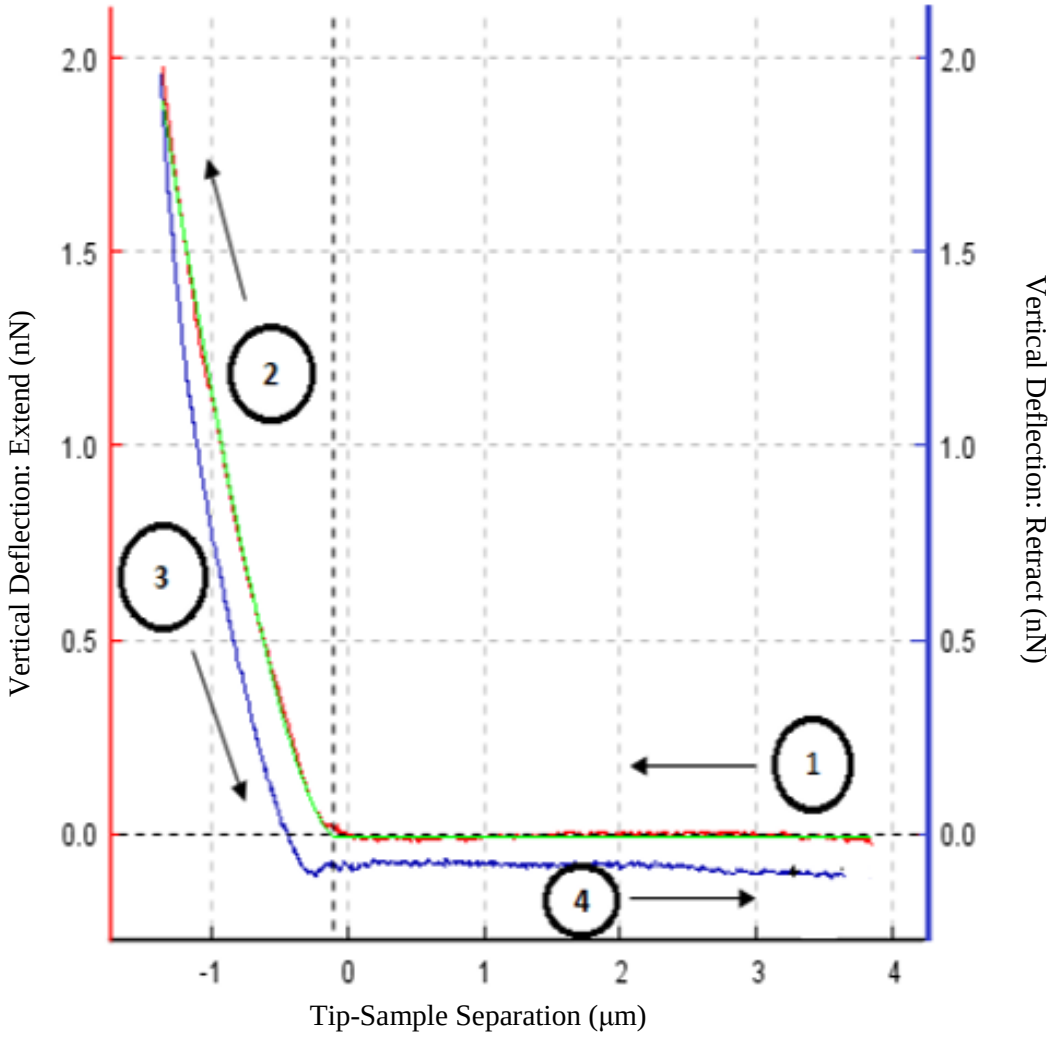

Figure 1-4. Force-indentation curve obtained from a live J774 mouse macrophage cell in liquid media at 37°C. Performing a force-indentation experiment in liquid media can increase the occurrence of hysteresis along the baseline portion of the force curve, due to the thermal fluctuations that occur as a result of the liquid warming bio chamber. Furthermore, the viscosity of the liquid can induce hydrodynamic drag on the cantilever, which inhibits the approach and retract portions of the force curves from returning to do the 'zero' point/force. Here, the numbered parts are 1- the approach portion, 2- the deflection portion 3- the retracting portion 4- the adhesion portion and the green curve represents the mathematical model fitted in to the extend curve to derive the Young's elastic modulus. The Hertz-Sneddon contact model is applied in this example.

1.3 Models of contact mechanics

Geometrical effects on local elastic deformation properties have been considered since the 1800's with the Hertz Theory of "Elastic Deformation" first published in 1880. This theory relates the circular contact area between two spheres to the elastic deformation properties of the two spheres material properties. In this theory any surface interactions, such as Van der Waals interactions, or work of adhesion are neglected [25, 26]. The "Elastic Deformation" paper was the first research in the elastic contact mechanics and soon Hertz founded the contact mechanics field theorem, which has retained a small but

loyal following during the past one hundred years. Further developments in the contact mechanics field was carried out by Sneddon who considered the shape of the indenter that contacted with the opposing material body. In doing so, he modified the Hertz contact model to include contact model theorems for flat-ended cylindrical probes, conical, pyramidal and paraboloid shaped probes [27].

The Hertz theory was improved by Johnston, Kendall and Roberts in 1971 with the JKR theory. In this theory, adhesion forces in the contact area between the two materials were considered in their calculations. The adhesive contact between the two materials results from formation the contacts at the time of unloading or in the negative loads. JKR theory is restricted to elastic sphere contact models [28].

Another theory derived in the field of contact mechanics was the DMT theory, published by Derjaguin, Muller and Toporov [29]. In this theory, the Van der Waals interactions outside the elastic contact regime are also considered, which results in additional load.

The elastic shell theory is another contact model developed in the field of contact mechanics. In this research work, we use this theory to develop a new model for measuring elastic properties and size changes in the biological samples.

1.3.1 Hertz model

Great strides have been made in the modelling of the contact between two elastic solids since the theory was first established by Heinrich Hertz in 1881. In his initial study, Hertz investigated the contact mechanics between two bodies by modelling the elastic deformation of the surface of two glass lenses based on the contact pressure between them. He presented his theory in the paper "On the contact of elastic solids" [25]. In the paper, Hertz made the initial hypothesis that the contact area between the two bodies is elliptical. He then went on to simplify the calculation for the deformed area, and made the assumption that each of the bodies can be exist as an elastic half-space (there were already well developed methods available to solve the boundary value problems of the elastic half-space bodies in contact with each other) loaded over a small elliptical region of its plane surface. Considering each of the bodies as an elastic half-space, results in a highly-concentrated stress in the contact region of the two bodies treated separately from the other stresses, which exist in the bodies due to their shape and the way they are supported. To apply the simplification, two conditions were required: dimensions of the contact area must be smaller than 1- the dimensions of each body 2- the relative radii of

curvature of the surface. The first condition is necessary to make sure that the general distribution of stresses in the bodies, are not influenced by the highly-stressed regions in their vicinity. The second condition is required for two reasons; first, to confirm the regions outside the contact region are approximately half-space and not spherical. Secondly, when fitting the model for the linear theory of elasticity, it is necessary to ensure that the strains in the contact region are sufficiently small. Furthermore, as an additional simplification, both bodies surfaces are assumed to be frictionless, with only the applied force from the indenter (which is parallel to the z-axis) taken in to the consideration [26].

To summarise the Hertz theory assumptions and present the equations that he derived using the assumptions, we need to introduce and define the parameters used in the Hertz model calculations. The parameters given the Hertz contact model equation are: The radius of the contact area between the two bodies [a], the indentation depth [δ] of the indenter, which are both related to the applied force [F], and the radius of the spherical indenter [R] (Fig. 1-5) [25, 26].

The assumptions made by Hertz to simplify the calculations can be summarised as:

1- Each body can be considered as an elastic half-space
2- The surfaces are continuous and non-conforming (which implies that the area of contact is much smaller than the characteristic dimensions of the contacting bodies): $a \ll R$
3- The strains are small: $a \ll R$
4- There is no friction between the two bodies, and only a normal applied force is transmitted between them

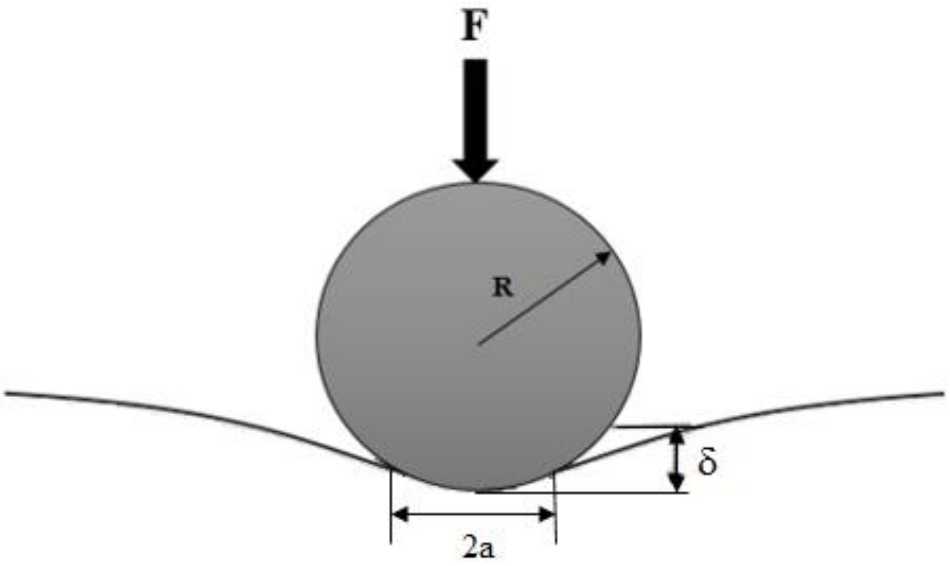

Figure 1-5. Schematic of the Hertz model. Contact between two continuous, non-conforming bodies under the action of an external force [F]. The initial shape of the contact area is a point or line, but after the deformation, the shape will be circular, with a contact radius of [a] and indentation depth of [δ].

For an elastic half-space deformed with a spherical solid, Hertz showed that the shape of the contact area is circular with a radius of [a], which can be calculated by:

$$a = \left(\frac{3FR}{4E^*}\right)^{\frac{1}{3}} \tag{1-1}$$

Additionally, the indentation depth is derived by:

$$\delta = \frac{a^2}{R} = \left(\frac{9F^2}{16RE^{*2}}\right)^{\frac{1}{3}} \tag{1-2}$$

Using and rearranging Eq. (1-2), the total force applied externally to compresses the two bodies, can be obtained as:

$$F = \frac{4ER^{\frac{1}{2}}}{3(1-\nu^2)}\delta^{\frac{3}{2}} \tag{1-3}$$

Where in all of the above equations, E* is:

$$\frac{1}{E^*} = \left(1 - \frac{\nu_1^2}{E_1}\right) + \left(1 - \frac{\nu_2^2}{E_2}\right) \tag{1-4}$$

E and ν are the Young's modulus and the Poisson's ratio respectively [26].

It should be noted that different contact models have been further developed based on the Hertz model theorem, for the purpose of analysing the Young's modulus of samples where the experimental and/or sample conditions do not meet the requirements of the original model. For example, for samples where the surface-adhesion of the sample is being measured, the geometry of the indenter, as well as thickness of the sample, need to be taken into consideration. These developments and modifications to the original contact model, are important for most of the biological samples, especially for living cells where the assumptions in the Hertz contact model cannot be applied [30].

Since the Hertz model contains the fundamental principles of the contact mechanics between two bodies, many of the modified models for elastic measurements are based on it. Although the Hertz model is designed for elastic bodies, it can also be applied for viscoelastic samples, and is also a suitable model for analysis the thick regions of a cell sample, such as the nuclear and perinuclear regions and shallow indentations (<10% of total sample thickness) [31].

As mentioned previously, Sneddon considered the shape of the indenter that contacted with the opposing material body and modified the Hertz model for different probe shapes.

1.3.1.1 Hertz-Sneddon model

The studies carried out by Hertz in the field of contact mechanics, provided the foundation for most of the experimental and theoretical works developed later in the field of contact mechanics. One such development has been further research carried out investigating the variances in mechanical outputs based on the geometry of the cantilever probe indenter. Based on the principles of the Hertz model, Ian. N Sneddon studied the relationship between load, displacement and contact area of the probe indenter, which were the solids of revolution. His studies lead to an equation which can be applied for the calculation of the applied load when using indenters of different geometrical shapes [27].

For flat-ended cylindrical indenters, the relation between load and displacement is given as:

$$F = \frac{2ER}{(1-\nu^2)}\delta \tag{1-5}$$

Where E is the elastic Young's modulus, R, is the radius of the indenter, ν is Poisson's ratio and δ is the indentation depth.

For the conical indenters, the equation given as:

$$F = \frac{2E \tan \alpha}{\pi(1-\nu^2)}\delta^2 \tag{1-6}$$

Here, all parameters are the same as above, with α as the half angle of the cone.

In the case of a spherical indenter, the equation is modified as:

$$F = \frac{E}{1-\nu^2}\left[\frac{a^2+R^2}{2}\ln\frac{R+a}{R-a} - aR\right] \tag{1-7}$$

Where a is the radius of contact sphere, and R is the radius of the sphere.

Finally, for a four-sided pyramidal indenter, the equation given as:

$$F = 0.7453\frac{E}{1-\nu^2}\,\delta^2 \tan \alpha \tag{1-8}$$

Here α denotes the face angle of the pyramidal indenter.

The results obtained from Sneddon's calculations, revealed that for many indenters with different geometries, the relationship between force and displacement can be described as:

$$F = A\delta^B \tag{1-9}$$

A and B are material constants.

Given that, Sneddon modified the Hertz contact model and developed it for different indenter geometries, the modified contact model is known as the Hertz-Sneddon model, and is regularly applied in studying the mechanical properties of various materials.

As mentioned previously in the Hertz model, the adhesion between two contacted surfaces are neglected, but further experimental studies have shown that although these adhesion forces are not significant at high forces, at the low forces (as it tends to zero), they become significantly important, and cannot be neglected [32]. As a result, the Hertz

model was further developed by Johnson, Kendall and Roberts, to produce the JKR theory, which considers the variation in adhesion forces between the contacted bodies.

1.3.2 JKR theory

Further studies by Johnson and colleagues in 1971, showed that under low forces the contact area between two bodies were significantly larger than that predicted by the Hertz model [28]. Also, as the forces were decreasing to zero the contact area was tended towards a constant finite value. This force, which was later discovered to be the adhesion force between the two bodies, resulted in development of the Hertz model. So, JKR theory developed by applying the adhesion forces between a rigid sphere and a rigid plane.

A rigid sphere with a radius [R] that is in contact with a rigid surface, the adhesion force [F_A] between the two surfaces can be calculated from:

$$F_A = 2\pi\Delta\gamma R \tag{1-10}$$

To separate the two bodies in contact, mechanical work is required to overcome the adhesion forces between the two surfaces. Therefore, the work of adhesion [$\Delta\gamma$], which creates a 'new' surface, is given by:

$$\Delta\gamma = \gamma_1 + \gamma_2 - \gamma_{12} \tag{1-11}$$

Where γ_1 and γ_2 are the surface energies of two spheres for creating a unit area of a 'new' surface, and γ_{12} is the interface energy [33].

The JKR theory presented a solution for the contact mechanics between two elastic spheres in contact with an external force. By considering the adhesion force in the contact area between the spheres, The JKR was able to show that at low forces the adhesion forces become important and cannot be neglected, however at high forces, the contact mechanics can be closely fitted to the Hertz model. In addition, the JKR experiments revealed that clean and dry sphere surfaces can significantly increase the adhesion between the two bodies [28, 34].

The parameters used in the JKR model are similar to the ones used in the Hertz theory. The finite contact radius [a], is formed due to the adhesion force between two bodies. The indentation depth shown by [δ] and the relative radii of the sphere curvatures by [R^*]:

$$\frac{1}{R^*} = \frac{1}{R_1} + \frac{1}{R_2} \tag{1-12}$$

Subscripts 1 and 2 denote the two bodies in contact [28]. Fig. 1-6 shows the contact model in the JKR theory compared with the Hertz theory.

Exact analysis showed that the force for separation of the contacted bodies is given by:

$$F_{adh(JKR)} = \frac{3}{2}\pi\Delta\gamma R^* \tag{1-13}$$

The above equation shows that the pull-off/adhesion force is dependent on the equivalent radius of the sphere curvature and work of adhesion. The contact radius [a_1], is calculated by taking into account the surface energy and is derived from:

$$a_1 = \left(\frac{3R^*}{4E^*}\left\{F + 3\pi\Delta\gamma R^* + [6\pi\Delta\gamma R^* F + (3\pi\Delta\gamma R^*)^2]^{\frac{1}{2}}\right\}\right)^{\frac{1}{3}} \tag{1-14}$$

Where, F is the external force and E^* is:

$$\frac{1}{E^*} = \left(1 - \frac{\nu_1^2}{E_1}\right) + \left(1 - \frac{\nu_2^2}{E_2}\right) \tag{1-15}$$

Here, E_1 and E_2 are the elastic modulus, and ν_1 and ν_2 are the Poisson ratio of the two spherical bodies.

From Eq. (1-14) it can be seen that both external force and the adhesion force has an effect on the contact radius between the two bodies. The indentation depth is derived as:

$$\delta = \frac{a_1^2}{R^*} - \frac{2}{3}\left(\frac{18\pi\gamma a_1}{4E^*}\right)^{\frac{1}{2}} \tag{1-16}$$

By substituting the Eq. (1-14) into Eq. (1-16), the indentation depth can be obtained as a function of the external and adhesion forces.

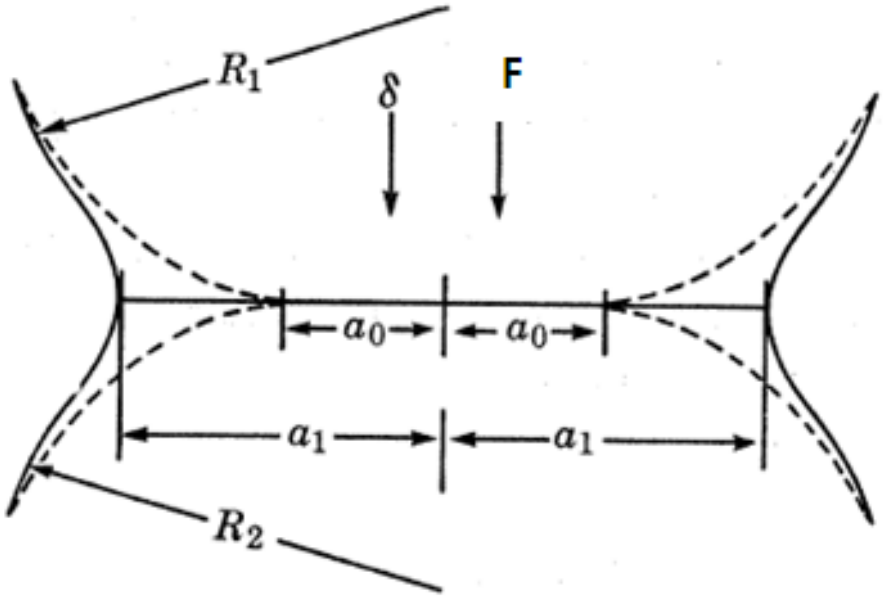

Figure 1-6. Schematic of the JKR model for the contact between two elastic, spherical bodies. Sphere radii [R_1] and [R_2] under the external force [F], the indentation depth [δ], as well as the adhesion force between the two spheres is considered in the JKR model. The dashed lines illustrate the contact area between the spheres, with the contact radius of [a_0] in the Hertz model (neglecting the adhesion forces). The solid lines show the contact area in the JKR theory (presence of the adhesion forces), which has a contact radius of [a_1] [28] .

1.3.3 DMT theory

Further developments of the Hertz model were carried out by Derjaguin and colleagues in 1975. In their study, they presented the DMT theory, which modelled the elastic interaction between an elastic spherical body and a perfectly rigid surface under the action of a normal force without friction. The DMT model considers the effect of the adhesion in the deformation profile just outside the contact region, where the surfaces are a small distance apart. This implies that the Van der Waals interactions outside the elastic contact regime are taken into consideration. The Van der Waals interactions are capable of increasing the elastic contact area between the spherical sample and the rigid surface (Fig. 1-7). To determine the contact force, the contact radius and the indentation depth between the two bodies, the adhesion force calculations (mentioned in the JKR theory) was applied in the DMT theory [29, 34].

The adhesion/pull off force resulting from the Van der Waals interactions outside the contact zone, can be derived by:

$$F_{adh(DMT)} = 2\pi\Delta\gamma R \qquad (1\text{-}17)$$

Where R is the radius of the spherical body, and $\Delta\gamma$ is the work of adhesion. It can be seen from the above equation, that the adhesion force is proportional to the first power of the spherical samples radius and the work of adhesion.

The contact radius of the two spheres, $a_{DMT,}$ is given by:

$$a_{DMT} = \frac{3R}{4E^*}(F + 2\pi\Delta\gamma R)^{\frac{1}{3}} \tag{1-18}$$

Here, R is the radius of the spherical body, F is the external force, $\Delta\gamma$ is the work of adhesion and E^* is:

$$\frac{1}{E^*} = (1 - \frac{\nu_1^2}{E_1}) + (1 - \frac{\nu_2^2}{E_2}) \tag{1-19}$$

Where E_1 and E_2 are the elastic modulus and ν_1 and ν_2 are the Poisson ratios of the two spherical bodies. Eq. (1-18) also shows that the contact radius between the two spheres depends on the work of adhesion, Young's modulus and the Poisson's ratio of the two spheres.

In addition, the deformation of the sphere under the applied force can be calculated from:

$$\delta = \frac{a_{DMT}^2}{R} = \frac{(F + 2\pi R\gamma)^{\frac{2}{3}}}{(\frac{9}{16}RE^{*2})^{\frac{1}{3}}} \tag{1-20}$$

And finally, the total force can be obtained from:

$$F_{total} = \frac{3}{4}E^*\delta^{\frac{3}{2}}R^{\frac{1}{2}} - 2\pi R\gamma \tag{1-21}$$

Eq. (1-21) indicates that the total force is proportional to the 3/2 power of the indentation depth [29].

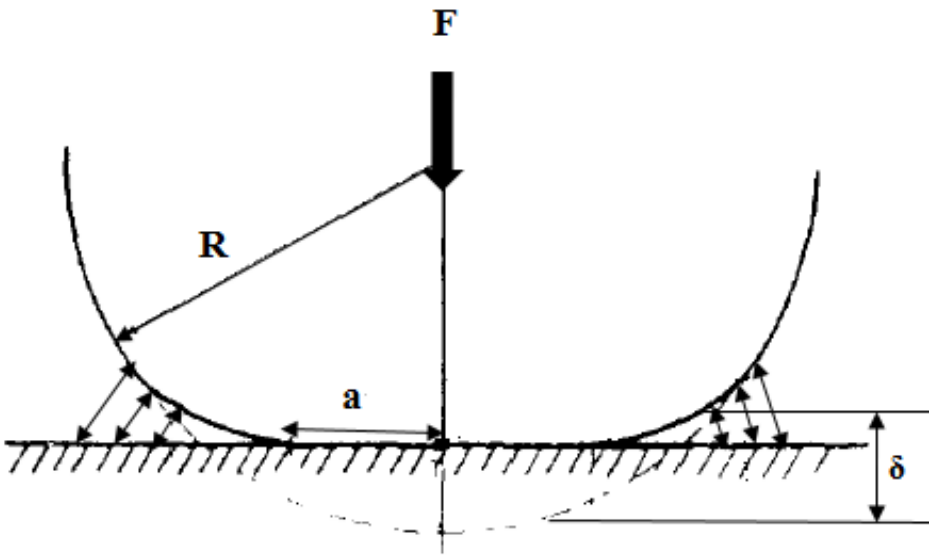

Figure 1-7. Schematic of the DMT model showing the contact between an elastic sphere, with the radius of [R], and a rigid surface. An external force [F], is applied to the body to deform it. The Van der Waals interactions outside the contact area are illustrated by the double sided arrows [29].

1.3.4 The elastic shell theory

A shell is defined as a thin-walled plate, which is curved in its non-deformed state. The definition of "thin-walled", means that the thickness of the shell is small in comparison to its dimensions in the other two directions (length and width). A shell can be considered as elastic if it returns to its original shape after the removal of an external load. A shell can be composed of a single layer of material, or composed of different/multiple layers of materials. Shells are divided into two degenerate classes; (1) plates, which in their non-deformed state are flat and (2) membranes, which they do not resist deformation (as they deform, the stretching stresses are larger than the bending stresses).

The elastic shell theory assumes that under sufficiently small strains, the stresses are proportional. The simplicity and efficiency of this model, makes it widely used in the field of mechanics. Under large deflections the model is no longer valid, due to geometrical non-linearity [35].

Despite the thickness of a shell, it is considered a three-dimensional body. Therefore, the shell theory must be equivalent to the three-dimension of the material from which the shell is made. Due to complications associated with three dimensional equations and boundary conditions, to solve those problems thin shells can be assumed as a two-dimensional body, so simpler solutions required to solve them and the results are expected to reflect the three-dimensional body with an acceptable accuracy.

To do so, there are two different theories. First one is the derived theory in which the general laws of continuum mechanics are applied to the kinematic (motion) and constitutive (stress, strain) equations of three dimensional bodies to stablish them in a way that the number of variables reduces to two parameters on a surface of the body. The second one is the direct theory in which a finite portion of the body under observation, having property of deformability is subjected to a certain amount of force. This force exerted over the surface of the said body is supplemented by the natural fields of geometric object giving it the property of deformability. Despite from the chosen theory the adequacy and amount of available information effect on the accuracy of the derived results. Therefore, there are various theory of shells available based on using different ways and methodologies [36]. Generally, for the linear elastic shell theory the main aim is to find the stresses in terms of the applied known force to the surface of the body. In the classical methods to solve the problem, first the equilibrium of all the forces on a small portion of the body must be formulated. Based on the situation if it is necessary to consider the weight of the body then it should be added to the force equilibrium equation. Normally the derived equation is linear in terms of the applied force and resultant stresses. Second step is to determine the relation between the strains and the overall displacement, which can be formulated based on the geometry of the body. Finally, to find the stress-strain relations the two above steps need to be combined. The provided equations then can be used to solve the unknown parameters such as displacement and elastic modulus [37].

Shell theory has lots of applications in different fields such as biological samples (membranes) and any thin structural films made with the shape memory materials [38]. It can be used to calculate elastic modulus of samples indented by AFM [39]. Using this theory cells can be considered as the shells (cell membrane) filled with cytoplasm/liquid. So, the cell membrane assumes as a thin film and the cytoplasm provides a uniform hydrostatic pressure on the membrane.

1.4 Cell elasticity

Cellular elasticity is one the main physical properties attributed to the mechanical function of a cell. The elastic modulus of a cell determines its inherent ability to recover its original shape following an applied external deformation force. A variety of complex mechanical forces such as stress, strain, pressure and fluid flow can continually affect a cells physiological function. Apart from their physiological function, the mechanical

properties of a cell such as elasticity/stiffness play an important role in enabling the cells to withstand external forces. As mentioned above the more cell is elastic the more it can recover from the external forces. Furthermore, the mechanical properties of cells (such as the elastic modulus), can be used as an indicator for alterations in cell mechanical behaviour in diseased states. Interestingly, cells can also exhibit contradictory mechanical properties. This means that, while a cell can act as a solid to maintain its shape under an applied mechanical force, it also can perform reversible deformations, which is a characteristic of liquids [40, 41].

It is well understood by researchers that there is a direct link between cell function and structure, which contributes to overall cell elasticity [40]. The elastic properties of cells, along with their deformation behaviour, play an important role in the biological and biophysical responses of cells [42]. Physical intracellular changes can occur within a cell due biological events such as cell differentiation, drug treatment and a cells interaction with the surrounding supporting extracellular matrix [43]. It has been shown that the mechanical changes that occur within a cell, plays a key role during cell differentiation, the cell cycle and its morphological changes associated with its shape [44, 45]. Furthermore, distinct mechanical properties can be measured for cell types that present with specific physiological functions [46]. For example, cell mechanical measurement studies have demonstrated the variations in the elastic modulus between healthy and cancerous cell types [21, 47]. A wide range of mechanical models (each model being dependent on different cell parameters such as cell shape, type and experimental conditions) have been utilised for understanding the mechanical properties of cells, and this has resulted in broad range of estimated values for different cell type specific elastic properties [5].

The elastic properties of cells can be characterized using quantitative parameters like the elastic modulus, which is defined as the relationship between applied stresses and the resultant strains. Stress is equal to the quantity of deformation force, and strain is defined as the amount of deformation. There are different forms of elastic moduli to calculate the mechanical properties of cells. These include the Young's modulus [E], bulk modulus [K] and shear modulus [G]. For isotropic materials, the elastic properties of the material can be explained using two elastic parameters, which are known as the Lame parameters. The elasticity of a cell can be described by Hooke's law in terms of the ratio between stress and strain, which are equal to the constant parameter of elasticity, depending on the material properties and deformation. The elastic modulus of a biological sample is

material specific, and can vary depending the type and depth of deformation (more details in Chapter 3) [41].

In this project, the Young's elastic modulus [E] (force per surface area) was used as the primary parameter for all cell mechanical measurements. All stress-strain relations were kept linear for small deformations, such that the cells could return to their original shape, following the removal of the applied external force. In addition, among from different techniques available to measure the mechanics of single cells, AFM was used to do all the measurements on the cells. The main reason is based on the ability of the AFM technique to provide information from different/selected locations on a cell. Therefore, analysing the effect of different organelles (e.g. nucleus) on the mechanical properties of the cell can be carried out more accurate.

1.5 Young's modulus and its AFM measurements in living cells

Young's elastic modulus is one of the parameters, which can be used to quantify the elastic properties of living cells. Derived Young's elastic modulus using the AFM technique depends on different parameters such as, shape of the applied indenter, stiffness of the cantilever, rate of indentation and the applied mechanical contact model [5, 8]. For instance in one study the elastic modulus of the HL60 cells were measured using pyramidal and spherical indenter. Keeping the rest of the parameters constant, using the Hertz model the elastic modulus derived from the pyramidal indenter was 0.8 kPa while the elastic modulus calculated from the spherical indenter was 0.3 kPa. It was discussed that the observed differences in derived elastic modulus from the two indenters are due to the fact that applying the spherical indenter provides more overall elastic properties of the cells while the conical indenter measures local elastic properties of the indented cell [48]. Some of the previous studies on measuring elastic properties of different types of mammalian cells are summarized in Table 1-1. It can be seen that while AFM can be applied for almost all types of cells for elasticity measurements, derived Young's elastic modulus can be easily affected by different parameters. Also, another factor which influences on the measured elastic modulus, arise from the heterogeneity of the cell. This means that indenting a cell over its body can give an elastic modulus different from elastic modulus derived from indenting the edge or nucleus area of the cell. For example, a study on elastic properties of the human umbilical vein endothelial cells showed that the elastic modulus value was 7.22 kPa over the nucleus; 2.97 kPa over the cell body in proximity

to the nucleus and 1.27 kPa on cell body near the edge [49]. Therefore, the elastic modulus of the cells in Table 1-1 presented in a range rather than one specific value.

Table 1-1. Young's elastic modulus of different mammalian cells derived from AFM measurements.

Cell type	Tip shape	Spring constant (N/m)	Indentation rate (μm/s)	Contact model	E (kPa)	Reference
Endothelial cells	Pyramidal	0.02	5	Hertz	0.9-1.7	[50]
Leukemia myeloid cells (HL60)	Pyramidal	0.009-0.01	0.4	Hertz	0.2-0.8	[48]
Osteoblast	Pyramidal	0.03	6	Hertz	1-2	[51]
Neutrophils	Pyramidal	0.009-0.01	0.4	Hertz	0.07-0.15	[48]
Fibroblasts	Pyramidal	0.01	2-12	Hertz	4-5	[52]
Murine muscle cells	Cone	0.03-0.05	9	Hertz	11-45	[53]
Cardiocytes	Cone	0.03-0.05	5	Hertz	90-110	[54]
Erythrocyte	Cone	0.03	5	Hertz	14-18	[55]
Astrocytes	Flat	0.01-0.03	3-5	Hertz	2-3	[56]
Epidermal keratocytes	Cone	0.06	0.2	Hertz	10-55	[57]
Platelets	Cone	0.02-0.03	9	Hertz	1-10	[58]
Macrophage	Cone	0.08	5	Hertz	1.2-2.5	[59]
Cortical hair cells	Flat	0.05	6-8	Euler beam theory	300-400	[60]

1.6 Motivations

The most recent advances in the life sciences and therapeutic science community have carried out with the cooperation between biological scientists, life scientists, chemists and process engineers. Applying mathematical models to measure and quantify the mechanical properties of biological samples has increasingly become an important tool in different research areas such as diagnostics and therapeutics [61], as well designing

and improving the current cell purification and separation methods [62, 63]. Of the available mathematical models, which are currently widely uses to measure mechanical properties of biological samples (e.g. Hertz model), none of them were originally designed and developed for the measurement biological materials. Thus, some of the assumptions made in the current models cannot be applied in measuring the mechanical properties of biological samples. Therefore, one of the main motivations for this research thesis was to develop a model that considers the physical characteristics of biological cells in the contact mechanical model calculations.

An additional aim of this research thesis arose based on the great interest in the production of manufactured red blood cells (RBCs). It has been reported that the annual worldwide requirement of RBCs is as high as 90 million units [64], which cannot be covered by the current supply of donated blood. Therefore, to fulfil this shortage, the *in vitro* production of RBCs is highly thought-after. Manufactured RBCs require post processing protocols such as sorting and separation to ensure that all cells are highly purified and culture media is free from the unwanted cells and debris. The most recent advances in cell sorting, which can be used for improving cell separation processes with high efficiency and less drawbacks, are methods that utilise the mechanical and physical properties of cells to separate and sort mixed cell populations [65]. Therefore, investigating the elastic properties, size and shape of biological cells during the *in vitro* production process, could allow for the fabrication/design of a more effective and high yield cell purification and separation method.

1.7 Thesis scope and structure

This thesis has two main goals. The first goal is to develop and validate a new mechanical model based on the elastic shell theory to measure the elastic modulus of cells indented with conical tips, using AFM. The second goal is to study the mechanical and physical changes of the umbilical cord blood CD34+ stem cells during their maturation and differentiation process, in order to help advise the design of highly efficient cell purification and separation techniques. Fulfilling the first goal will help for a better understanding of the physical and mechanical properties of biological samples. The main impact of this work could be obtaining the Young's elastic modulus of biological samples by considering additional physical features of the indented cells (size of the biological samples and thickness of the cell membrane) in the contact model calculations. Moreover, the results from this thesis could provide more information about changes in the size of

the biological samples due to the external applied forces. Positive outcomes for the second goal could pave the way towards selecting high yield and minimum drawback cell sorting and separation techniques. The ultimate impact of this work could be in optimization of current cell sorting separation methods, by reducing the costs, unnecessary procedures and separation time.

Therefore, the objectives of the thesis are:

- To develop a mechanical model for measuring the Young's elastic modulus of biological samples by considering the thickness of the cell membrane and changes in the radius of the cells before and after of the indentation;
- Validate the developed model by testing the model using the data collected from indenting J774 macrophage cell line with AFM;
- Measure the mechanical and physical properties of RBCs during their differentiation process to select proper sorting and separating techniques;
- Study the elastic modulus of the cell nucleus and its effect on the elastic properties of cell.

The outcomes of this thesis are structured in the following way to meet the described objectives:

Chapter 2: Material and methodology

The general materials and methods, which were used in every experiment are explained in this chapter. The materials which were utilised for the preparation and maintenance of the cell lines are defined in detail in this chapter. Furthermore, the operating modes of AFM, which were used to measure the mechanical properties of the cells are also discussed. Finally, the applied data processing methods to analyse the obtained data is also described.

Chapter 3: Mechanical modelling of biological cells

In this chapter, the methodology undertaken to determine the Young's elastic modulus and size changes in cell was investigated. The method presented is based on the elastic shell theory, and it was developed by changing the geometry of the AFM indenter. Firstly, a simplified form of deformation with a plate is described to demonstrate and explain the necessary steps to develop the proposed new model. Following this, the indenter is changed to a conical geometry, and the calculations are modified for the new geometry.

The analysis carried out in this chapter was done to test the newly developed model, and to predict the size changes and Young's elastic modulus of the indented biological cells. Furthermore, the relationship between the obtained new radius, applied force and indentation depth were also investigated.

Chapter 4: Investigation of the mechanical properties of umbilical cord blood CD34+ stem cells during their differentiation and maturation process for sorting and separating purposes

This chapter was designed to study changes in the elasticity, size and shape of umbilical cord blood CD34+ stem cells during their expansion, differentiation and maturation process, to better improve current cell sorting and separating processes. Due to the high demand for donor red blood cells (RBCs), different protocols aimed at improving their *in vitro* production has increased rapidly. High yield with less downsides in cell purification and separation techniques are required to sort cells and separate them from the unwanted cells and the extruded pyrenocytes in the cell culture media. In this chapter, the current available sorting and separating techniques are discussed, with great emphasis on the methods to purify and separate biological cells based on their mechanical and physical properties (elastic modulus and size). Therefore, the Young's elastic modulus, size and shape changes of cord CD34+ stem cells at four different stages of their expansion and differentiation processes was investigated. AFM was utilised for all cell elasticity measurements, and obtained data fitted with the Hertz-Sneddon model to derive the Young's elastic modulus. All the cells were measured prior to measurements for size and shape investigations.

Chapter 5: Study on the mechanical and physical properties of pyrenocytes for understanding the effect of nucleus and enucleation process on mechanical properties of cord CD34+ stem cells

The analysis carried out for the experiments described in the previous chapters on the elastic modulus of the cells during different days of cell expansion and differentiation, showed that cells become softer as they differentiate. Therefore, we predicted that these changes are due to the effect of cell's nucleus and the enucleation process. In this chapter, the effect of the cell nucleus on the derived elastic modulus of the cells was investigated. To carry out this analysis, first, we studied the mechanical and physical properties of the extruded nucleus of the cells (pyrenocytes). The results from measuring the elasticity,

size and shapes of pyrenocytes were then compared with the results derived from the whole cell measurements in the previous chapters. Furthermore, it is also discussed how the derived results from pyrenocytes measurements can be applied for selecting/ designing better cell sorting and separation methods. The effect of a cell's nucleus on the elastic modulus of the cells was also studied. For this purpose, using the data obtained from the previous chapter, cells at early stages of differentiation, which are nucleated were analysed. The elastic modulus of a cells nuclear region was compared with the elastic modulus for the rest of the cell. The nuclear region in each cell was identified by analysing the height changes across the surface of the cell. Finally, further investigations on the effect of the nucleus on the elasticity of the cells was done by preparing samples of the cells during their enucleation process, and sorting them with the Fluorescent-Activated Cell Sorting (FACS) machine into nucleated and enucleated groups. Then, elastic modulus, size and shape of each group was then measured and compared with each other.

Chapter 6: Looking back and working forward

A summary of the works carried out in this thesis and the main outcomes is provided in this chapter. Future works are proposed to pursue the benefits of further investigations on different aspects of the results presented, which could alter the mechanical and physical properties of cells. In particular, further research into the biological events that occur alongside mechanical changes during cell differentiation is suggested. It is suggested that the biological changes can have an important effect on the elastic properties of cells. Therefore, further research into this area could provide valuable information, which could be useful in clinical research as well as the improvement of the current cell sorting and separation techniques.

CHAPTER 2

Material and methodology

Contents

2.1 Introduction

In this chapter, the general experimental materials and methods which have been applied to all experiments are explained. Atomic Force Microscopy (AFM) was used as the primary method for measuring the elastic properties of the described cell types, as well as for cell surface topography imaging. All cell mechanical data obtained (cell elastic moduli) was processed using the JPK SPM data processing software. When further analysis of the obtained force-displacement curves from the AFM was required (e.g. testing the developed model), Gnuplot data processing software was used.

2.2 Cell preparation

For the selected chosen cell types, alternate culture and preparation methods were used and will be denoted specific cell type. Two different cell lines have been used in this project; a murine J774 macrophages cell line, and human umbilical cord blood CD34+ derived red blood cells (RBCs).

2.2.1 Murine J774 macrophages cell preparation

Murine J774 macrophages were cultured and maintained with RPMI 1640 medium (Fisher scientific, UK) supplemented with 10% heat-inactivated fetal bovine serum (FBS) (Fisher scientific, UK) at 37°C in 5% CO_2 in air [66].

To prepare the cells for AFM experimentation, a concentration of 2×10^4 cells/ml was seeded onto the AFM sample culture dish (TPP, Switzerland) and kept overnight at 37°C in 5% CO_2. The chosen cell seeding density produced well developed, fully attached single cells suitable for AFM measurements. Prior to all AFM measurements, cell sample dishes were mounted onto a heated BioCell™ stage (JPK instruments), which maintains the cells and RPMI 1640 medium at 37°C during the course of the AFM measurements.

2.2.2 Umbilical cord blood CD34+ stem cells preparation

Umbilical cord blood CD34+ cells from a single donor have been used to produce reticulocytes. The preparation of the cells was done by colleagues, whom currently investigating *in vitro* RBC production. The process of CD34+ cell expansion, differentiation and maturation can divide into four steps. The first step takes three days and during this time mesoderm formation happens from the cord blood cells. The second step is the formation of embryoid bodies and this step takes around ten days. In the third step the haematopoietic progenitors are further expanded and then differentiated into erythroid cells. This step happens between days 11 to 21. During this step, especially from day 14 of differentiation on ward, the enucleation process starts and nuclei expel from cells (known as pyrenocytes). The last step is maturation of the erythroid cells and can take up to ten days (more details in Chapter 4, section 4.2.1) [67]. In this work, specifically, the elastic modulus of the cord CD34+ cells were tested on days 11, 14, 18 and 21 of the differentiation protocol (Chapter 4, section 4.3). Produced cells were measured using AFM in an attempt to determine how the mechanical properties of the cells changes during various selected points the differentiation protocol.

Since the cord CD34+ cells are not naturally adherent, AFM sample petri dishes were coated with poly-D-lysine hydrobromide (Sigma, UK). Poly-D-lysine is a positively charged amino acid polymer with an attachment factor, making it suitable for the adherence of cells to a solid substrate. Specifically, Poly-D-lysine enhances the electrostatic interactions between negatively charged ions on the membrane surface of the cells and the substrate/petri dish surface. When coated to the AFM sample petri dish, poly-D-lysine increases the number of positively charged sites for cell binding [5]. Poly-D-lysine is available in two different ranges of molecular weights: 30,000-70,000 Da and 70,000-150,000 Da. Although, the lower molecular weight poly-D-lysine is less viscous in solution and easier to apply, the higher molecular weight of the polymer provides more attachment sites per molecule [68]. Therefore, when coating the dishes with poly-D-lysine, a molecular weight of 70,000-150,000 Da has been used.

To prepare the poly-D-lysine and coat the AFM sample petri dishes, 50 ml of sterile tissue culture grade water was added to 5 mg of poly-D-lysine and mixed well. Based on the supplier's recommendation, 1 ml of the prepared solution is enough to coat 25 cm^2 of surface area. Petri dishes used for all experiments had a surface area of 9.62 cm^2. Thus, 0.38 ml of prepared solution was applied aseptically to coat the surface of each petri dish. The petri dishes were then rocked gently to spread the solution evenly across the surface of the prepared dishes. Coated dishes were then left to dry for ~ 2 hours, following which any excess solution was removed by aspiration. Prepared dishes were then sterilized under the UV light for 20 minutes prior to the cord CD34+ cells seeding. Using poly-D-lysine to cover the petri dishes can arise the concern about side effects of the polymer on the physiological behaviour of the cells. Studies on the effect of the poly-D-lysine on physical and mechanical properties of cells showed that concentration of the polymer has direct effect on physiological properties of cells. Cells on the dish coated with high concentrations (>10 mg/ml) did not attach to the surface and showed a circular morphology due to the high toxicity of polymer and fusion of the cell membrane. However, in the dishes coated with low concentration of the poly-D-lysine (<1 mg/ml) cells adhered and spread on the surfaces with no significant changes in their morphology [69]. Therefore, in this work a concentration of 0.1 mg/ml of poly-D-lysine was used in experiments to cover all the petri dishes.

To prepare the cells for AFM experimentation, a concentration of 2×10^6 cells/ml was seeded onto the coated AFM petri dishes. The dishes were then incubated for ~1 minute to allow for adequate cellular attachment. Cell seeded sample dishes were then gently

rinsed with 1 ml of Hank's Balanced Salt Solution (HBSS) (Merk Millipore, UK) to remove any loosely and/or unattached cells. 2mls of HBSS was then added to the sample dish, which was then mounted onto the BioCell™ stage, which maintains the cell sample and HBSS media at 37°C for the duration of the AFM experiment. Since the AFM is an 'open' system, maintaining the cells at the recommended 5% CO_2 during the experiment is not practical. CO_2 is not used by cells but keeps the pH of media at 7. Without CO_2, the acidity of the cell culture media will increase rapidly, reducing the optimal conditions for cell survival and viability. Given that the cord CD34+ cells are highly sensitive to external environmental alternations, HBSS was chosen as the liquid medium to measure the cells for AFM experimentation as it is essential to keep the pH of the media balanced, and will not adversely affect the viability of the cells during the experiment window [70].

2.2.3 Fixation of umbilical cord blood CD34+ stem cells for AFM imaging

For AFM cell imaging, the cord CD34+ cells were fixed using a paraformaldehyde solution (Thermo Scientific, USA). Cells were fixed in a 4% solution of paraformaldehyde, prepared by diluting 1 ml paraformaldehyde in 3 ml of Phosphate Buffer Saline (PBS) (Fisher scientific, UK). Prior to cell fixation, the cord CD34+ cells were first seeded onto the coated AFM petri dishes, and left for one minutes to allow for adequate cell attachment. Excess HBSS media was then removed and the dish washed once with PBS. The prepared 4% solution of paraformaldehyde was then added to the sample dish and left for 10 minutes at room temperature to fix the cells. The fixative solution was then removed, and the fixed cell sample washed with PBS three times. The fixed cell sample dishes were then mounted onto the AFM for imaging.

2.2.4 Preparation of the pyrenocytes extruded from the cord blood CD34+ cells

AFM measurements were performed on pyrenocytes (extruded nucleus) (Chapter 5, section 5.1) extruded from the cord CD34+ cells during the differentiation process. To perform the experiments on the pyrenocytes, samples from day 14, 18 and 21 were used. Preparation of the samples were exactly same as the preparation of the cord CD34+ cells, which explained in section 2.2.2. Also, pyrenocytes were imaged without fixation, since they could tolerate the applied force for longer time without bursting.

2.3 AFM set up and measurements

All the experiments detailed were carried out using a NanoWizard III Bio AFM (JPK Systems, Berlin, Germany), mounted on a Zeiss Observer D1 inverted optical microscope placed on top of a Halcyonics i4 anti-vibration table. To reduce the effect of ambient noise, the AFM is setup in an acoustically isolated box (Fig. 2-1).

Two separate force spectroscopy modes were used to acquire cell mechanical data for the two chosen cell types. Force mapping mode was used for the J774 macrophage cell line, and quantitative imaging mode (QI) for the cord CD34+ cell line.

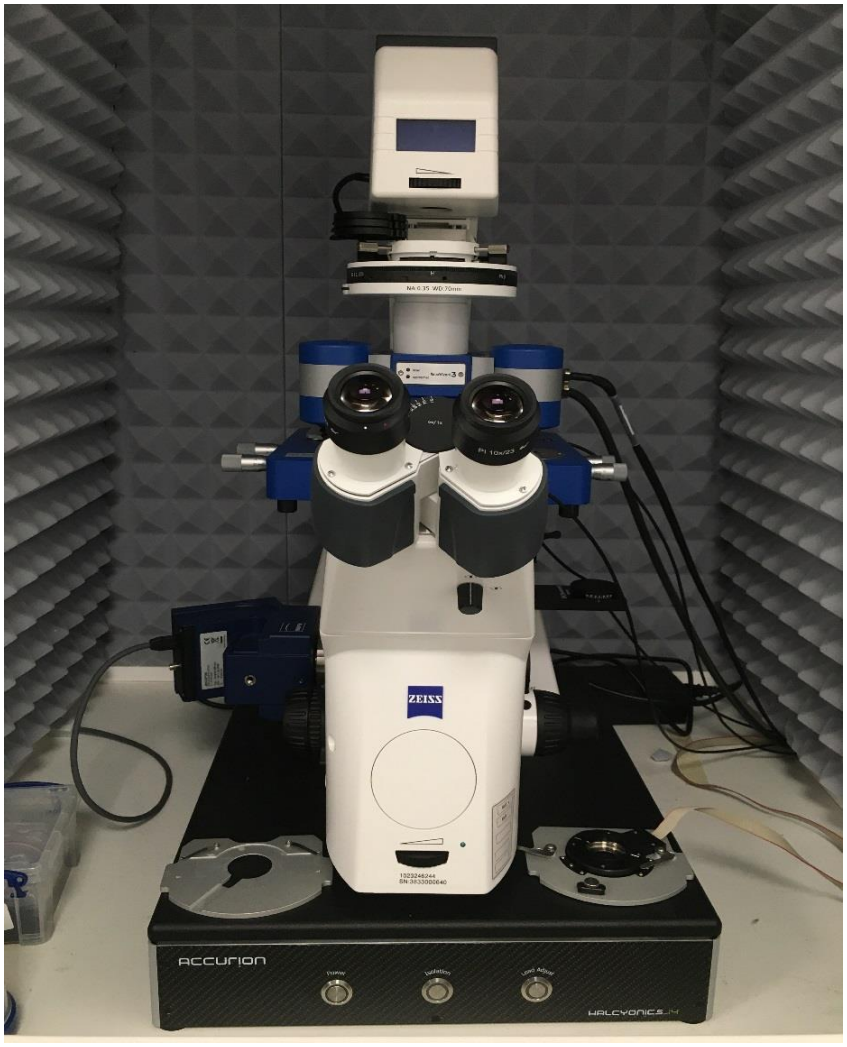

Figure 2-1. AFM NanoWizard III Bio placed on the top of the vibration isolation table. The whole system placed in the acoustically isolated box.

2.3.1 AFM force mapping mode

Force mapping mode is an extension of the standard spectroscopy mode. Force mapping mode performs multiple force-displacement measurements across a specifically selected region on a selected cell. Each map is constructed from an array of pixels, referred to as a force map "index". Each force map index provides a single force-displacement curve, from which the Young's modulus for that specific indentation can be derived. Force mapping index sizes can be defined, with a minimum index size of 8×8 force map pixels, and a maximum of 128×128 pixel indexes. Once the sample petri dish with cells is mounted under the AFM, the probe can be positioned over a chosen region for force mapping. All the force map curves detailed for the J774 macrophage cell line were gathered out using an 8×8 force map index, producing 64 force-displacement curves for each cell. Force indentation parameters were kept constant for each experiment, with indentation speed and maximal indentation force exerted set at 5µm/sec and 2nN respectively.

2.3.2 AFM quantitative imaging mode

Quantitative imaging (QI) mode is an integrated imaging version of force spectroscopy, where each pixel within an acquired QI image gathers both topographical as well as the force-displacement properties of a QI imaged cell. Specifically, QI mode produces a force-indentation curve for each index/pixel of a selected imaged cell region. The main difference between QI mode and force mapping mode, is a variation in the algorithm for cantilever tip movement and probe sampling rate. Cantilever tip movement and raster scanning in force mapping mode, is from left to right for first row and then from right to left for the second row. However, for the QI mode the tip movement for all rows is from left to right (Fig. 2-2). For both modes, the selected sample rate is the number of collected indexes per second. Sampling rates are controlled in such a way to enable maximal detection of all surface features of the cell region along with each gathered within the force curve. Increasing and/or decreasing the sample rate, can produce more or less amounts of data points for data processing. QI mode was carried out for all the cord CD34+ cell AFM experiments, with indentation speed kept the same as was set for the force mapping of J774 macrophages (5µm/sec), with a slight variation in the applied force (0.8 - 1 nN).

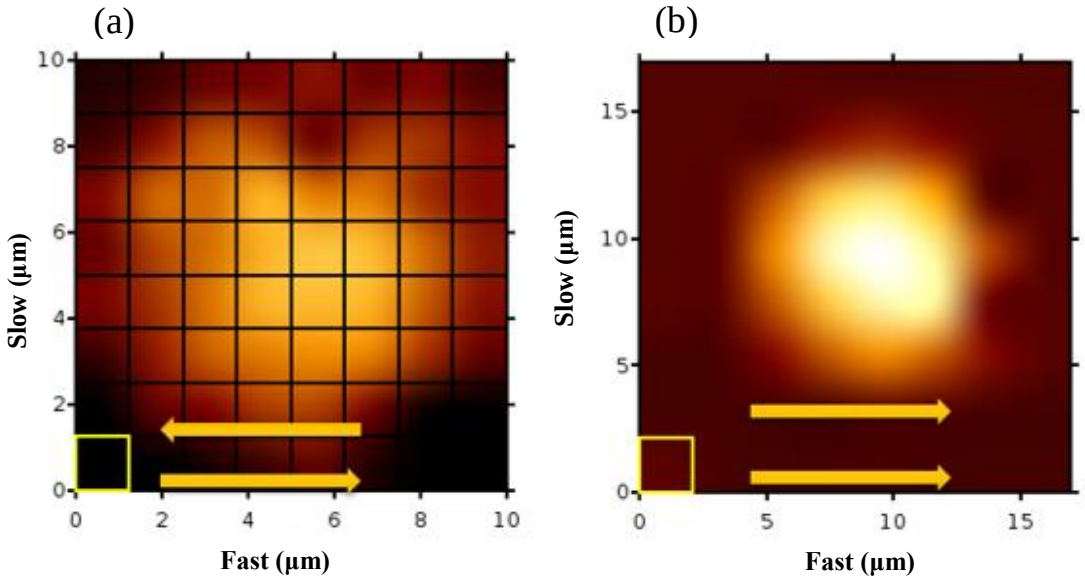

Figure 2-2. Difference between direction of the tip movement in (a) the force mapping mode and (b) the QI mode.

2.3.3 AFM sample temperature control

When working with live cells, it is essential to maintain them within a controlled *in vitro*-like environment. Temperature control is one of the most important factors in maintaining cell viability during AFM experimentation. Thus, all force spectroscopy experiments were carried out using the JPK BioCell™ temperature controller stage (Fig. 2-3), to maintain the temperature of the cell sample media at 37°C.

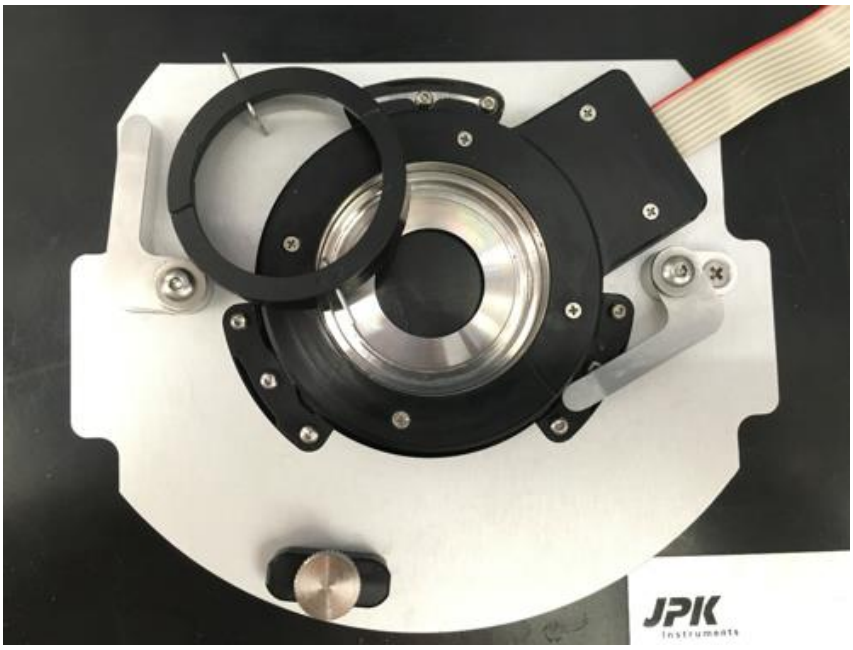

Figure 2-3. JPK BioCell™ stage to control the temperature of the culture media of the live cells.

2.4 AFM probe selection

Selecting an appropriate probe for any force spectroscopy experiment is essential. Factors such as cantilever material as well as tip geometry, coating and spring constant are all properties one should take in to consideration when attempting to measure the elastic properties of living cells. Cantilevers with a soft enough spring constant to be considered suitable for force spectroscopy on biological samples are often fabricated from silicon nitride (Si_3N_4) as it is extremely flexible and unlikely to break during even the deepest of indentations; however pure silicon (Si) cantilevers are also capable of extremely soft indentations. It is important to select a probe with a spring constant similar to that which you expect the sample to have for the most reliable results. If indenting live cells this would typically be around 0.02 N/m. Stiff cantilevers (> 0.1 N/m) do not have the sensitivity suitable for indentations on live cells [13].

For all AFM experiments, silicon coated HQ: NSC36/Cr-Al series conical probe cantilevers, (MicroMasch, UK) with a half cone angle of 20º and a tip radius of ~8nm were used for indentation on both chosen cell types and pyrenocytes (Fig. 2-4). The conical probes were chosen due to the nature of the model we were testing and also to obtain the elastic properties from different locations on the cells.

Moreover, selecting a cantilever with a reflective metal coating can help to increase the reflection of the laser beam from the cantilever towards the receiving photodiode. Furthermore, selecting a cantilever with a spring constants of similar value to the mechanical properties of the soft biological sample is essential to obtain more reliable data outputs. For indenting live mammalian cells, the stiffness of the cantilever should be less than 0.1 N/m. Cantilevers with a stiffness of more than 0.1 N/m are not suitable for indenting live cells, as they do not have enough sensitivity. The spring constant of the probes (HQ: NSC36/Cr-Al) used in all experiments was in the range of 0.06-0.2 N/m, as determined by the thermal fluctuations method. In this method, thermal vibrations cause free fluctuations at the end of the cantilever. Using the thermal fluctuations method results in a balance between the free fluctuations and deflection of the cantilever, providing an accurate spring constant of the cantilever [52].

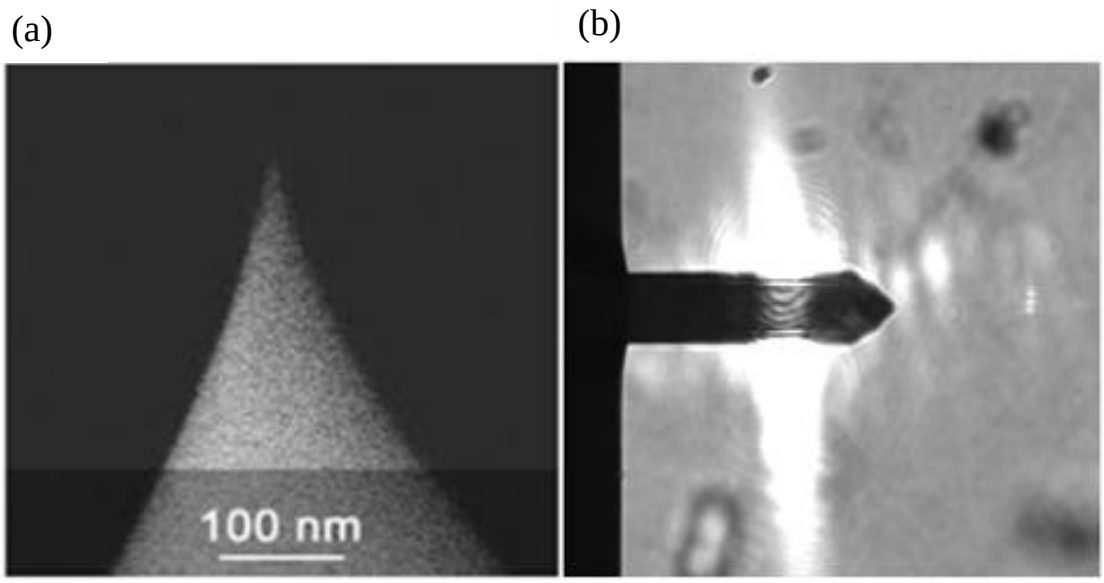

Figure 2-4. HQ: NSC36/Cr-Al probe (a) conical tip with radius (Ri) of ~8nm and half cone angle of 20° (MicroMasch, UK) (b) mounted with the laser aligned on and ready for indentation.

2.5 Sensitivity and spring constant calibration

Before performing any experiment on the AFM, mounted cantilever probes were always pre-calibrated on a clean empty AFM sample dish. Calibration can be done in both air and liquid based on the sample's condition. Given that both selected cell lines were indented in liquid environment, calibration also performed in serum free liquid cell culture media (calibration was performed with RPMI-1640 or HBSS, depending on the cell line being investigated). Prior to calibration of the cantilever, the default AFM unit for vertical deflection of the laser beam on the photodiode is measured in units of Volts. When attempting to image, indent or measure the mechanical properties of cells, the sensitivity and spring constant of the cantilever probe is calibrated in order to convert the vertical deflection unit from Volts to nano-Newton (nN). During calibration, cantilever sensitivity calibration is performed first, which is a necessary step prior to cantilever spring constant calibration (Fig. 2-5). To measure the cantilever spring constant, the thermal noise determination method is used. In this method, thermal vibrations cause free fluctuations at the end of the cantilever. Using the thermal fluctuations method results in a balance between the free fluctuations and deflection of the cantilever, providing an accurate spring constant of the cantilever (Fig. 2-6).

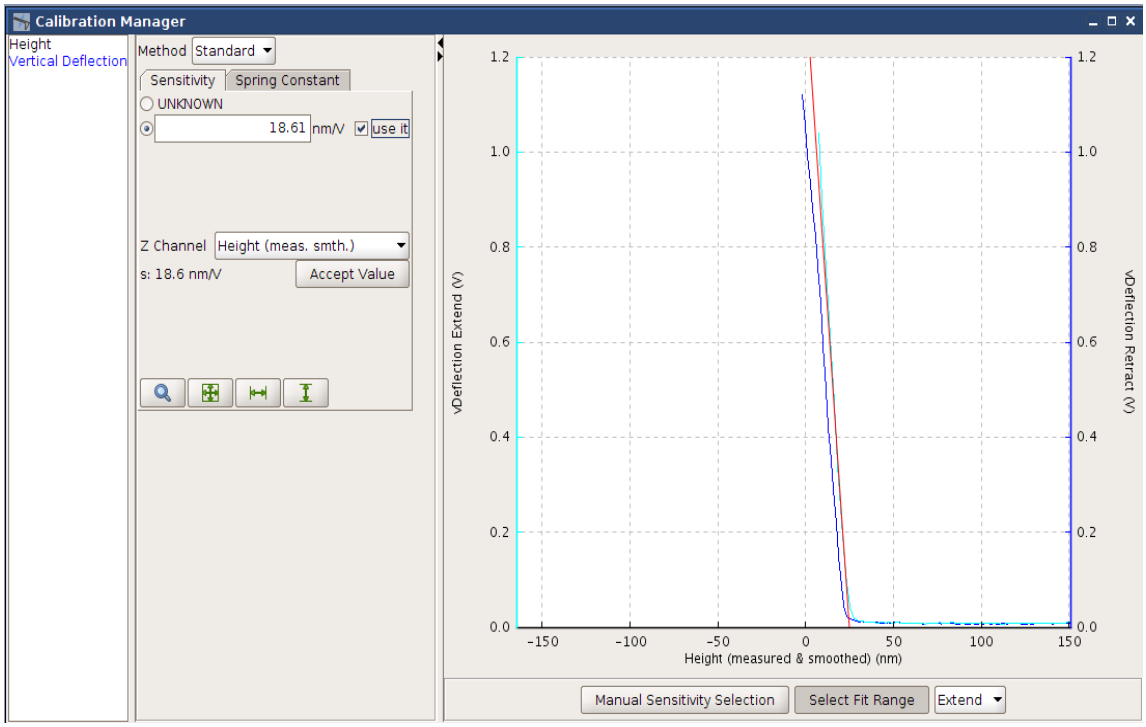

Figure 2-5. Measuring the sensitivity of the cantilever is the first step in converting the unit of vertical deflection from Volts to nN. The light blue shows the approach curve and the dark blue denotes the retract curve. Fitting (red line) should be performed on the approach curve for sensitivity measurements.

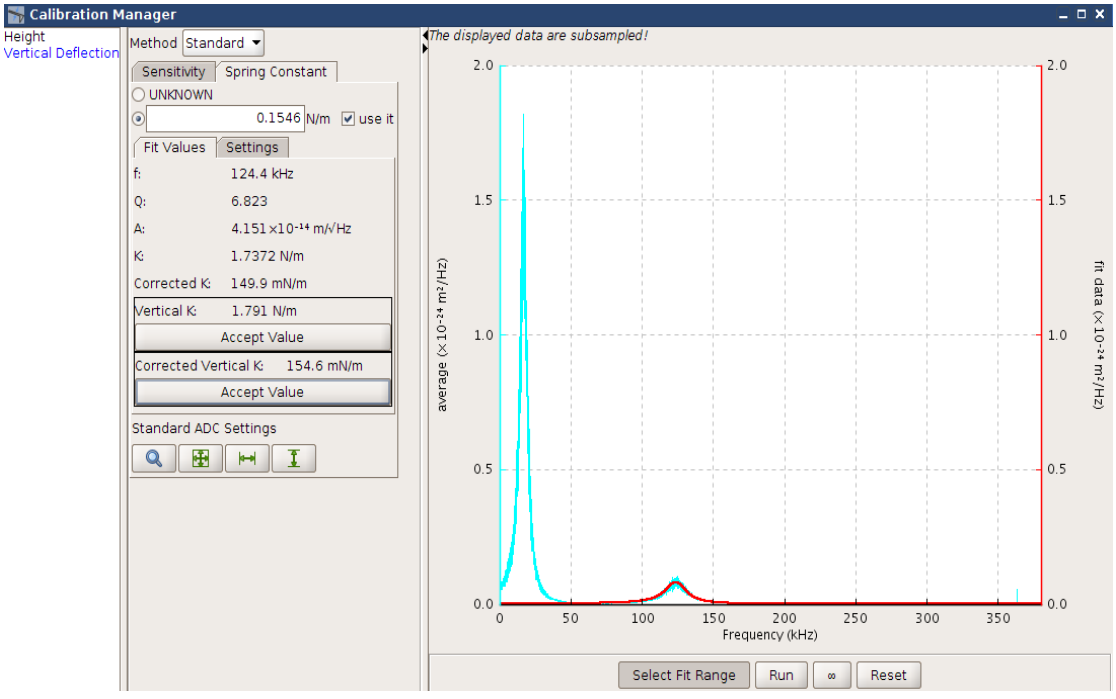

Figure 2-6. Using thermal noise detection method to measure cantilever spring constant, results in one or two frequency spectrums peaks. To find the spring constant of the cantilever, it is necessary to fit the larger peak with the Lorentz curve. If the large curve does not have baseline from both sides (such as the case illustrated), the second curve (with a baselines) is fitted. Upon completion of this step, the spring constant of the cantilever will be determined, and the vertical deflection unit is converted from V to nN.

2.6 Optical direct overlay

For both types of force spectroscopy measurements (force mapping and QI imaging), it is important to position the AFM probe accurately over the cell of interest. Using manual stage manipulation and cantilever positioning (using the coarse movement knobs) is highly subjective and does not allow for the accurate selection and mapping of a specified cell/cell region in force mapping and/or QI mode. Therefore, in order to accurately position the cantilever probe and force map or image a selected cell, direct optical overlay calibration is carried out.

Direct optical overlay calibration is begun by first creating high contrast between the cantilever and the surrounding sample dish substrate. High contrast allows the AFM camera software to recognise the position of the cantilever, and thus calibrate the optical image and centre position of the cantilever probe. Focusing on the cantilever prior to optical calibration increases the chance of more accurate overlay. The generated data from optical overlay is completely independent from the spectroscopy experiment.

Upon completion of the overlay calibration, an optical image of the target cell is then sourced and captured with the CCD camera, and imported into the scan region of the mode selected (force mapping/QI). The desired cell (or cell region) can then be selected by placing a scanning size map over the selected sample. Direct overlay of an optical image has the advantage of taking into account aberrations in the optical image caused by the effect of the mirror and lens of the AFM. The advantages of using this method are; it saves time in locating a selected cell, optical overlay calibration is fast and effective (~1 minute), selection of specific cells can be done more accurately, which is useful to study specific intracellular regions of cells such as the cell nucleus. Optical overlay, when carried out, also insures that entire cells are measured and there is no overlap or regions lost when force mapping or imaging the cells.

2.7 Imaging of cells

For AFM cell imaging, QI (contact mode) was used, with all cell images gathered at a 32×32 pixel resolution. Imaging cells at this pixel resolution took around 20 minutes to gather a complete cell image. J774 cells were imaged live in pre-warmed serum free RPMI-1640 culture media (as they were able to resist the loading rates required for cell imaging without cell rupture). However, for cord CD34+ cell imagining, the cells were fixed prior to AFM imaging as they were less able to tolerate the loading force and

imaging conditions required (rupture for live cells commonly occurred after 8 to 10 minutes of imaging). Due to the nature and size of the J774 cells (they are normally cells with high height), AFM cell imaging was carried out CellHesion mode (section 2.7.1) for J774 cells, with cord CD34+ cells imaged in the standard z-range contact mode.

2.7.1 CellHesion Module

The NanoWizard III Bio AFM currently allows for AFM experimentation in two alternative z-movement ranges. The default range (most commonly used), is applied for most samples with height variances/diameters of less than 15μm, with a piezo z movement range of 15 μm. For samples with greater height profiles, the z-movement range can be increased up to 100 μm using CellHesion module.

In the default mode, the limits of the x-y-z movement of the piezo are confined to the 15μm z-range limit that the piezo alone can move. However, when activating CellHesion mode, the movement of the x- and y- axes is controlled by the AFM piezo head, while the z-range movement is controlled by the CellHesion stage (the microscope stage on which the cell sample is mounted). This enables greater range of movements in the z-direction (an increase of up to 100 μm in z-direction).

2.8 Data processing software

Each force curve obtained following force map or QI mode indentation is processed separately using the JPK data processing tool version spm-5.0.69. All the Young's elastic modulus calculated using the Hertz-Sneddon contact model obtained from JPK SPM data processing software. The Young's elastic modulus, which derived from the developed model (Chapter 3, section 3.7) are obtained via application of the Gnuplot software (see section 2.9 for more details).

Specific functions are applied to each force-displacement curve to allow for the appropriate application of the Hertz-Sneddon contact model, to derive the elastic properties of the selected cells. Three types of functions are applied to each curve prior to fitting with the Hertz-Sneddon contact model (to calculate the Young's elastic modulus). Firstly, the function to subtract the force curve baseline is applied to automatically calculate the average value of the baseline and subtract it from the whole curve. For optimal force curve analysis, the approach portion of the curve is selected (where vertical deflection and height should equal to zero). This part of the curve shows

the region where there was no force detected between the tip and surface of the sample (known as the approach baseline). Under certain circumstances, where there is residue or debris within the testing media, it is often the case that the baseline will not be linear and equal to zero. In such cases, the most linear part of the baseline is selected for analysis.

The second function to be applied to the force curve the determination of the contact point between the sample and cantilever probe. The calculated contact point is then set as the zero force point of the x axis vertical deflection curve. Usually, the absolute position of the z-piezo during the force measurements is not interesting, but rather the relative position of it to the sample surface is mattered and so using this function helps to update the contact point. After applying baseline subtraction and contact point determination functions, both the x and y axes of the force curve are set to zero.

The third and last function to be applied is the calculation of the tip-sample separation. This function corrects the height signal from the cantilever bending and calculates the tip-sample separation. The height signals from the displacement of the piezo come from the cantilever movement toward the sample, followed by bending/deflection of the cantilever into the opposite direction following contact with the sample. To measure the elastic modulus of the chosen cells, it is necessary to first plot the force vs the tip-sample separation (instead of the piezo movement), followed by application of the Hertz-Sneddon contact model. The resulting force curve has a greater gradient, as the corrected distance is always shorter due to elimination of the cantilever bending in to the opposite direction (which results in an additional movement of the piezo toward the cell).

Following application of the previously described functions, the Hertz-Sneddon contact model can then be applied to the processed force curve. Currently, the JPK SPM data processing software allows the user to choose between the Hertz-Sneddon and DMT mechanical contact models to calculate Young's modulus (elasticity) of the indented cell sample. Due to the shape of the chosen cantilever probes, the Hertz-Sneddon contact model (for the conical probe geometry) was applied to determine the elastic modulus of the cells for each force-displacement curve obtained (Fig. 2-7). Also, the JPK SPM data processing software has the option to apply the selected functions to all derived force curves. Since choosing the contact point to fit the Hertz-Sneddon model is done manually, force curves procced one by one in order to fit the model from the contact point on each curve (point where curve start to rise). It is clear that finding the first contact point is impossible due to the presence of large number of data close to each other and the

fluctuation of the curve around the contact point. Therefore, selecting the contact point might vary from one person to another. To test how this variation can effect on the calculated Young's elastic modulus the curve presented in Fig. 2-7 is fitted with the Hertz-Sneddon model for twenty times at the contact point and the calculated Young's elastic modulus is presented in Table 2-1.

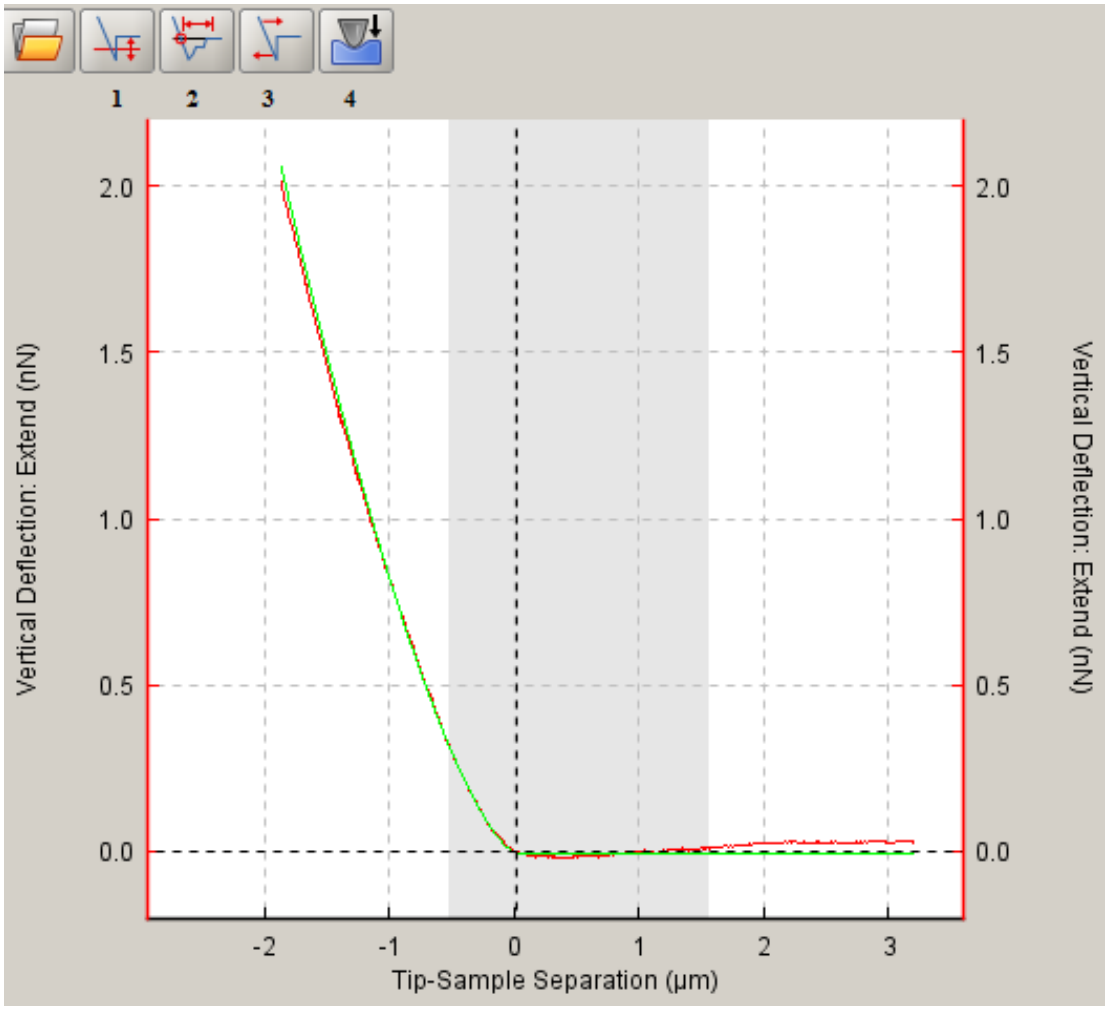

Figure 2-7. AFM force-displacement curve following the application of the 1- Baseline subtraction 2- Contact point determination and 3- Tip-sample separation 4- Hertz-Sneddon contact model elasticity fit. The red curve is the approach curve, the vertical black dashed line crosshairs shows the contact point of the approach curve, and the green line denotes the fit of Hertz-Sneddon's contact model. The grey shaded region represents the area selected by the user to be considered for the elasticity calculation.

Table 2-1. Young's elastic modulus derived from fitting the Hertz-Sneddon model in one force-indentation curve to study the variability of the derived Yong's elastic modulus based on the selected contact point.

Number	Calculated E (kPa)
1	3.129
2	3.082
3	2.927
4	3.006
5	2.997
6	3.016
7	3.012
8	3.201
9	3.136
10	2.945
11	3.040
12	3.113
13	3.215
14	3.190
15	3.104
16	3.047
17	2.946
18	3.181
19	3.033
20	2.931

From Table 2-1, it can be seen that the largest and smallest derived Young's elastic modulus are 3.215 kPa and 2.927 kPa respectively. For all obtained Young's elastic modulus the derived error is 0.114 kPa, which shows that the variability is low and negligible.

2.9 Gnuplot software

Where application of the newly developed model, based on the elastic shell theory (Chapter 3, section 3.7) for elastic modulus calculation was required, the Gnuplot software (version 4.4) has been used. To correctly apply the newly developed model, force map sets were exported from the JPK software and uploaded for processing and application of the model in Gnuplot. To do this, all force-displacement data files from the NanoWizard AFM were imported into the JPK data processing software as compressed binary file formats. These formats could only be read by the JPK SPM data processing software. To apply the newly developed model using Gnuplot, compressed binary files were saved as txt, formatted split force-displacement files. This then allowed the force-displacement data files to be correctly uploaded and processed in the Gnuplot software tool. The panel to write the code and the panel to show the plotted curve have been presented in Fig. 2-8.

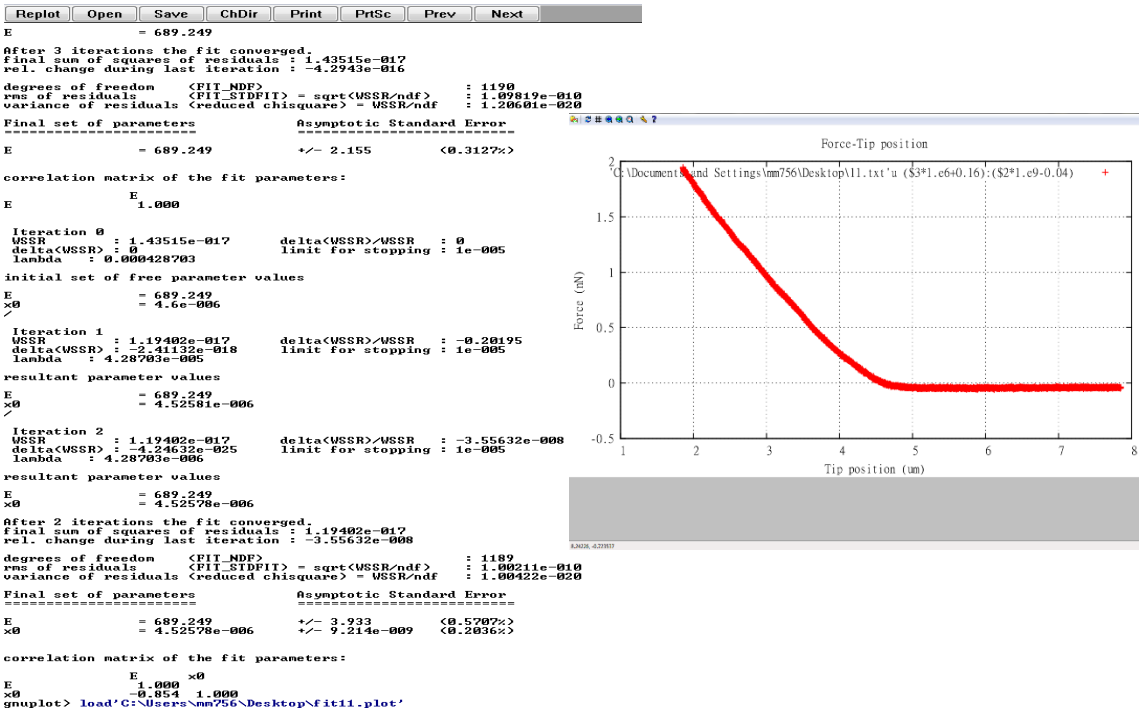

Figure 2-8. The panels for coding and plotting in Gnuplot software version 4.4.

CHAPTER 3

Mechanical modelling of the biological samples

Contents

3.1 Introduction

Analysing the elastic properties of cells requires understanding of the concept of the statistical and continuum mechanics. In a non-deformed body, arrangements of all the parts are in a way to achieve the mechanical equilibrium. So, at any portion of the body the sum of the action of forces on that part is zero. Applying external force on the body results in changes in volume and shape. This deformation can be explained in the form of the strain and stress tensors (see sections 3.2 and 3.3 for more details). Finding the relation between strain and stress tensors helps us to calculate free energy of the deformed body and correspondingly the relation between the applied force and the elastic modulus [71].

As discussed in Chapter 1 section 1.3.1, among different mechanical models, the Hertz contact model is the widely-applied model to measure the mechanical properties of the elastic solids. The model was developed based on the two in contact glass lenses, with considering the bodies are elastic half-space with an infinite sample thickness[26]. Hertz model has been widely applied for characterization of the mechanical properties of microorganisms such as cells. However, due to the assumptions on which the model is developed, it has limitations to provide accurate information about mechanical properties of cells. For instance, the Hertz model assuming sample thickness as infinite. Therefore,

for obtaining the elastic modulus from derived force-displacement curves from indenting the cells with an AFM, the model can only be applied for cellular deformations of less than 10% [72]. So, to derive the elastic modulus of the cells, only the first 200-300 nm of force-displacement curve can be fitted to the Hertz model.

Due to the limitations of the Hertz model, in this Chapter we investigated the development of a new model based on the elastic shell theory. To develop the model, thickness of a cell membrane and changes in the size of the cell due to deformation are taken into consideration. Also, the geometry and shape of the cell and the indenter were involved in the calculations.

It is hoped that the new model can provide more information about different aspects of the cells (e.g. elasticity and size changes), which can be later used for the other applications such as designing the separation techniques.

In this Chapter, first we explained the useful terms such as strain and stress tensors. Also, the elastic modulus and Poisson's ratio are explained using the Hook's law. In the next step, the deformation of the shells and developing the model are explained by using the elastic shell theory. There are considerable verity of the analytical approaches and notation conventions due to the different spectrum of disciplines. Here we used Landau and Lifshitz method as a reference [71].

In addition, where required the Einstein summation was applied for simplifying expressions including summations of vectors and tensors. The essential three rules of Einstein summation are:

1- Repeated indices are implicitly summed over.
2- Each index can appear at most twice in any term.
3- Each term must contain identical non-repeated indices.

According to this summation rule, when an index variable appears twice in a single term with no other definition, it implies summation of that term over all the values of the index [73].

3.2 Strain tensor

When a body deforms the position of the points within the body change. The relative change in the position of points within the deformed body can be define as strain. To explain it in the co-ordinate system we can consider a body in which the position of any point in it can be defined by its radius vector r (x_1, x_2, x_3). Deformation causes all the points in the body to undergo the displacement. Considering a specific point in the body,

its radius vector before and after deformation are r with co-ordinates (x_i) and r' with co-ordinates (x'_i) respectively. Suffix i refers to the component of the vector. The difference in the position of the chosen point due to the deformation is shown by the displacement vector and is given by:

$$\epsilon_i = x'_i - x_i \tag{3-1}$$

The co-ordinates of the displaced point (x'_i), is the function of the co-ordinates (x_i) before displacement. Therefore, it can be said that $\epsilon_i = \epsilon(x_i)$.

In a body, also, deformation causes the distances between the points to change too. To explain it we can consider two points near to each other in the body. If the radius vector joining them before the deformation denotes by dx_i then the radius vector after deformation can be shown by:

$$dx'_i = dx_i + d\epsilon_i \tag{3-2}$$

The distance between the two points before and after the displacement can be calculate by:

$$dx = \sqrt{(dx_1^2 + dx_2^2 + dx_3^2)}$$
$$dx' = \sqrt{(dx_1'^2 + dx_2'^2 + dx_3'^2)} \tag{3-3}$$

We can write the above equations as: $dx^2 = \sum_i dx_i^2$ and $dx'^2 = \sum_i dx_i'^2$. So, Eq. (3-2) can be written in the form of:

$$\sum_i dx_i'^2 = (dx_i + d\epsilon_i)^2 \tag{3-4}$$

Where $d\epsilon_i = (\frac{\partial \epsilon_i}{\partial x_j})dx_j$ obtained from a contravariant tensor transformation rule (A contravariant tensor is a tensor having specific transformation properties).

Expanding Eq. (3-4) we have:

$$dx_i'^2 = dx_i^2 + 2\frac{\partial \epsilon_i}{\partial x_j}dx_i dx_j + \frac{\partial \epsilon_i}{\partial x_j}\frac{\partial \epsilon_i}{\partial x_k}dx_j dx_k \tag{3-5}$$

If we write the second term in the above equation in the explicit symmetrical form:

$$2\frac{\partial \epsilon_i}{\partial x_j} dx_i dx_j = \left(\frac{\partial \epsilon_i}{\partial x_j} + \frac{\partial \epsilon_j}{\partial x_i}\right) dx_i dx_j \tag{3-6}$$

By interchanging the suffixes i and k in the third term in the Eq. (3-5) it can be written in the form of:

$$dx_i'^2 = dx_i^2 + 2\epsilon_{ij} dx_i dx_j \tag{3-7}$$

Then the strain tensor is defined as:

$$\epsilon_{ij} = \frac{1}{2}\left(\frac{\partial \epsilon_i}{\partial x_j} + \frac{\partial \epsilon_j}{\partial x_i} + \frac{\partial \epsilon_k}{\partial x_i}\frac{\partial \epsilon_k}{\partial x_j}\right) \tag{3-8}$$

Where the ϵ_{ij} is the symmetrical strain tensor.

Practically, in most situations of interest, strains are small. So, when a body undergoes a small deformation, all the strain components are small. However, even for the small strains the displacement vector can be large. There is an exception case where the body is spherical. In the spherical bodies, small deformations cause small displacements too.

Since, for small deformation displacement vector is small, the third term in the Eq. (3-8) can be neglected. So, Eq. (3-8) for small deformations can be rewrite as:

$$\epsilon_{ij} = \frac{1}{2}\left(\frac{\partial \epsilon_i}{\partial x_j} + \frac{\partial \epsilon_j}{\partial x_i}\right) \tag{3-9}$$

For the later applications, it is important to have the components of the strain tensor in the spherical co-ordinates (using spherical co-ordinates r, θ and φ):

$$\epsilon_{rr} = \frac{\partial \epsilon_r}{\partial r} \tag{3-10}$$

$$\epsilon_{\theta\theta} = \frac{1}{r}\frac{\partial \epsilon_\theta}{\partial \theta} + \frac{\epsilon_r}{r} \tag{3-11}$$

$$\epsilon_{\varphi\varphi} = \frac{1}{r sin\theta}\frac{\partial \epsilon_\varphi}{\partial \varphi} + \frac{\epsilon_\theta}{r} cot\theta + \frac{\epsilon_r}{r} \tag{3-12}$$

3.3 Stress tensor

Before a body undergoes any deformation, all the parts in it are in thermal and mechanical equilibrium. Therefore, in any arbitrary portion of the body the action of forces on it is equal to zero. Applying an external force on a body causes the molecular arrangement changes and body loses its equilibrium. Internal forces therefore, arises to return the body to its original equilibrium state. These internal forces, which are the result of molecular interaction, are known as internal stresses. In fact, molecular forces have a very short range of action and they can affect only on the other molecules in their neighbourhood. So, in the theory of the elasticity these forces are known as a 'near-action' forces. Thus, the forces from the internal stresses can only act on the surface of the body.

By considering a portion of a body, the total force is equal to the sum of the all forces on the all volume elements in that portion of the body. So, we can write it as a volume integral:

$$\iiint F dV \tag{3-13}$$

Where F is the force per unit volume and dV is the volume element.

Based on the Newton's third law the total force is zero due to the action of the forces from different parts of the selected portion on each other. Therefore, the total force can be taken as the sum of the forces applied on the selected portion of the body from the portions surrounding it. As all the mentioned forces, can be refer as a near action forces so they act on the surface of the selected portion. So, for any portion of the body, each of the three components $\iiint F_i dV$ of all the internal stresses can be written as an integral over the surface. To transform all the three components of all the internal stresses from the volume integral to an integral over the surface, we used the divergence of a vector rule. Thus, the vector F_i is a divergence of a tensor of rank two and can be written as:

$$\nabla . F_i = \frac{\partial \sigma_{ij}}{\partial x_j} \tag{3-14}$$

Using the divergence theorem, the force on the volume can be written as an integral over the closed surface.

$$\iiint \nabla . F_i \; dV = \oiint \sigma_{ij} \, ds_j \tag{3-15}$$

Substituting Eq. (3-14) in Eq. (3-15) we have:

$$\iiint \frac{\partial \sigma_{ij}}{\partial x_j} dV = \oiint \sigma_{ij} \, ds_j \tag{3-16}$$

Where ds_j is the component of the surface element vector and σ_{ij} is the stress tensor.

Eq. (3-16) shows the integral of the force applied to the volume of the body, which is enclosed by the surface of the body. If the volume of the body exerts force on to the surface of that body, this force is equal with the one derived from Eq. (3-16) but with the opposite sign. Therefore, when the internal stresses apply force to the surface of the body equation is:

$$-\iiint \frac{\partial \sigma_{ij}}{\partial x_j} dV = -\oiint \sigma_{ij} \, ds_j \tag{3-17}$$

By considering a body undergoing hydrostatic compression (uniform compression from all sides), finding the stress tensor, the action of the pressure from inside of the body on the surface of it, is important. Since, the pressure is the same magnitude of the external force, it can be written as:

$$F = -p ds_i \tag{3-18}$$

Where p is the pressure and ds_i is the component of the surface element. Eq. (3-17) shows the relation between the force and the stress tensor. Therefore, from Eq. (3-17) and Eq. (3-18) we can find out:

$$\sigma_{ij} ds_j \; = -p ds_i \tag{3-19}$$

We can also, write the $-p ds_i$ as a $-p\delta_{ij} ds_j$ where δ_{ij} is a unit tensor. Substituting $-p\delta_{ij} ds_j$ in Eq. (3-19) we have:

$$\sigma_{ij} = -p\delta_{ij} \tag{3-20}$$

Here σ_{ij} is the stress tensor in the hydrostatic compression.

To keep the system in an equilibrium state all the internal stresses of all the volume elements must be balanced. Therefore, the equilibrium equation can be stated as:

$$F_i = \frac{\partial \sigma_{ij}}{\partial x_j} = 0 \tag{3-21}$$

If we consider a body, which is deformed by applying an external force on its surface element (Fds), to have an equilibrium state it must be balanced by the force exerted from the internal stresses:

$$F_i ds - \sigma_{ij} ds_i = 0 \tag{3-22}$$

We can write $ds_i = n_j ds$ where n_j is a unit vector. So, Eq. (3-22) can be written as:

$$\sigma_{ij}\, n_j = F_i \tag{3-23}$$

To have an equilibrium on the surface of the body, the above equation must be valid at each point of the surface.

3.4 The thermodynamics of deformation

To understand the thermodynamics of deformed body we can assume a body deformed with applying an external force. Displacement is small in a way that it can be written as $\delta\epsilon_i$. To determine the work done by the internal stresses over the volume of the body, we need to multiply the applied force by the displacement:

$$R = F_i * \delta\epsilon_i = \frac{\partial \sigma_{ij}}{\partial x_j} * \delta\epsilon_i \tag{3-24}$$

To determine the work done over the volume of the body, Eq. (3-24) can be written as an integration of the work over the volume:

$$\iiint \delta R dV = \iiint \frac{\partial \sigma_{ij}}{\partial x_j} \delta\epsilon_i dV \tag{3-25}$$

Using Eq. (3-16) and applying integration by parts rule, we can write above equation as:

$$\iiint \delta R dV = \oiint \sigma_{ij} \delta\epsilon_i \, ds_i - \iiint \sigma_{ij} \frac{\partial \delta\epsilon_i}{\partial x_j} dV \tag{3-26}$$

If we consider an infinite body, which is not deformed at infinity, the first integral in the above equations, which is over the surface tends to infinity. So, the stress tensor tends to zero and makes the whole integral become zero. Therefore, the Eq. (3-26) can be present as:

$$\iiint \delta R dV = -\iiint \sigma_{ij} \frac{\partial \delta \epsilon_i}{\partial x_j} dV \tag{3-27}$$

The integral on the right side can be expand by writing it in an explicit symmetrical way:

$$\iiint \delta R dV = -\frac{1}{2} \iiint \sigma_{ij} \left(\frac{\partial \delta \epsilon_i}{\partial x_j} + \frac{\partial \delta \epsilon_j}{\partial x_i} \right) dV \tag{3-28}$$

The expression in the parenthesis on the right side is the strain tensor so:

$$\iiint \delta R dV = -\frac{1}{2} \iiint \sigma_{ij} \delta \left(2\epsilon_{ij} \right) dV \tag{3-29}$$

$$\iiint \delta R dV = -\iiint \sigma_{ij} \delta \epsilon_{ij} dV \tag{3-30}$$

Therefore, we can find the work done by the internal stress as:

$$\delta R = -\sigma_{ij} \delta \epsilon_{ij} \tag{3-31}$$

Which, shows work as a function of the strain tensor.

There are two forms of deformations. First type is the elastic deformation in which, deformations are small and the deformed body can return to its original state after the external force has been removed. If the deformations are large and body cannot turn to its non-deformed state after the external force ceased, this deformation is called plastic. In our case, all the deformations are considered as an elastic deformation. In addition, to keep the thermodynamic equilibrium in the body, we assumed the deformation is slow. So, we can say that the process is thermodynamically reversible.

In the closed thermodynamic systems, the internal energy can be stated as a heat added to the system minus the work done on the system. This relation in the infinitesimal terms can be expressed using the differentials of each term (all thermodynamic quantities are taken on the unit volume of the non-deformed body).

$$dU = dQ - dR \tag{3-32}$$

In the reversible process the heat can be given as:

$$dQ = TdS \tag{3-33}$$

Where T is temperature and S is entropy.

Substituting Eq. (3-31) and Eq. (3-33) in Eq. (3-32) we can derive the fundamental equation for deformed bodies:

$$dU = TdS + \sigma_{ij} d\epsilon_{ij} \tag{3-34}$$

Using Eq. (3-20) we can write:

$$\sigma_{ij}\, d\epsilon_{ij} = -p\delta_{ij} d\epsilon_{ij} = \ -pd\epsilon_{ii} \tag{3-35}$$

As the deformation occurs on the unit volume of the body, so, ϵ_{ii} is the changes in the volume and therefore, $d\epsilon_{ii}$ is the volume element. We can write the Eq. (3-34) in the form of:

$$dU = TdS - pdV \tag{3-36}$$

Moreover, the Helmholtz free energy can be defined as:

$$H = U - TS \tag{3-37}$$

So, we can write:

$$dH = -SdT + \sigma_{ij} d\epsilon_{ij} \tag{3-38}$$

Furthermore, thermodynamic potential is:

$$\Phi = U - TS + pV = H - \sigma_{ij}\epsilon_{ij} \tag{3-39}$$

Substituting the Eq. (3-39) in Eq. (3-38) we have:

$$d\Phi = -SdT - \epsilon_{ij} d\sigma_{ij} \tag{3-40}$$

S and ϵ_{ij} in the Eq. (3-34) and T and ϵ_{ij} in the Eq. (3-38) are the independent variables. Therefore, stress tensor at constant entropy and temperature can be derived by differentiation of U or H with respect to the strain tensor:

$$\sigma_{ij} = \left|\frac{\partial U}{\partial \epsilon_{ij}}\right|_S = \left|\frac{\partial H}{\partial \epsilon_{ij}}\right|_T \tag{3-41}$$

Now to understand elasticity [E] and the Poisson's ratio [ν] we need to explain the Hooke's law.

3.5 Hooke's law and elastic moduli

It is important to express the free energy of a body as a function of strain, which means that for small deformations the free energy changes in powers of the strain tensor. This can help us to use the general thermodynamic equations, derived in the previous section, in special cases such as isotropic bodies.

Let's consider an isotropic deformed body at the constant temperature. Since, the free energy is scalar, and the strain is a tensor, free energy is a function of all components of the strain tensor: $H = H(\epsilon_{11}, \epsilon_{12}, \dots)$. In the linear elasticity, stress is also linear like the strain tensor. However, considering the Eq. (3-41), the free energy cannot expand linearly in powers of the stain tensor. Thus, the generalised Helmholtz free energy per unit volume due to strain is a sum of contributions:

$$H = \frac{1}{2}\sum_{ij} C_{ij}\epsilon_i\epsilon_j \tag{3-42}$$

Where the C_{ij} is a second rank symmetrical elastic stiffness tensor and Einstein summation has been used to imply summation over repeated indices.

The above equation can be written as a squared sum of the diagonal elements $(\epsilon_{ii})^2$ and sum of all the elements squared (ϵ_{ij}^2). Einstein summation has been used for the tensors, in which repeated indices are implicitly summed over. Therefore, for small strains free energy can be given as:

$$\begin{aligned} H = \frac{1}{2}C_{11}\epsilon_1^2 + \frac{1}{2}C_{12}\epsilon_1\epsilon_2 + \frac{1}{2}C_{13}\epsilon_1\epsilon_3 + \frac{1}{2}C_{22}\epsilon_2^2 + \frac{1}{2}C_{12}\epsilon_1\epsilon_2 \\ + \frac{1}{2}C_{23}\epsilon_2\epsilon_3 + \frac{1}{2}C_{13}\epsilon_1\epsilon_3 + \frac{1}{2}C_{33}\epsilon_3^2 \end{aligned} \tag{3-43}$$

Where the elastic stiffness for diagonal and non-diagonal components are:

$$C_{11} = C_{22} = C_{33} = C_1 \tag{3-44}$$

$$C_{12} = C_{13} = C_{23} = C_2 = \lambda \tag{3-45}$$

$$(C_1 - C_2)/2 = \mu \tag{3-46}$$

Here λ and μ are Lamé coefficients. So, we can write the equation for the free energy of an isotropic body as:

$$H = \frac{1}{2}\lambda(\epsilon_1 + \epsilon_2 + \epsilon_3)^2 + \mu(\epsilon_1^2+\epsilon_2^2+\epsilon_3^2) \tag{3-47}$$

$$H = H_0 + \frac{1}{2}\lambda(\epsilon_{ii})^2 + \mu\,\epsilon_{ij}^2 \tag{3-48}$$

Where H_0 is the free energy of the body before deformation and it can be omitted from the equation.

There are two ways to deform a body, pure shear and hydrostatic compression. Pure shear is when the deformation make changes in the shape of the body while its volume remains constant. Conversely, hydrostatic compression is a kind of deformation where the volume of the body changes but the shape stays unchanged. Therefore, total deformation can be write as a sum of the pure shear and the hydrostatic compression. It is well known that the sum of the principle values of a tensor is invariant and is equal to the sum of the diagonal components: $\epsilon_{ii} = \epsilon_{11} + \epsilon_{22} + \epsilon_{33}$. Taking this in to the consideration and to relate the Lamé coefficients to the elastic moduli we can rewrite the strain tensor as:

$$\epsilon_{ij} = \left(\epsilon_{ij} - \delta_{ij}\frac{1}{3}\epsilon_{kk}\right) + \delta_{ij}\frac{1}{3}\epsilon_{kk} \tag{3-49}$$

Where the first term on the right side of the equation is the pure shear and the second term represents the hydrostatic compression.

The free energy of the deformed body can be decomposed into two independent deformation modes by substituting Eq. (3-49) in to Eq. (3-48):

$$H = \frac{1}{2}\lambda(\epsilon_{kk})^2 + \mu[\left(\epsilon_{ij} - \delta_{ij}\frac{1}{3}\epsilon_{kk}\right) + \delta_{ij}\frac{1}{3}\epsilon_{kk}]^2 \tag{3-50}$$

Therefore:

$$H = \mu\left(\epsilon_{ij} - \delta_{ij}\frac{1}{3}\epsilon_{kk}\right)^2 + \frac{1}{2}\left(\lambda + \frac{2}{3}\mu\right)(\epsilon_{kk})^2 \tag{3-51}$$

Again, in the above equation the first term on the right side shows the pure shear and the second term is hydrostatic compression. Also, the term $\lambda + \frac{2}{3}\mu$ is called bulk modulus (or modulus of compression) and can be shown by K and μ is the modulus of rigidity. Therefore, free energy can be rewrite as:

$$H = \mu\left(\epsilon_{ij} - \delta_{ij}\frac{1}{3}\epsilon_{kk}\right)^2 + \frac{1}{2}K(\epsilon_{kk})^2 \tag{3-52}$$

In addition, the quadratic form of the above equation indicates that both K and μ must be positive otherwise the system could deform spontaneously by a shear or compression modes.

To find the stress-strain relation using Eq. (3-41) we need to find the derivation of the free energy:

$$dH = 2\mu\left(\epsilon_{ij} - \frac{1}{3}\delta_{ij}\epsilon_{kk}\right)d\left(\epsilon_{ij} - \frac{1}{3}\delta_{ij}\epsilon_{kk}\right) + (K\epsilon_{kk})d(\epsilon_{kk}) \tag{3-53}$$

Substituting $d(\epsilon_{kk}) = \delta_{ij}d\epsilon_{ij}$ we can write:

$$dH = \left[2\mu\left(\epsilon_{ij} - \frac{1}{3}\delta_{ij}\epsilon_{kk}\right) + K\epsilon_{kk}\delta_{ij}\right]d\epsilon_{ij} \tag{3-54}$$

Therefore, the stress tensor of an isotropic body at the constant temperature throughout the body is:

$$\sigma_{ij} = \left(\frac{\partial H}{\partial \epsilon_{ij}}\right)_T = 2\mu\left(\epsilon_{ij} - \frac{1}{3}\delta_{ij}\epsilon_{kk}\right) + K\epsilon_{kk}\delta_{ij} \tag{3-55}$$

To calculate the strain tensor (ϵ_{ij}), first we need to derive the sum of the diagonal terms in the stress tensor. To do so, the Eq. (3-55) can be written inversely to find the sum of the diagonal terms (σ_{ii}). Since, δ_{ii}=3, sum of the diagonal terms in the first term on the right side, which represents the pure shear is zero. So, the strain tensor for the diagonal terms is:

$$\epsilon_{ii} = \frac{1}{3K}\sigma_{ii} \tag{3-56}$$

By substituting the Eq. (3-56) in the Eq. (3-55) strain tensor can be obtained as:

$$\epsilon_{ij} = \frac{\sigma_{ij} - \frac{1}{3}\delta_{ij}\sigma_{kk}}{2\mu} + \frac{\delta_{ij}\sigma_{kk}}{9K} \tag{3-57}$$

It can be seen from the above equation that there is a linear relation between strain tensor and stress tensor. So, in the isotropic bodies the deformation is proportional to the applied force. This rule which is known as a Hooke's Law is valid for almost all elastic deformation when they are small.

Moreover, the free energy of the deformed body can be expressed by using the Euler's homogenous function theorem, per volume of the body. For the homogenous functions of the order "n" it can be written:

$$x_i \frac{\partial f}{\partial x_i} = nf(x) \tag{3-58}$$

From Eq. (3-48) it can be seen that the free energy is quadratic in the strain tensor, so:

$$\epsilon_{ij} \frac{\partial H}{\partial \epsilon_{ij}} = 2H \tag{3-59}$$

Thus, substituting Eq. (3-41) in the above equation, free energy of the deformed body per volume of it is:

$$H = \frac{1}{2}\sigma_{ij}\epsilon_{ij} \tag{3-60}$$

In the next step, the elastic modulus and Poisson's ratio are explained. So, we considered the body homogeneously deformed. Hydrostatic compression is a good example of homogeneous deformation in which the strain tensor is constant per volume of the body. The simple case is a rod which is uniformly thin and it lies along the z-axis and the force is applied along the same axis. Therefore, all components of σ_{ij} are zero except σ_{zz}. Since the stress is:

$$\sigma_{zi} n_i = \sigma_{zz} = p \tag{3-61}$$

Using it, the Eq. (3-57) can be solved for components of the strain and stress tensors:

$$\epsilon_{xx} = \epsilon_{yy} = \frac{1}{3}\left(\frac{1}{3K} - \frac{1}{2\mu}\right)p \tag{3-62}$$

$$\epsilon_{zz} = \left(\frac{1}{3\mu} + \frac{1}{9K}\right)p \tag{3-63}$$

Where the ϵ_{zz} shows the relative lengthening of the body and the term in the parenthesis is called Young's modulus, which is shown by E:

$$\epsilon_{zz} = \frac{p}{E} = \frac{9K\mu}{3K + \mu} \tag{3-64}$$

$$E = \frac{9K\mu}{3K + \mu} \tag{3-65}$$

The Poisson's ratio (coefficient of expansion) can, also be explained as the negative ratio of transverse compression to axial extension:

$$-\frac{\epsilon_{xx}}{\epsilon_{zz}} = \nu \tag{3-66}$$

Substituting Eq. (3-62) and Eq. (3-63) in the above equation, the Poisson's ratio derived as:

$$\nu = \frac{3K - 2\mu}{2(3K + \mu)} \tag{3-67}$$

As we discussed above K and μ are the positive parameters so, for the K=0, Poisson's ratio is -1 and for the μ=0, it is 0.5. Therefore, it can be said that for the isotropic bodies the Poisson's ratio cannot be less than -1 and not bigger than 0.5:

$$-1 \leq \nu \leq 0.5 \tag{3-68}$$

We can rearrange the Eq. (3-65) and Eq. (3-67) to have K and μ:

$$K = \frac{E}{3(1 - 2\nu)} \tag{3-69}$$

$$\mu = \frac{E}{2(1 + \nu)} \tag{3-70}$$

Moreover, using Eq. (3-55) and substituting the derived equations of K and μ the stress tensor is obtained as a function of the strain tensor:

$$\sigma_{ij} = \frac{E}{1+\nu}\left(\epsilon_{ij} + \frac{\nu}{1-2\nu}\delta_{ij}\epsilon_{zz}\right) \tag{3-71}$$

We can converse the above equation to find the strain tensor:

$$\epsilon_{ij} = \frac{\left[(1+\nu)\sigma_{ij} - \nu\delta_{ij}\sigma_{ii}\right]}{E} \tag{3-72}$$

3.6 Bending energy of membranes

In the cell, the lipid bilayer is a component of the membrane, which has a thickness that is much smaller than the length scale of the cell. Therefore, the lipid bilayer can be assumed as a two-dimensional system over the surface.

Applying a positive tension on one monolayer and a negative tension on the other monolayer results in a bending moment [M]. Curved surface can be characterised by calculating the mean curvature:

$$mean\ curvature = \frac{1}{R_1} + \frac{1}{R_2} \tag{3-73}$$

Here, R_1 and R_2 are the principal radii of curvature which measured along two perpendicular directions.

Using the Hook's law the moment of bending can be calculated from:

$$M = K_c\left(\frac{1}{R_1} + \frac{1}{R_2}\right) \tag{3-74}$$

Where, K_c is the bending rigidity$\left(K_c = \frac{ET^3}{24(1-\nu^2)}\right)$.

Physically meaningful quantities constructed from the radii of curvature should depend on the value of the mean curvature [74, 75]. Thus, the bending energy must take the form of:

$$H_b = \frac{1}{2}K_c \oiint \left(\frac{1}{R_1} + \frac{1}{R_2}\right)^2 ds = \frac{ET^3}{48(1-\nu^2)} \oiint \left(\frac{1}{R_1} + \frac{1}{R_2}\right)^2 ds \tag{3-75}$$

3.7 Deformation of shells

A shell can be defining as a plate which is curved in its non-deformed state with uniform thickness [T]. Here, the shell's thickness is assumed to be much smaller than the other dimensions in the other directions. We also assumed shell as an isotropic, linear elastic

body with the Young's modulus [E] and Poisson's ratio [ν]. For simplicity, it is assumed that the shell is homogeneous and thermal expansions are neglected.

The important points in deformation of the shells are stretching and bending energies. Generally, for very thin membranes stretching energy is the main energy due to large tensile stresses. However, bending energy near the deformed parts of the sample is relatively high. Using Eq. (3-60) the stretching energy of a deformed shell is obtained from:

$$H_s = \frac{T}{2} \oiint \epsilon_{ij}\, \sigma_{ij} ds \tag{3-76}$$

Where H_s is the stretching energy of the body derived from the integral over the surface of the entire body [ds]. T is the thickness of the shell membrane, ϵ_{ij} and σ_{ij} are two-dimensional strain and stress tensors respectively.

To employ the shell theory to cells we assumed they are a "bag" filled with an incompressible liquid. So, the volume of the cells stay constant and mechanical changes (e.g. elastic properties) of the surface are taking into the consideration. For small deformations, also, the shape of the cells remains spherical, except in the contact points. As the main aim is to find a relation between the applied force and the Young's elastic modulus, first we need to find the stretching and bending energies of the cell. We shall start with a simple example where a spherical cell deforms uniformly subjecting to the force from a plate (Fig. 3-1) [39].

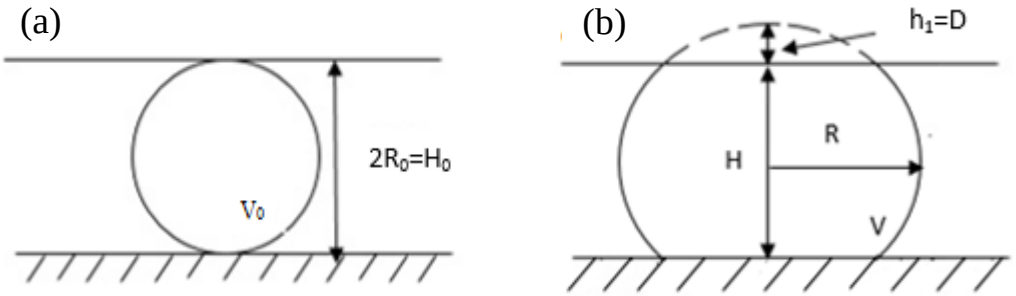

Figure 3-1. A spherical cell at its (a) non-deformed state and (b) after deformation under a uniform force of a plate. Here, h_1 is the height of the deformed parts and D shows the total deformation where in this case it is equal to the h_1. R_0 and R are the radius of the cell before and after deformation respectively. H is the height of the non-deformed part. V_0 and V are the volume of the cell before and after the deformation respectively, which, due to the incompressibility of the liquid, assumed to be constant.

Using a spherical co-ordinate system for the spherical cells, we can say that the deformation is radial [r]. So, φ and θ are two dimensional co-ordinates on the surface of the shell, which are polar and azimuthal angels respectively, as shown in Fig. 3-2. By applying the radial force on the cells, the respond to the force coming from the tensile stresses arise from the surface of the cell. The tensile stresses acting tangentially on the surface membrane of the cell to balance the pressure inside of the cell. Therefore, the pressure can be defining as:

$$P = \frac{T}{R}(\sigma_{\theta\theta} + \sigma_{\varphi\varphi}) \tag{3-77}$$

The stress tensors act on the surface of the surface elements of the sample. As the component are equal therefore, $\sigma_{\theta\theta} = \sigma_{\varphi\varphi}$.

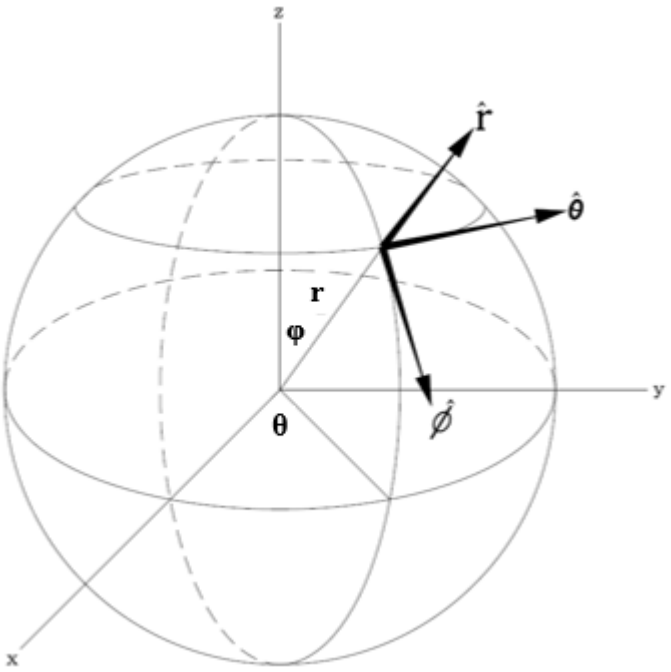

Figure 3-2. Schematic of the spherical co-ordinate system. Here, r is the radial distance from a point to the centre, φ is the polar angle and θ is the azimuthal angle.

To calculate the stretching energy, we can use Eq. (3-71), where stress tensor is related to the strain tensor. Therefore, the stress tensor for the φ and θ angles is given by:

$$\sigma_{\theta\theta} = \sigma_{\varphi\varphi} = \frac{E}{1+\nu}\epsilon_{\theta\theta} = \frac{E}{1+\nu}\epsilon_{\varphi\varphi} \tag{3-78}$$

And the strain tensor can be obtained from substituting the Eq. (3-10) in the Eq. (3-11):

$$\epsilon_{\theta\theta} = \frac{1}{r}\left(\frac{\partial \epsilon_\theta}{\partial \theta} + \frac{\partial \epsilon_r}{\partial r}\right) \tag{3-79}$$

By considering the symmetrical radial deformation, the first term in the parenthesis is zero and the second term is (R-R_0). So, the strain tensor for the φ and θ angles can be obtained as:

$$\epsilon_{\theta\theta} = \epsilon_{\varphi\varphi} = \frac{1}{R}(R - R_0) \tag{3-80}$$

Substituting Eq. (3-80) in Eq. (3-78) we derived:

$$\sigma_{\theta\theta} = \sigma_{\varphi\varphi} = \frac{E}{1+\nu}\frac{(R - R_0)}{R} \tag{3-81}$$

Now we are able to calculate the stretching energy of the cell. The stretching energy (H_s), which is over the surface of the sample can be calculated by substituting the Eq. (3-80) and Eq. (3-81) in Eq. (3-76):

$$\begin{aligned} H_s = \frac{T}{2}\oiint \frac{(R - R_0)}{R}\frac{E}{1+\nu}\frac{(R - R_0)}{R} ds = \frac{TE}{2(1+\nu)}\frac{(R - R_0)^2}{R^2} 4\pi R^2 \\ = \frac{2\pi TE}{1+\nu}(R - R_0)^2 \end{aligned} \tag{3-82}$$

It is obvious from the Eq. (3-82) that to find the stretching energy we need to calculate the radius of the cell after deformation. Using the assumption of the constant volume, we have:

$$V_0 = V \tag{3-83}$$

$$\frac{4}{3}\pi R_0^3 = \frac{4}{3}\pi R^3 - \frac{2}{3}\pi D^2(3R - D) \tag{3-84}$$

In the above equation, the second term on the right side shows the equation for the volume of a spherical caps from the top and bottom of the cell subtracted from the whole volume of it after deformation. The spherical cap from top and bottom of the sample are equal. Eq. (3-84) can get the final form of:

$$4R^3 - 4R_0^3 - 6RD^2 + 2D^3 = 0 \tag{3-85}$$

It can be seen from the above equation that R is explicitly depend on the indentation depth. Since, R changes as a function of D (R=R(D)), it can be said that the stretching

energy is a function of indentation depth ($H_s=H_s(D)$) too. For small indentations ($D \leq \frac{R_0}{10}$), changes in the radius of a cell as a function of indentation depth is plotted in Fig. 3-4 (a). Also, applying Eq. (3-82) changes in the stretching energy of the cell is plotted as a function of indentation depth Fig. 3-4 (b). In all calculations R_0 had the value of 9 μm, which is measured before indentation. Using an AFM, the indentation depth [D] can be obtained from the force-displacement curve (Fig. 3-3). Therefore, by knowing R_0 and D, the radius of the sample after indentation [R] can be derived from the Eq. (3-85). For stretching energy calculation, the term $2\pi TE/1+\nu$ is assumed to be 10^4 nN/μm. From Fig. 3-4 (a), it is clear that the new radius [R] and indentation depth have a non-linear relation. Also, the maximum change in the radius of the cell at the indentation depth of 3 μm is obtained as 0.46 μm. Since the applied indenter is flat, the calculated change in the radius of the cell is reasonable as it was expected to be. Also, Fig. 3-4 (b) shows while the stretching energy has non-linear relation with the indentation depth, it increases faster as the indentation depth increases.

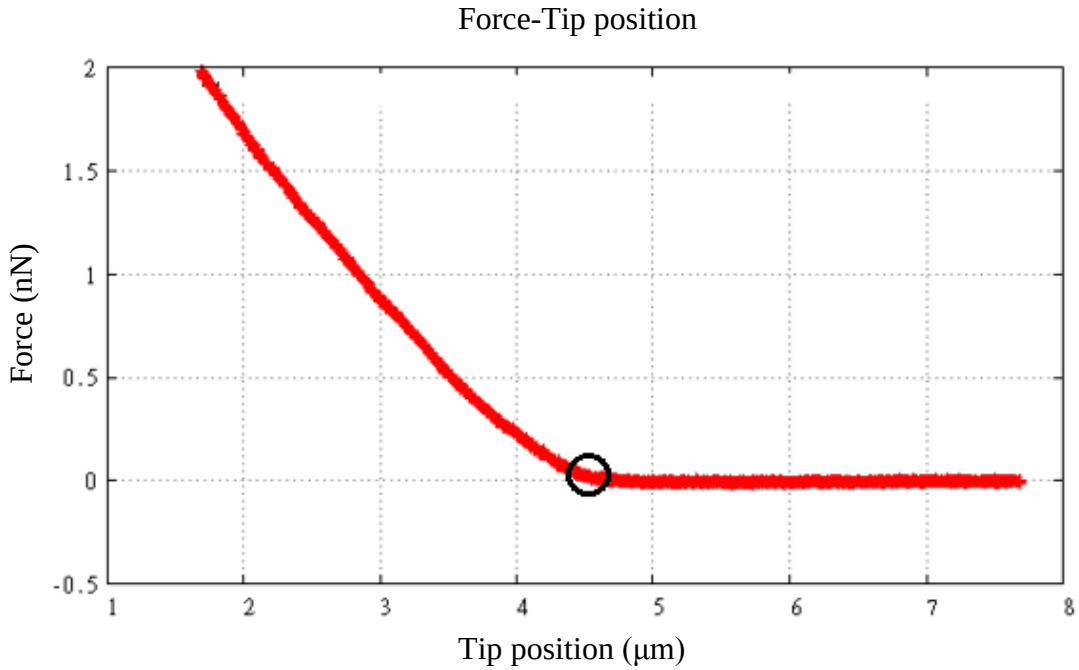

Figure 3-3. Force curve obtained from indenting a cell using AFM. It shows changes in the position of a tip (indentation) vs. applied force. The baseline shows movement of the tip to approach to the cell. The black circle shows the point where the tip touches the cell for the first time. The point where the curve starts to rise up is where the value for force is not zero anymore and can be used as a reference to calculate the indentation depth [D].

To obtain bending energy in the deformed area, Eq. (3-75) can be use:

$$H_b = \frac{ET^3}{48(1-\nu^2)} \oiint (\frac{1}{R_1} + \frac{1}{R_2})^2 \, ds = \frac{ET^3}{36} \left(\frac{1}{R_1} + \frac{1}{R_2}\right)^2 (2\pi RD) \qquad (3\text{-}86)$$

Comparing the stretching energy of the deformed cell with the bending energy, it can be seen that due to the term T^3 in the bending energy, it is quite smaller than the stretching energy. Therefore, it is convenient to neglect it from the calculations.

Finally, force can be determined by applying partial differentiation on the stretching energy over the indentation depth:

$$F_D = \frac{\partial H_s}{\partial D} = (4\pi T \frac{E}{1+\nu}(R - R_0)) \frac{\partial R}{\partial D} \qquad (3\text{-}87)$$

The term $\partial R/\partial D$ needs to be calculated from Eq. (3-85):

$$\frac{\partial R}{\partial D} = \frac{2DR - D^2}{2R^2 - D^2} \qquad (3\text{-}88)$$

Therefore, the final form of Eq. (3-87) is:

$$F_D = \frac{\partial H_s}{\partial D} = (4\pi T \frac{E}{1+\nu}(R - R_0)) \frac{2DR - D^2}{2R^2 - D^2} \qquad (3\text{-}89)$$

Eq. (3-89), can be applied to calculate the Young's elastic modulus of a cell deformed under the flat indenter force. Using Eq. (3-89), it is possible to plot the applied force as a function of indentation depth (Fig. 3-4 (c)). To plot force versus indentation depth, force was calculated for small indentations ($D \leq \frac{R_0}{10}$). Also, the value of 9 μm is used as an initial radius of the cell. The term $4\pi TE/1+\nu$ is also, assumed to be 10^4 nN/μm. It can be observed from the plotted curve, force and indentation depth have a non-linear relation. Moreover, referring to the curves plotted in Fig. (3-4), it is objective that finding the real first contact point is almost impossible.

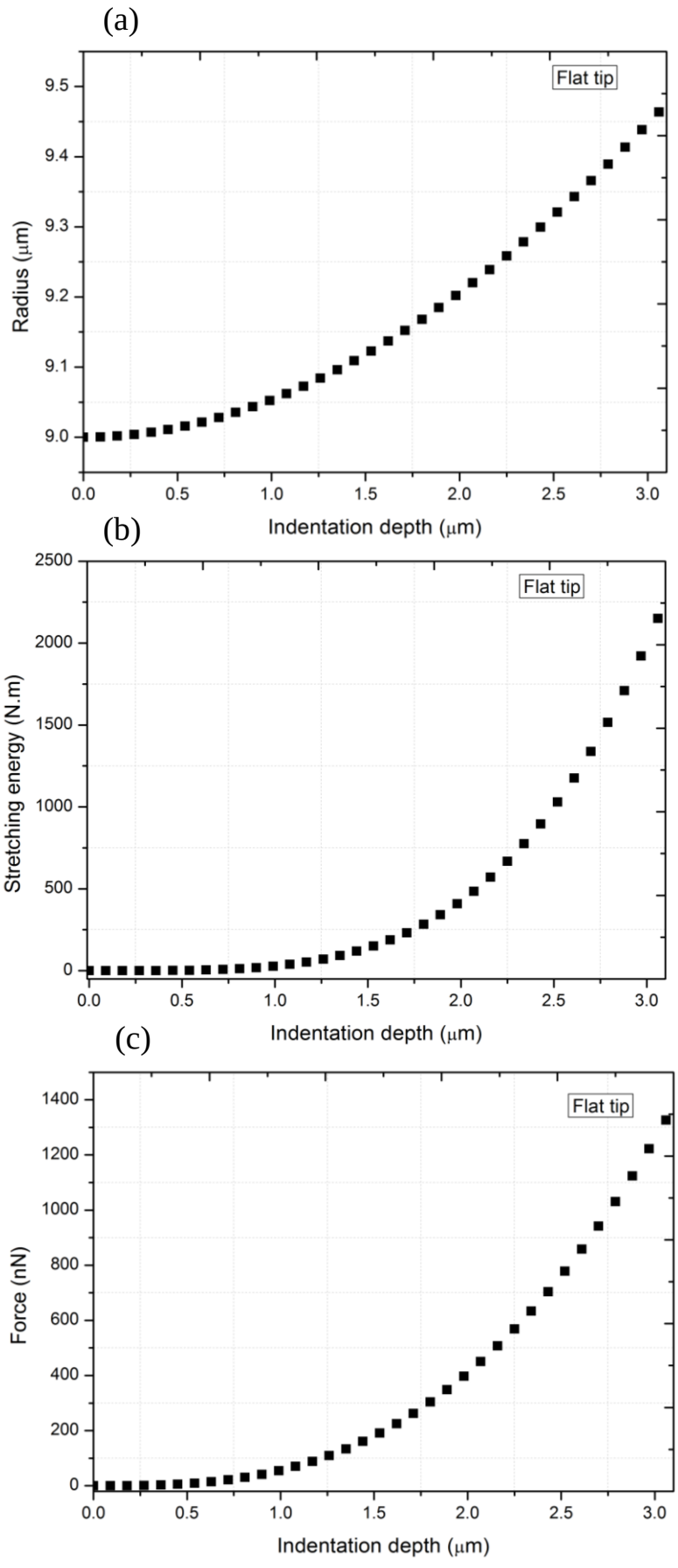

Figure 3-4. Relation between indentation depths with (a) obtained radius after deformation (b) resultant stretching energy and (c) force, by applying a flat indenter.

In the next step, flat indenter is replaced with a conical tip. Changes in the shape of the spherical cell after indentation is presented in (Fig. 3-5).

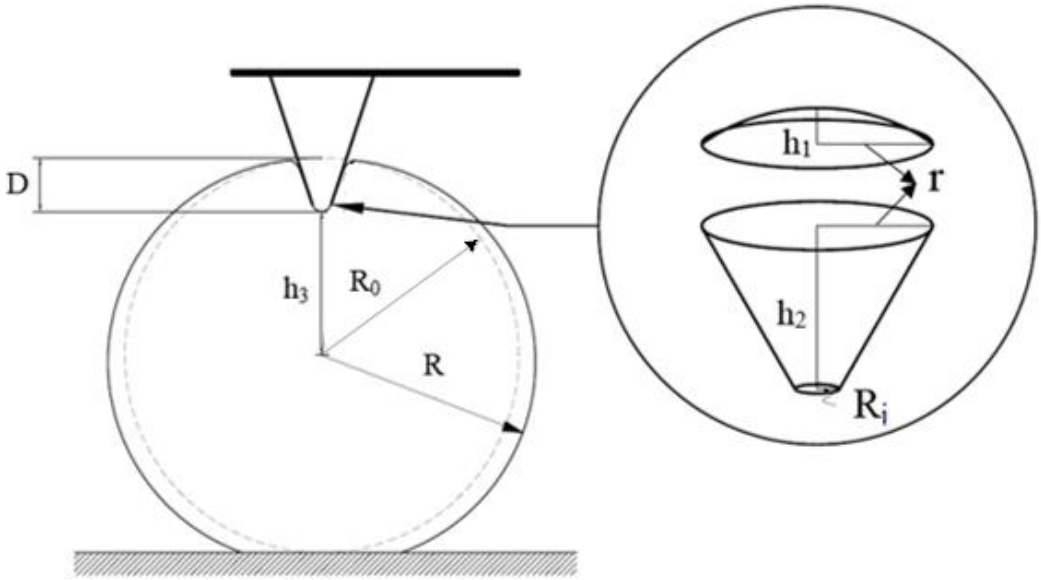

Figure 3-5. Schematic of the spherical cell indented with a conical tip: non-deformed (shown by dashes) and deformed states (solid line). R_0 is initial radius of the cell, R is radius after indentation, R_i is radius of the tip, h_1 is the height from the top spherical cap, h_2 is height of truncated cone, r is radius of the base circle, h_3 is the distance between the deformed part to the centre of sphere and D is total deformation.

From Fig. 3-5, it can be seen that for small deformations, h_1 from the top spherical cap is very small, which can be neglected from the calculations. Also, the same spherical cap from the bottom of the cell is neglected too. Therefore, total indentation depth can be equal to h_2:

$$D = h_2 \tag{3-90}$$

Value for r is calculated using the trigonometric functions for the right triangle, which is presented in Fig. 3-6.

Therefore, the equation to calculate r is:

$$r = (D + d)\tan\alpha \tag{3-91}$$

Where, α is the half tip cone angle. And d can be find from:

$$d = \frac{R_i}{\tan\alpha} \tag{3-92}$$

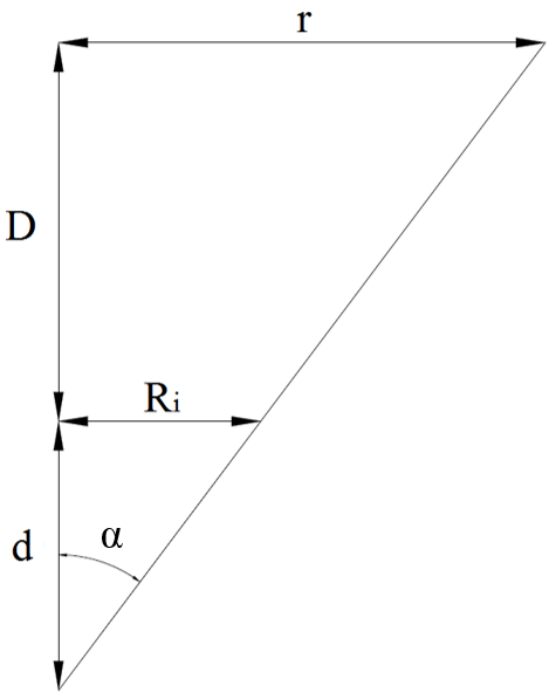

Figure 3-6. The trigonometric functions were used to calculate r.

In the next step, the stretching energy need to be calculated, using Eq. (3-76). The stretching energy (H_s), which is over the surface of the spherical sample is calculated from Eq. (3-93). Therefore, stretching energy is:

$$H_s = \frac{T}{2}\oiint \frac{(R-R_0)}{R}\frac{E}{1+\nu}\frac{(R-R_0)}{R}ds = \frac{TE}{2(1+\nu)}\frac{(R-R_0)^2}{R^2}4\pi R^2 = \frac{2\pi TE}{1+\nu}(R-R_0)^2 \quad (3\text{-}93)$$

It is clear from above equation that to determine the stretching energy, radius of the cell after indentation [R] required to calculate. To do so, the assumption of the constant volume, (V_0=V) was used. Therefore, while the non-deformed cell volume was spherical, the volume of the deformed cell by the conical tip, assumed to be a sphere mines one spherical cap and one truncated cone from the top of the cell and one spherical cap from the bottom (Fig. 3-5). However, for small indentations the spherical caps are ignored and only the truncated cone is taken into the calculations. Therefore, the equation to calculate radius after deformation [R] for the small indentations can be written as:

$$\frac{4}{3}\pi R_0^3 = \frac{4}{3}\pi R^3 - [\frac{\pi}{3}D(R_i^2 + r^2 + rR_i)] \quad (3\text{-}94)$$

With some simplifications, the final equation was obtained as:

$$4R^3 - 4R_0^3 - DR_i^2 - Dr^2 - DrR_i = 0 \quad (3\text{-}95)$$

It can be seen that the Eq. (3-95) is a cubic equation and since all of the coefficients are real numbers, therefore, there will be at least one real root for R. To reduce the variables in Eq. (3-95) [r] is replaced by Eq. (3-91). Therefore, the Eq. (3-95) can take the final format of:

$$4R^3 - 4R_0^3 - DR_i^2 - D(D+d)^2 \tan\alpha^2 - DR_i(D+d)\tan\alpha = 0 \quad (3\text{-}96)$$

Finally, to calculate the elastic Young's modulus, relation between the applied force and resultant indentation depth needed to be determined:

$$F_D = \frac{\partial H_s}{\partial D} \quad (3\text{-}97)$$

Where $\partial H_s/\partial D$ is:

$$\frac{\partial H_s}{\partial D} = 4\pi T \frac{E}{1+\nu}(R - R_0)\frac{\partial R}{\partial D} \quad (3\text{-}98)$$

It can be seen that, to use Eq. (3-98), the value for $\frac{\partial R}{\partial D}$ required to be obtained. To do so, the partial differentiation of Eq. (3-96) was calculated:

$$\frac{\partial R}{\partial D} = \frac{3R_i^2 + 3D^2\tan\alpha^2 + 6DR_i\tan\alpha}{12R^2} \quad (3\text{-}99)$$

Replacing the Eq. (3-99) in the Eq. (3-98) the equation for F_D got the final form as:

$$F_D = 4\pi T \frac{E}{1+\nu}(R - R_0)\frac{3R_i^2 + 3D^2\tan\alpha^2 + 6DR_i\tan\alpha}{12R^2} \quad (3\text{-}100)$$

After obtaining the required equations, the same tests as performed for the flat indenter, is applied to the conical tip. Changes in the radius of the cell [R], stretching energy [H_s] and force [F] as the functions of indentation depth are obtained and plotted in Fig. 3-7. The initial radius [R_0] of the cells were measured prior to the indentation and the total indentation depth [D] was derived from the force-displacement curves obtained from the AFM (Fig. 3-3). Calculations were done for small indentations ($D \leq \frac{R_0}{10}$), with the initial radius of 9 μm. In stretching energy and force equations the terms $2\pi TE/1+\nu$ and $4\pi TE/1+\nu$ are assumed to be 10^4 nN/μm.

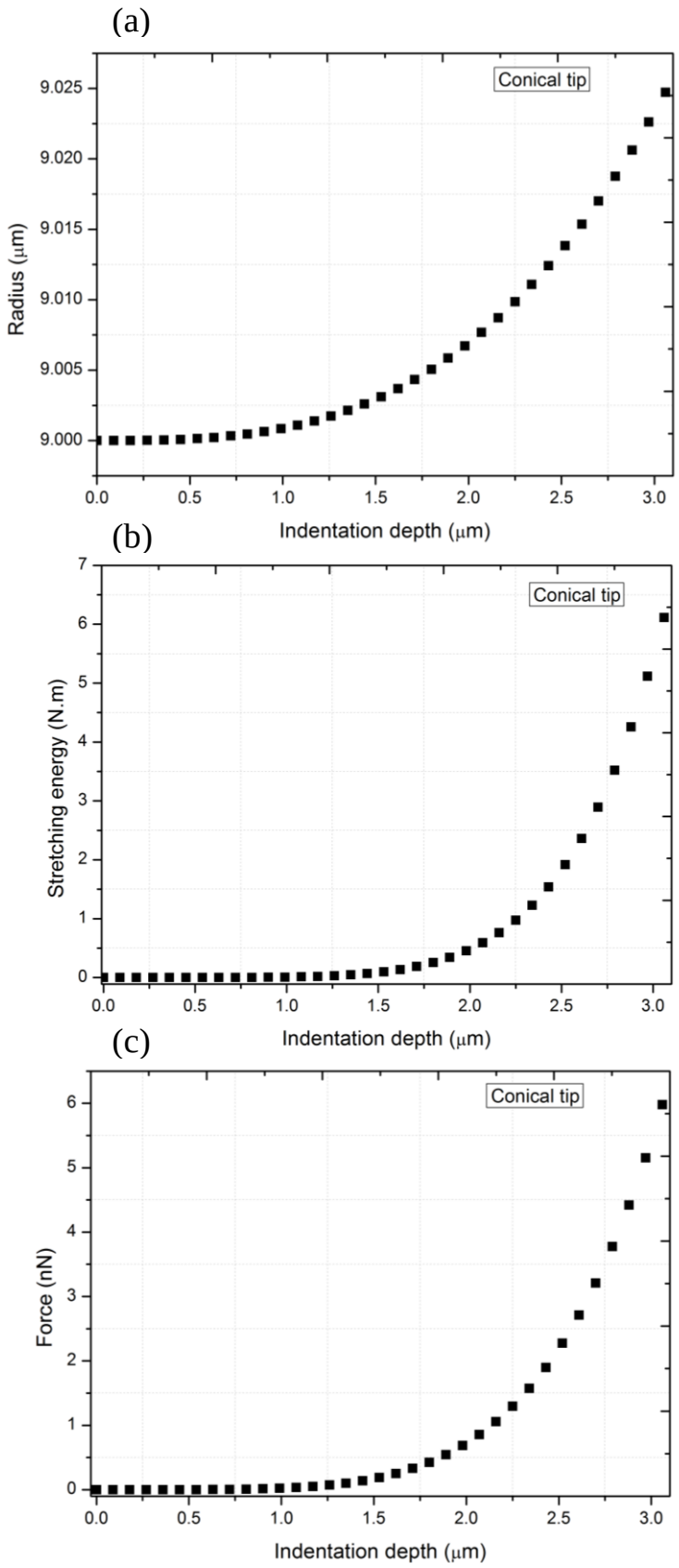

Figure 3-7. Changes in the (a) radius (b) stretching energy and (c) force of a cell as a function of indentation depth for the conical indenter.

As it can be seen from Fig. 3-7 (a), the relation between the new radius [R] and indentation depth is non-linear. At the maximum indentation depth (3 μm), change in the radius of the cell is obtained as 0.025 μm. Comparing this value with the one obtained from the flat indenter at the same indentation depth (0.46 μm), shows that how the shape of the indenter can effect on the radius/size change of the cell. Also, based on the shape of the conical indenter it can be expected that changes be small and more local than the flat indenter. Moreover, Figs. 3-4 (b and c) show the stretching energy and force have non-linear relations with the indentation depth. Comparing the stretching energy and force curves obtained from the conical tip with the ones from flat indenter shows that in the same range of indentation depth, changes in the stretching energy and force curves from the conical indenter are sharper and curves are steeper. Furthermore, in the case of the conical tip it can be seen that finding the first contact point is more difficult than the flat indenter.

In the last step, a set of experiments were prepared to test Eq. (3-100) to calculate the Young's elastic modulus numerically. Also, Eq. (3-96) was applied to calculate size changes of the cells after deformation. To measure the mechanical properties of spherical cells, murine J774 macrophage cells were selected. The force mapping mode of AFM with a map size of 8×8 indexes and a conical tip were used for all the measurements. Macrophages are a type of the white blood, tissue-dwelling cells, which are produced from differentiation of monocytes. Due to their immune function and pathogen engulfment, macrophages are highly robust cells in the immune system. Also, ease of maintenance and high reproducibility of macrophages make them suitable model cells for quantitative biophysical research [76]. Moreover, J774 macrophages are an "adherent" cell line with spherical shape, which make them completely suitable for biophysical studies [77].

Since the main aim of developing the new model is calculating Young's elastic modulus, Eq. (3-100) is used to fit to the force-tip position curves obtained from measuring J774 cells with AFM. Prior to calculations, new radii are calculated using Eq. (3-96). For all calculations values for the half cone angel, R_i and Poisson's ratio were equal to 20°, 0.008 μm and 0.5 respectively. Thickness of the cell membrane [T] is assumed to be 10 nm in all calculations [78]. The following steps were performed to fit the Eq. (3-100) to the force-tip position curves:

1- An initial value for the term $4\pi TE/1+\nu$ is assumed (e.g. 1000 nN/μm);

2- The rest of the remained terms in the equation are calculated for different [D] and [R];
3- Using step (1) and (2) values for force are derived based on the changes in the indentation depth and obtained new radius;
4- The offset of each curve is recorded and added to the obtained values of force;
5- For each curve the contact point is found and subtracted from the indentation depths, used in calculations, in order to find the position of the tip;
6- Results from step (5) are plotted versus the results from step (4) to get the fitting curve along with the force-tip position curve in one graph;
7- By changing the guessed value for the term $4\pi TE/1+\nu$, the best fit for the force-tip position curve is obtained;
8- Using the value of the term $4\pi TE/1+\nu$ for the best fit, Young's elastic modulus is calculated.

To test fitting of the force-tip position curves, obtained from AFM measurements, with the developed new model and compare them with the Hertz-Sneddon model, three J774 mouse macrophage cells with low, medium and high elasticity are selected. The results of fitting force-tip position curves with the new developed model along with the Hertz-Sneddon model are presented in Fig. 3-8 and Fig. 3-9. Fitting force-tip position curves with the developed model shows the model can use to fit to stiff, medium stiff and soft cell samples (Fig. 3-8 (a, b and c)). However, it can be seen that as the cells become softer, the force-tip position curves fitted better with the developed model. Comparing the developed model with the Hertz-Sneddon model shows that in contrast the Hertz model can fit to the stiffer cell better that the soft cell. However, both models cannot fit the entire force-tip position curves perfectly (Figs. 3-8 and 3-9). Moreover, the Young's elastic modulus of the three J774 mouse macrophage cells are calculated using the developed new model and the Hertz-Sneddon model. For the stiff cell with the initial radius of 8.8 μm, the Young's elastic modulus is obtained as 95.2 MPa and 2.34 kPa from the developed model and the Hertz-Sneddon model respectively. For the medium stiff cell with the initial radius of 9.05 μm, calculated Young's elastic modulus from developed model and the Hertz-Sneddon model are 65.45 MPa and 1.62 kPa respectively. Also, for the soft cell with the initial radius of 6.9 μm, derived Young's elastic modulus are 1.19 MPa and 0.57 kPa for the developed model and the Hertz-Sneddon model respectively.

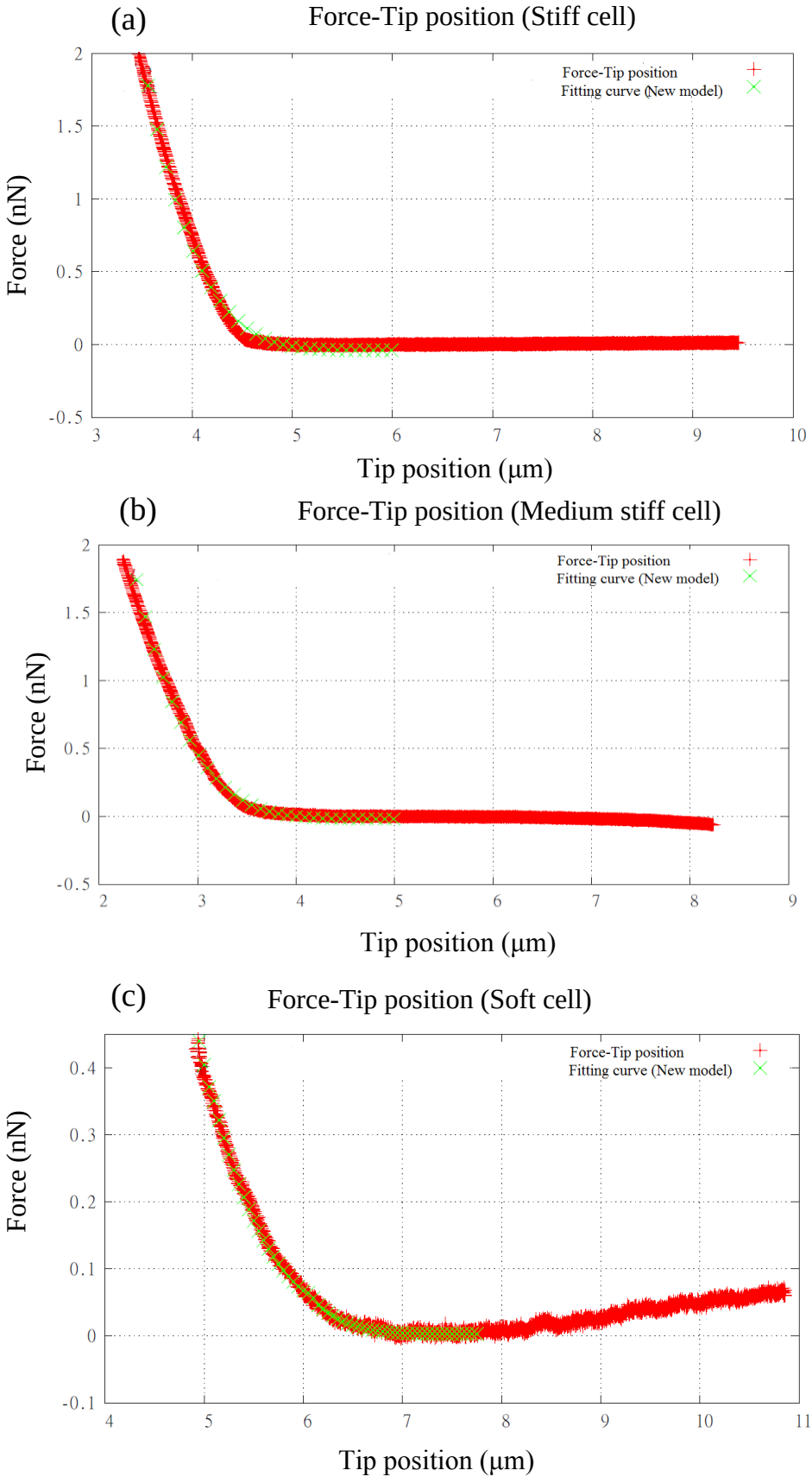

Figure 3-8. Developed new model is fitted to (a) stiff (b) medium stiff and (c) soft cell samples in order to find the Young's elastic modulus.

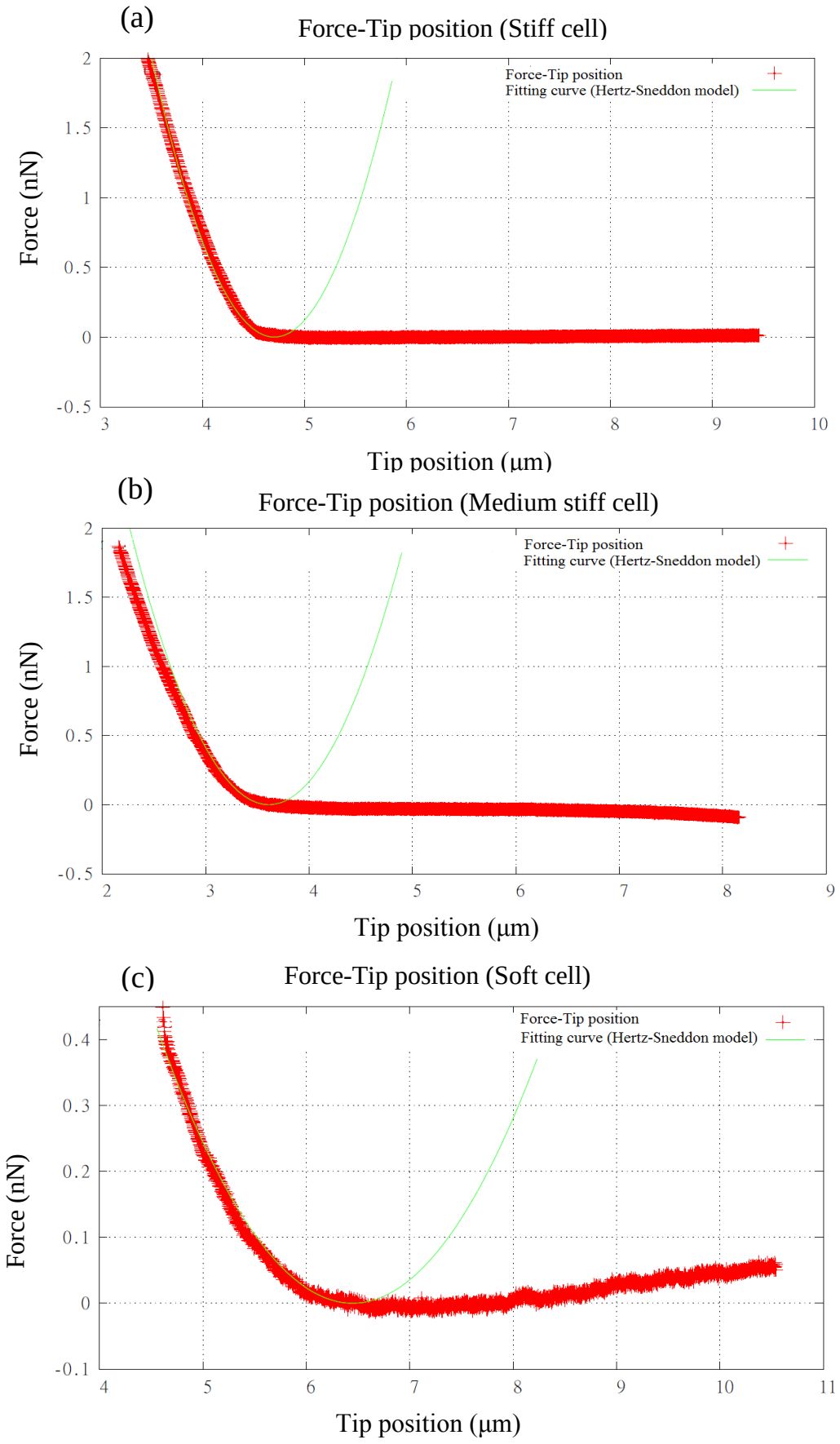

Figure 3-9. The Hertz-Sneddon model is fitted to (a) stiff (b) medium stiff and (c) soft cell samples in order to find the Young's elastic modulus.

Referring to the Young's elastic modulus obtained from the developed model and the Hertz-Sneddon model, it is clear that the results are significantly different. This difference can be expected due to the nature of the two models. Since the new model is developed based on the elastic shell theory, different assumptions from the Hertz model are used. For example, in the elastic shell theory cells assumed as a bag, which is filled with liquid and the changes in the stretching energy of the cells due to the applied external force are measured for the surface elements. Therefore, obtained Young's elastic modulus from the developed model is considering the surface of the cells (lipid bilayers). However, the Hertz model describes the elastic deformation for two perfectly homogeneous bodies with infinite thickness under load. To calculate the Young's elastic modulus, the Hertz model describes the relationship between the applied force and the central displacement for isotropic or transversely isotropic linear elastic bodies [79]. Therefore, while the new model tests the changes on the surface of the cell the Hertz model focuses on the changes inside of the cell. This can be also understood from the graphs presented in Figs. 3-8 and 3-9. As a cell become softer it is probable that the most changes happen inside of the cell rather than on the surface of it. So, the stiff cell acts more like a "bulky body" rather than the "bag of liquid" and the Hertz model can fit to the obtained force-tip position curve better. However, soft cell can be more the "bag of liquid" rather than the "bulky body" and therefore the developed model can fit to the force-tip position curve better. Furthermore, comparing the derived Young's elastic modulus from the developed model with the elastic properties of the lipid bilayer (28-116 MPa) showed that the results are in the same range as reported in previous researches [75, 80].

Finally, Eq. (3-96) is used to calculate size changes in the cells based on the indentation depth. Therefore, changes in the size of the J774 cells after deformation were calculated using Eq. (3-96). For fifty J774 cells, the maximum indentation depth of 3 μm (where the applied force reached 2nN) was used in the calculations. The half cone angel and R_i were also had values equal to 20° and 0.008 μm respectively. To calculate the initial radius of each cell, the diameter of the cells was measured from two different sides prior to the indentation. For this purpose, an optical image of each cell was taken and diameters were measured by using the "measure the distance" function in the AFM imaging tool bar (Fig. 3-10). Finally, the radius was obtained using Eq. (3-101).

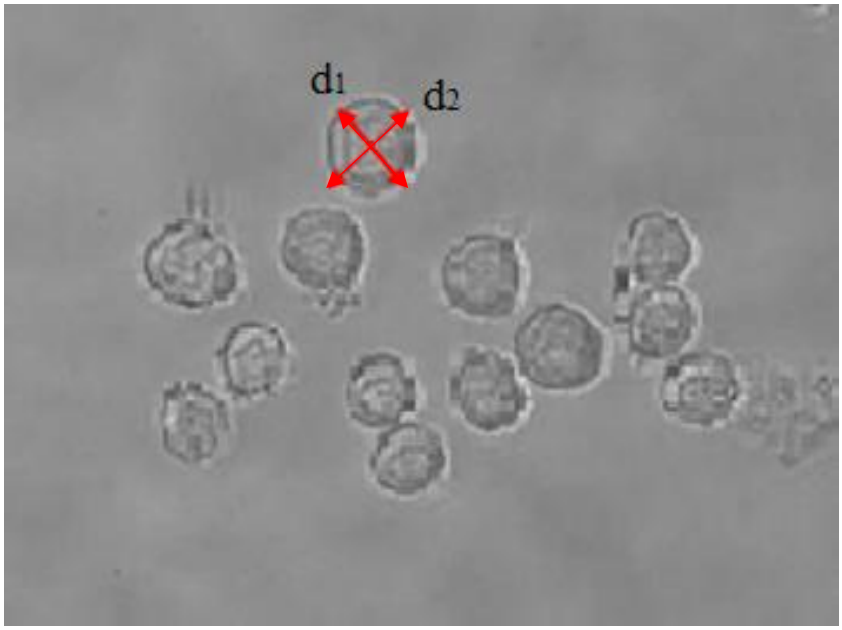

Figure 3-10. An optical image of J774 mouse macrophage cell line. Spherical shape of the cells can be seen from the image. The double sided red arrows show how the diameters were measured.

$$R_0 = \frac{1}{2}\frac{(d_1 + d_2)}{2} \tag{3-101}$$

The measured initial radius of the cells [R_0] and calculated new radius after indentation [R] are presented in Table 3-1. Obtained results shows that changes in the size of the cells after deformation are small and they are mainly in the ranges of 0.01 μm. Since, the force applied locally (due to the shape of the conical tip) and kept low (maximum of 2 nN), it can be expected that small changes (in the magnitude of 10^{-2} μm) happen in the size of the cells.

Table 3-1. Initial radius [R_0] of fifty J774 cells and changes in their radius after deformation [R] along with their difference.

Cell number	R_0 (µm)	R (µm)	$R-R_0$ (µm)
1	7.15	7.16	0.01
2	6.675	6.68	0.01
3	8.675	8.68	0.007
4	5.35	5.36	0.01
5	6.325	6.34	0.014
6	7.45	7.46	0.01
7	6.54	6.55	0.01
8	7.35	7.36	0.01
9	8.3	8.308	0.008
10	7.325	7.33	0.01
11	9.825	9.83	0.005
12	9.05	9.056	0.006
13	8.825	8.83	0.007
14	8.825	8.83	0.007
15	7.575	7.58	0.009
16	7.375	7.38	0.01
17	8.075	8.08	0.008
18	7.925	7.93	0.008
19	7.575	7.58	0.009
20	7.85	7.86	0.01
21	8.1	8.11	0.01
22	8.2	8.21	0.01
23	7.35	7.36	0.01
24	8.375	8.38	0.005
25	7.425	7.43	0.01
26	6.9	6.91	0.01
27	5.525	5.54	0.015
28	8.6	8.61	0.01
29	8.15	8.16	0.01
30	6	6.01	0.01
31	7.75	7.76	0.01
32	6.025	6.04	0.015
33	7.725	7.73	0.009
34	7	7.01	0.01
35	8.525	8.53	0.007
36	7.125	7.14	0.015
37	8.2	8.21	0.01
38	6.85	6.86	0.01
39	6.575	6.58	0.005
40	7.8	7.81	0.01
41	6.475	6.48	0.01
42	6.475	6.48	0.01
43	8.55	8.56	0.01
44	8.3	8.31	0.01
45	8.275	8.28	0.008
46	8.475	8.48	0.007
47	8	8.01	0.01
48	8.025	8.03	0.008
49	8.4	8.41	0.01
50	9.65	9.66	0.01

3.8 Concluding remarks

This Chapter aimed to study and develop a model based on the elastic shell theory to quantify the mechanical properties of biological samples. All the equations derived for calculating the changes in the radius of the cells after deformation (Eq. 3-85 and Eq. 3-96) and equations to calculate the Young's elastic modulus as a function of applied force and indentation depth (Eq. 3-89 and Eq. 3-100) are novel.

The following key conclusions are listed below:

- Changes in size of the cells after deformation were predicted using the developed model. The derived results were in the acceptable ranges (shown in Table 3-1);

- The relation between the indentation depth and derived radius for both flat and conical indenters obtained non-linearly;

- The changes in the stretching energy of the cell due to the changes in the indentation depth, in the case of flat and conical indenters, found to be non-linear;

- The changes in the indentation depth for different ranges of applied force using flat and conical tips showed a non-linear relation between force and indentation depth;

- The numerically obtained Young's elastic modulus from the developed model was in the range of Mega Pascal. It was explained that due to the assumptions made for the model, the obtained results show the elastic properties of the cells lipid bilayer (surface of the cell).

As it was discussed, the developed model showed promising results for measuring the size changes and Young's elastic modulus of the surface elements of the biological samples. However, as it was shown, using the developed model fitting cannot be done accurately and it improves as the cells become softer. Yet, it can be said that, however, the attempt to develop a model to quantify the elastic properties of biological samples based on the elastic shell theory provided convincing results, due to the complex environment of the biological samples, has its certain limitations. Therefore, for the rest of this thesis where analysing the force-indentation curves are required for measuring the Young's elastic modulus of the cells, the Hertz-Sneddon model is applied. Although the

Hertz-Sneddon model comes with its own set of limitations, which detailed in Chapter 1 section 1.3.1, the advantage of this model is that the limitations are well understood and so we are in a position to combat the affect they have on the data. Through an understanding of the model we have been able to change aspects of the experimental method, such as indentation depth, to produce curves that fit the model well and produce reliable results.

CHAPTER 4

Investigation of the mechanical properties of umbilical cord blood CD34+ stem cells during their differentiation and maturation process for sorting and separating purposes

Contents

4.1 Introduction

The annual requirement of red blood cells (RBCs) is as high as 90 million units, worldwide. In March 2016, the global stem cell therapy market was estimated to grow by 25% between 2015 and 2022 reaching a market value of $297 billion by 2022. Due to a rise in the number of people diagnosed with Acquired Immune Deficiency Syndrome (AIDS), as well as many other blood borne diseases/disorders, there is a significant decrease in the number of blood donors and traditional transfusion products. As a result, only 4% of the human population that are eligible currently donate blood, with blood supply and stocks varying seasonally. Furthermore, blood that is donated can only be stored for use for a maximal period of 35 days, due to the variable mixed age of the donated cell population i.e. RBCs have a finite life span, and not all RBCs within the

blood stream mature at the exact same rate. In the UK number the units of blood used is around 2.2 million per year, with 1 unit of blood equally around 1 pint of donated blood. Also, the estimated market value of manufactured blood in UK is £300 million/year, and the worldwide market estimated to be at least £11 billion [64, 81]. As a result of the aforementioned issues surrounding donor RBC blood supply, there is an increased need to meet the shortages using *in vitro* cell culture methods to produce RBCs. The current cell culture techniques used to produce RBCs *in vitro* use donor hematopoietic stem cells derived from umbilical cord blood. There is a great potential for any *in vitro* produced RBCs to cover the current requirements (shortages) for donor RBCs experienced in the medical field, as well as minimize the risk of infections [82-84]. In October 2011, a ruling by the European Court of Justice, resulted in the passing of a law whereby cells derived from human Embryonic Stem Cells (hESCs) cannot be patented. Therefore, IP rights supporting any commercialisation of regenerative medicine therapies involving hESCs will results from the processes through which hESC cells are cultured and separated (which is still open for patenting). Therefore, cell purification techniques developed for regenerative medicine purposes could form the backbone for the creation of hESC derived therapies [85].

Manufacturing cell-based products such as RBCs requires the presence of rapidly sorting and separating strategies to ensure that all cell-based products are highly purified and contamination free. Therefore, selecting high efficiency separation methods for sorting and separating cell-based products is crucial. The selection of an appropriate separation method for the manufactured cells depends on the production process i.e. sample preparation, handling, manufacturing process and Good Manufacturing Practice (GMP) compatibility, as well as the final product i.e. cell composition, purity and viability. To choose a suitable separation method, numerous different aspects of the sample are taken in to consideration. Therefore, to determine the required level of purity, which leads to the selection of an effective separation method, a thorough analysis to gather information about the starting materials and expected final products must be carried out.

Cell separation techniques can be divided into two main groups (1) labelled and (2) non-labelled sorting methods. The two main labelled methods are flow cytometric Fluorescent-Activated Cell Sorting (FACS) and Magnetic-Activated Cell Sorting (MACS). It should be noted that, although labelled based techniques show a high yield for cell purification (>95%), there are some disadvantages associated with these methods. For example, labelling the cells requires extra processes which leads to higher

consumables costs. Additionally, added labelling processes can increase the risk/occurrence of sample contamination via the labelling reagents and labelling processing. The separation process is elongated more with the whereby at the end of the separation process the target cells will have the attached label to them. Towards the end of the cell sorting process the removal of the labels also adds more steps to the manufacturing process, with the risk of any attached labels interfering with the signalling pathways and thus effecting the physiological state of cells. Moreover, if the label removal process cannot be done completely it will be dangerous for the downstream applications especially when the final products are injected into humans.

As a result of the disadvantages encountered with label based cell sorting methods, more recent label free techniques have now become more adventitious for cell sorting of cell based products. Label free methods mainly utilise the biomechanical properties of cells such as size and elasticity/deformability to sort populations of cells. Furthermore, they do not present with many of the previously discussed disadvantages associated with cell labelling sorting methods. There is currently a variety of label free techniques used for cell separation, some of which recently becoming potentially suitable for large-scale clinical cell production [63].

There are variety of techniques for cell separation, where among all of them the ones which are potentially suitable for large-scale clinical cell production and based on the cell size and elasticity are: Acoustophoretic, Deterministic Lateral Displacement (DLD) [86], normal flow filter devices (also known as microfilters), Tangential Flow Filters (TFF) [87] (also called cross-flow filters or microscale membranes) and Inertial Focusing (IF) [88]. Sorting in this type of systems is facilitated purely by cell endogenous properties such as size and deformability. Deformability is emerging as a novel homogeneity marker that could serve to identify subpopulations within complex cell samples such as mRBCs [89]. The different approaches proposed in the literature based on mechanical properties as sorting factors present many advantages such as a reduced number of sample processing steps (e.g. by reducing staining/washing steps), relatively high-throughput (millilitres / min [90] and litres / min [91]) and efficiency (~90%) [92].

From the techniques mentioned above the Inertial Focusing (IF) method is one of the good microfluidic systems, which works based on the physical properties (size and elasticity) of the cells [65]. Inertial focusing is a phenomenon in which within the laminar flow the suspended particles can move across the straight or circular cross section microchannel to be sorted based on their size and deformability. The IF method is able to

continuously focus and sort the suspended particles/cells without using external forces. In the fluids with low Reynolds number this phenomenon occurs due to the balance of two forces, which are the shear induced lift force and inertial lift force. The shear induced lift force is a result of the curvature form of the velocity profile and it is directed towards the wall of the channels. The lift inertial force is a result of the interaction between the wall and the particle/cell and its direction is against the channel's wall. In the spiral microchannel due to the curvature shape of it the lateral motion of particles/cells are enhanced across the channel by applying the dean drag force on them. Since this method is a passive technique with deformability-induced migration and the ability for the extremely high throughput, for flowing of mixed particles/cells in size and elasticity, it is a suitable method for sorting and manipulating the cells [93]. In addition, studies showed that the inertia of the fluid results in nonlinearity in migration of particles/cells and for the deformable particles/cells this nonlinearity can also occur in the lateral migration too. Also, deformable particles/cells experience more lift force which can be used for higher throughput for sorting and separation of the particles/cells [94, 95]. Deformation-induced lift forces will act in superposition with inertial lift forces to create modified lateral equilibrium positions that are dependent on particle deformability. Consequently, the lateral equilibrium position can then be used as the measure of particle deformability when the particle size is taken into account. Furthermore, the differences in lateral equilibrium position among cell types can be utilized for deformability-induced target cell enrichment by directing entrained target cells to separate designated outlets [65].

Moreover, in one study it has been demonstrated that for a mixed cell culture media, a mixture of four cells, MDA MB 231, HL60, MCF 7 and HeLa, with Young's elastic modulus of 1 kPa, 2.7kPa, 3.4 kPa and 13.5 kPa could be sorted using the stiffness-based sorting microfluidic channel with an efficiency ranging from 70 to 85% [96].

Since applying the IF method and many other separation techniques for cell classification and separation are based on the elasticity and size of the cells, understanding the mechanical and physical changes of the RBCs during the differentiation process is essential.

In this Chapter, we have studied the mechanical properties (elasticity, size and shape) of umbilical cord blood CD34+ stem cells as they underwent cell differentiation. Testing the cells during their progressive maturation provided us reliable information about the morphological and mechanical changes that occur within the cells during differentiation, which can be later used for quality control, separation and diagnostic purposes.

4.2 Generation and differentiation of Erythroid cells from human stem cells

Erythropoiesis of mammalian cells comprises a number of different steps including expansion, differentiation, enucleation and maturation. Many morphological changes along with the molecular and cellular mechanisms are involved in this process, however they are not fully understood yet [67]. RBCs can be produced *in vitro*, using hESCs, umbilical cord blood CD34+ cells, adult hematopoietic stem/progenitor cells and human-induced pluripotent stem cells (hiPS cells) [97]. Currently, a number of different methodologies have been applied using hematopoietic stem cells and progenitor cells to produce the RBCs in an *in vitro* environment. Among the various methods, the multi-phase liquid culture media system is a common method currently used to produce RBCs in the lab [82]. In this section the *in vitro* production, differentiation and maturation of RBCs from umbilical cord blood CD34+ cells and morphological changes of the cells is explained.

4.2.1 Production of RBCs from human stem cells

The process of cell expansion, differentiation and maturation for hESCs takes around thirty days. The whole process can be divided in to four steps. The first step is mesoderm formation from the hESCs. This normally takes three days (days -3 to 0). After the formation of embryoid bodies, the second step is hemangioblast expansion. This generally takes around ten days (days 0-10), and is required for complete expansion and hematopoietic proliferation of the cells. In the third step, which takes ten days (days 11-21), the haematopoietic progenitors are further expanded and then differentiated into erythroid cells. The fourth and last step in the cell culture process is maturation of the erythroid cells, which takes another ten days (days 21-30) [67, 84].

Following the fourth step, RBCs can be harvested for experimentation/further manipulations. In summary, the differentiation process involves the initial step of lineage commitment followed by further steps of differentiation and expansion. Finally, the cells mature into reticulocytes, which are the final products in the *in vitro* production process. Since the cells were produced *in vitro,* there was considerable variations in reproducing the first two steps (up to day 10 of the pluripotent process), which may be due to missing some of the signals required during the initial phase of the differentiation process. Day 11 of the cell culture process is the start day of the umbilical cord blood CD34+ cells (Fig. 4-1). Therefore, we used cord CD34+ stem cells as these were more consistent in both

expansion of cell number and differentiation and showed suitable reproducibility of the process. Therefore, cells grown for experiments here were derived from CD34+ progenitor cells as they were differentiating. For this project samples were selected from the cells of days 11, 14, 18 and 21 of the cord process to test their mechanical properties, we labelled them based on their days of differentiation. Also, since the reticulocytes are the final products in our RBCs production process, cells need to be separated from the mixed culture media at this stage. Additionally, in-process control is required during the expansion and differentiation steps to separate the unwanted cells from the cell culture and monitor the ongoing differentiation efficiency/cell health.

Referring to Fig. 4-1, it is evident that during the cell differentiation process, the shape and size of the cells are changing continually. While most of the cells from day 11 of the cord process are generally spherical in shape, with a relatively large nucleus, at around day 14, the cells start to become smaller with uneven outlines and a condensed nucleus (see section 4.4). Additionally, the enucleation process normally starts around day 14 of the cord process, whereby the condensed nucleus of the cell is extruded to the outside of the cell (see Chapter 5, section 5.1 for more details). However, in some cases, some of the expelled nuclei still remain attached to the cells. At around day 18 of the cord process, the majority of the cells have become enucleated and are immature reticulocytes. Following this developmental process, at around day 21 of the cord process, mature reticulocytes, which are the immature RBCs without a nucleus and reticular network of ribosomal RNA, begin to appear. Reticulocytes are the final products in the *in vitro* production of RBCs. However, cells then only mature into erythrocytes with the oval biconcave disk shape within the blood circulation (*in vivo*) [98].

In this Chapter and the following Chapter cells from the day 11, 14, 18 and 21 of the cord process are mentioned only as day 11, 14, 18 and 21.

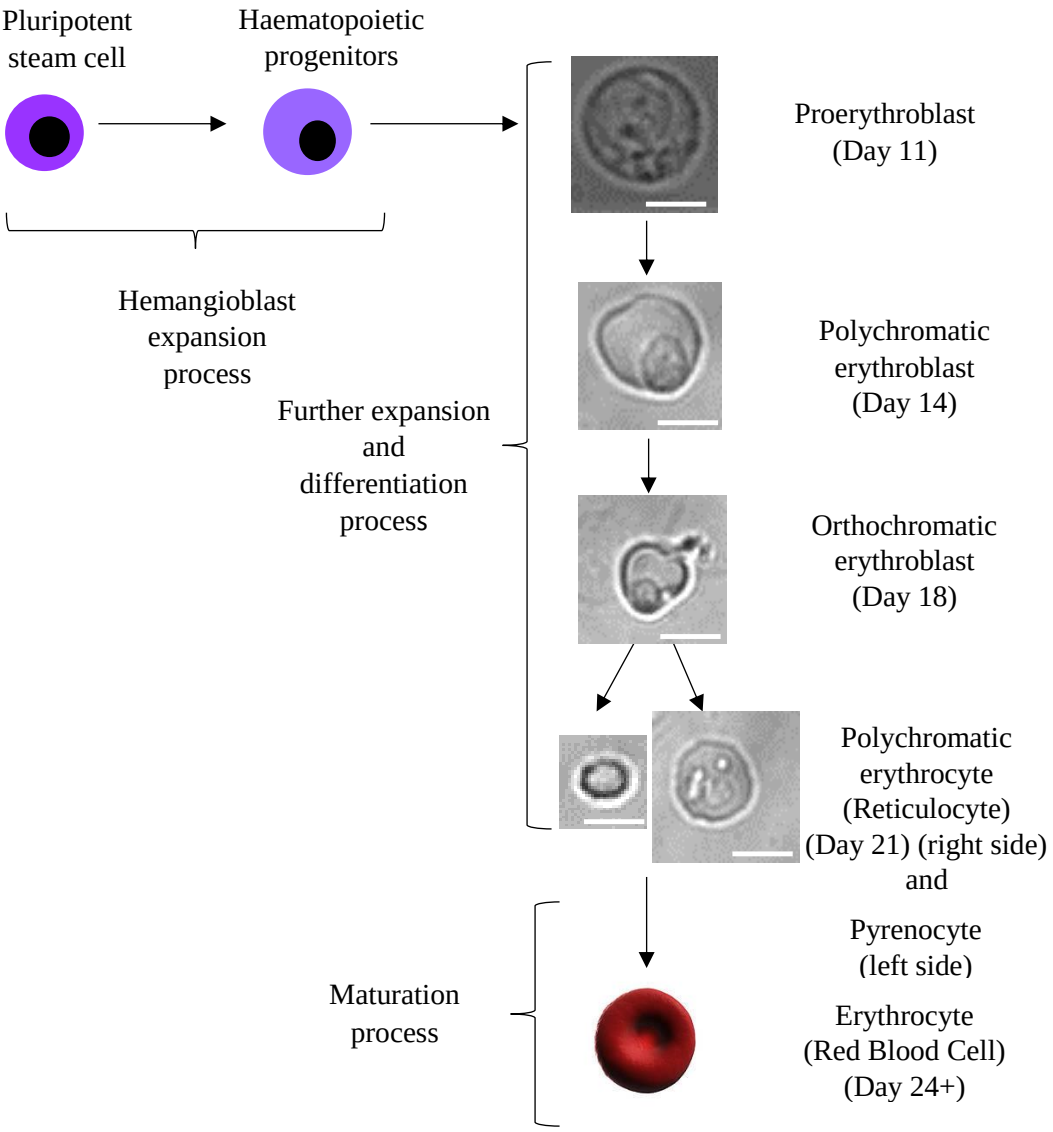

Figure 4-1. Differentiation and maturation of umbilical cord blood CD34+ cells to the Erythroid cells *in vitro*. Morphological changes and enucleation of the cells can be seen during the progression from day 11 to the day 21. In day 11 the big portion of the cell is occupied by the nucleus and as the cell become smaller in size from day 14 the nucleus shrinks as well. Here in day 18 the cell is ejecting the pyrenocyte and by day 21 cell with the reticulated appearance is remained. All images were taken using optical imaging of the AFM. Scale bars in the images represent 5 μm.

4.3 Investigation of the Young's elastic modulus of umbilical cord blood CD34+ stem cells during the differentiation and enucleation

Several changes occur in the cord CD34+ cells during their differentiation process. These changes include a gradual decrease in the number of the organelles until they disappear. Furthermore, the cells' nucleus becomes more dense during pyknosis, until it is finally extruded from the cell [82]. Since, matured RBCs are required to pass through

microvascular constrictions (some of them up to three times smaller in diameter compared to the RBCs size) and veins to transfer the oxygen, it is important for RBCs to be able to transverse through the capillaries without undergoing haemolysis [97, 99]. RBCs are known to be one of the most deformable cells in the human body, and as a result it is expected that the cells become more elastic during the differentiation and enucleation processes [100]. The elastic properties of cord CD34+ cells can be characterized by applying an external force using AFM and measuring the cells deformability from the derived force-displacement curves.

Producing reticulocytes *in vitro* requires cell sorting/purification and separating during the production process as well as upon completion of the production process. In the case of reticulocytes production, as they may later be used for as donor injected cells, it is vital to operate the sorting and separating processes with high accuracy and precisions in order to separate the unwanted cells in each step of differentiation. Furthermore, in the last step of manufactured cell production, when the final product is ready for harvesting (around day 21 when the reticulocytes are formed), a proper separation technique is required to sort the cells. The separation process is necessary to separate the enucleated cells in the mixed culture media from the nucleated cells (if any remain in the culture mix) as well as any extruded pyrenocytes. As is discussed in section 4.1, selecting the correct separation techniques, which have less drawbacks and higher cell/particle yields, is important. Therefore, selecting a cell/particle separation method that sorts the cells based on their physical and mechanical properties (size and elastic modulus), can be highly beneficial for the cell separation process. Studying the mechanical properties of cord CD34+ stem cells during differentiation is not only useful for the analysing the "in-process" control and final separation of the cell separation techniques, it can also be beneficial for further scientific studies such as diagnostics research [65, 101].

In the following section, changes in the elastic properties of cord CD34+ stem cells during cell differentiation were tested and analysed. Samples from days 11, 14, 18 and 21 (during the differentiation process) were selected and sixty cells per day of differentiation were indented using the AFM QI mode. All derived force-displacement curves were analysed by applying the Hertz-Sneddon contact model.

4.3.1 Elasticity changes of the cord CD34+ stem cells during the differentiation

Using QI mode on the AFM with map sizes of 8×8 indexes, the local elastic properties of the cord CD34+ stem cells during the differentiation process were quantitatively determined from the obtained force versus displacement curves. For each measurement, 64 force curves were recorded. However, not all of the 64 curves comprised measurements taken directly from the cells, some of the curves were from the AFM dish coating and/or residues within the culture media. Such curves were discarded from the analysis/calculations. The Young's elastic modulus for each force-displacement curve was calculated using the Hertz-Sneddon model. All derived results for each cell were collected, with all the results from all of the cells for each day of differentiation, sorted into the different ranges of elastic moduli. To study the changes of the elastic modulus of the cord CD34+ stem cells during the differentiation process, each range of the elastic modulus was plotted against the probability of each elastic modulus.

The analysed results from days 11 and 14 are presented in Fig. 4-2. Referring to the plots, it can be seen that there are three ranges of elastic moduli with higher distributions for day 11. These three ranges/peaks are in the range of 0.5-0.6 kPa, 0.6-0.7 kPa and 1.2-1.4 kPa respectively. For day 14, the higher elastic distributions are 0.5-0.6 kPa, 0.6-0.7 kPa and 0.41-0.5 kPa respectively. Comparing day 11 with day 14, it is evident that although for both days the higher peaks are in the ranges of 0.5-0.6 kPa and 0.6-0.7 kPa, the probability ranges for day 14 are higher than day 11. Furthermore, the third higher peak for day 11 is 1.2- 1.4 kPa, but for day 14 the third peak is shifted to the softer range (0.41-0.5 kPa). This cell softening from day 11 to day 14 can be related to the fact that while the majority of the cells are nucleated at day 11, the enucleation process starts from day 14. Therefore, samples from day 14 are a mixture of nucleated and enucleated cells (more details on the effects of the cell's nucleus on elasticity described in Chapter 5, section 5.5). As the cord CD34+ stem cells differentiation progressed further, additional changes could be observed in all the ranges of the elastic modulus distributions. It can be seen from Fig. 4-3, that at days 18 and 21, the elastic modulus shifted to the softer ranges, with most of the distributions in the ranges of 0.41-0.5 kPa, 0.51-0.6 kPa and 0.3-0.4 kPa respectively. Although, for both days the peaks in elasticity were the same, but from days 18 to day 21, the softer elastic range increased as shown by the increased probabilities. Furthermore, it should be noted that the cell enucleation process starts from day 14, and

by day 18, most of the cells are expected to be enucleated, with all cells completely enucleated at day 21 (however, there is always a slight percentage chance that some cells still have a nucleus). Therefore, the results from both days' present higher probabilities in the softer ranges of elastic modulus, and a significant decrease in the locations on the cells with the higher elastic modulus.

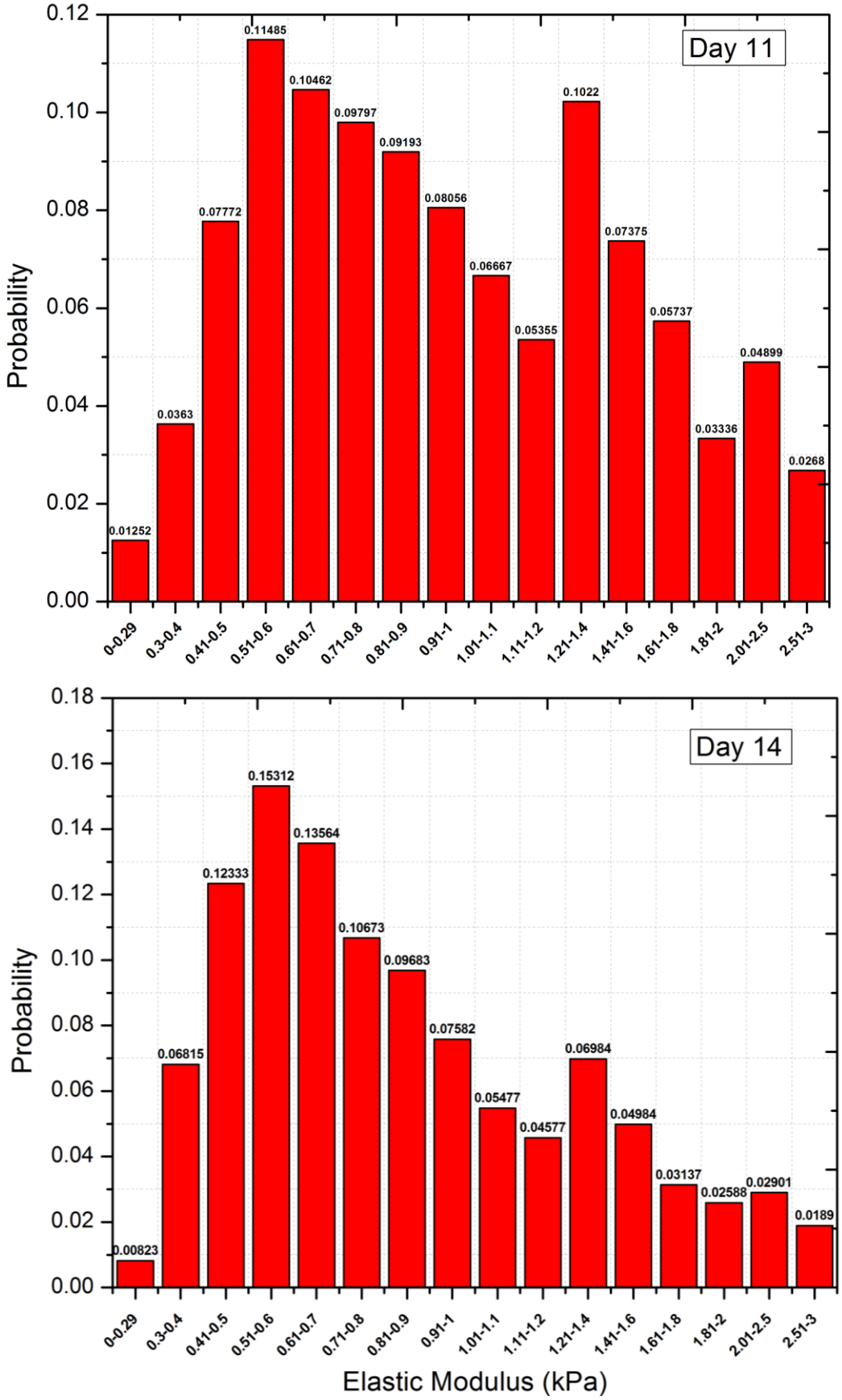

Figure 4-2. Probability distributions of the Young's elastic modulus for the cells of day 11 and day 14.

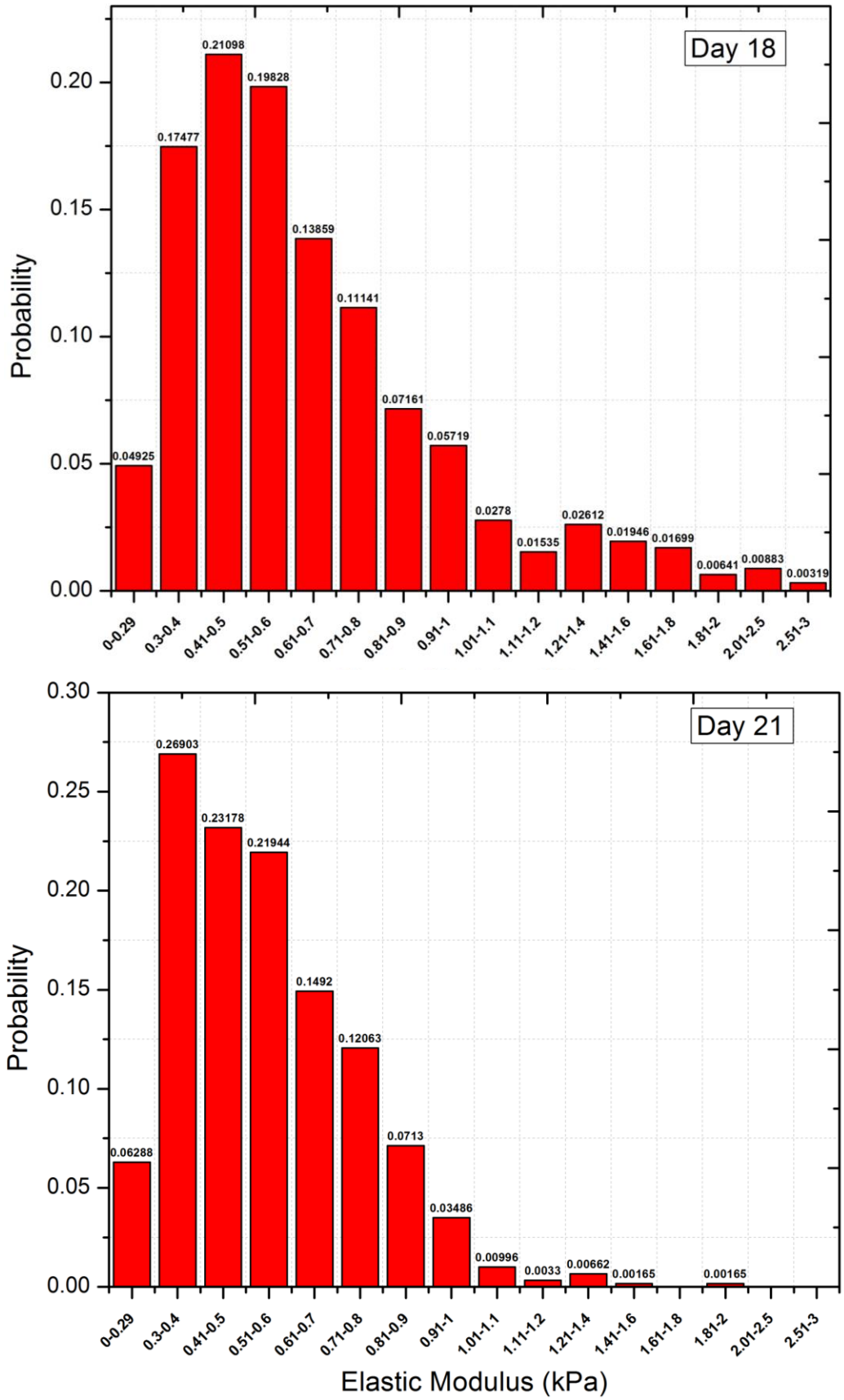

Figure 4-3. Probability distributions of the Young's elastic modulus for the cells of day 18 and day 21.

In the next step in attempting to understand if the elastic distribution obtained from all sixty cells measured for each day can be related to each single cell's elastic distribution,

the elasticity distribution of each cell was plotted and compared with the plots from the all cells. In Fig. 4-4, the results for single cells on days 11, 14, 18 and 21 were presented (all 60 samples per day). Comparing Fig. 4-4 with the Fig. 4-2 and Fig. 4-3, it can be seen that the results for single cells from each day have the same peaks as the plots from all the cells of each day. Therefore, the results from single cells show that they were following the same trend as the results driven from all the cells.

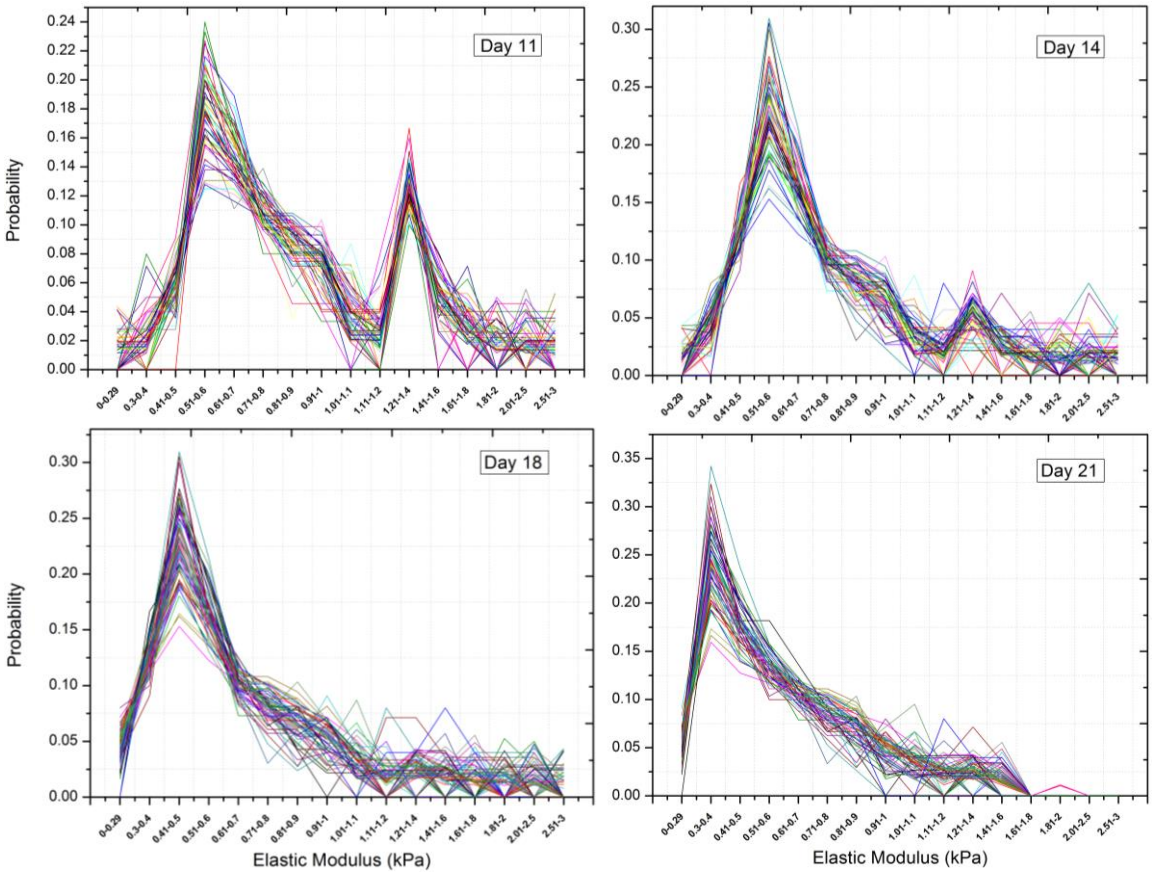

Figure 4-4. Probability distributions of the Young's elastic modulus for the single cells on days11, 14, 18 and 21.

By plotting the obtained data from different days in one graph (Fig. 4-5), it can be observed how the cell differentiation process progresses with the peaks of the stiffer elasticity ranges (day 14) becoming smoother, until they completely vanish by the end of the differentiation process (day 21), and the peaks for the softer elasticity ranges become greater.

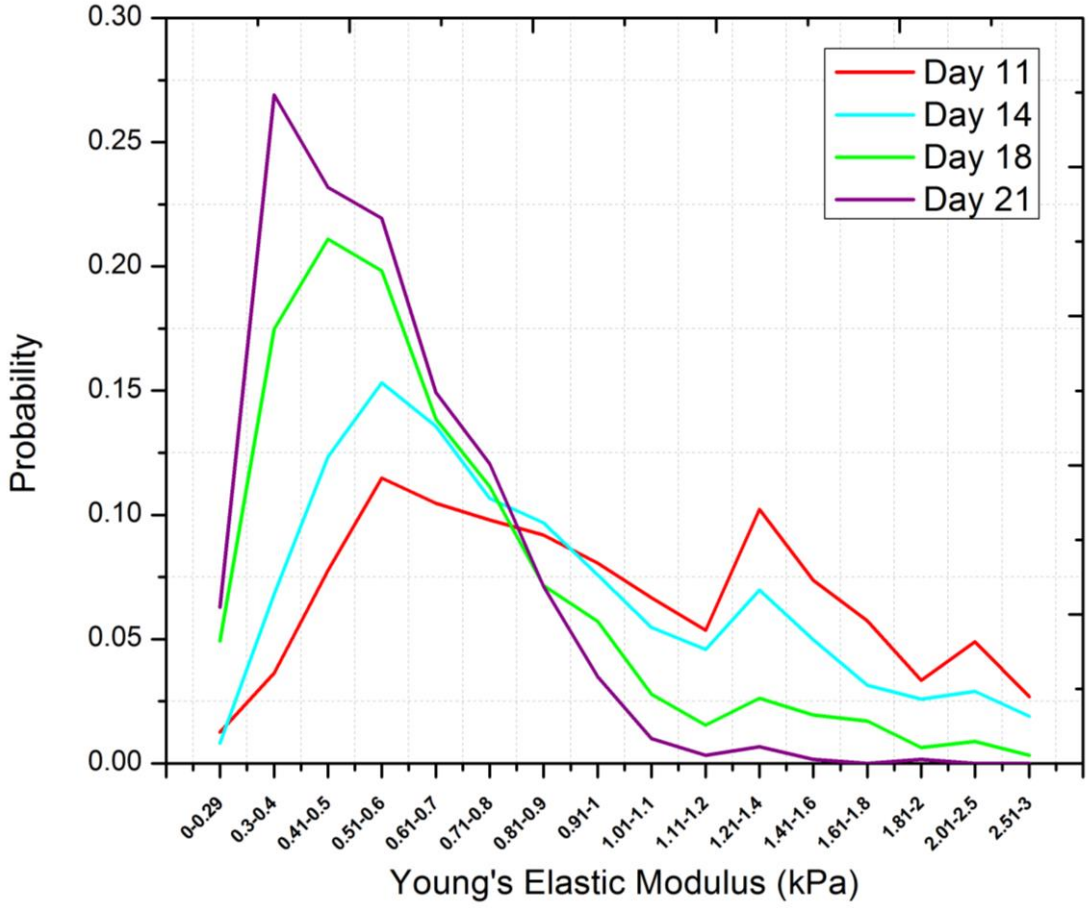

Figure 4-5. Comparing the probability distribution of the elastic modulus derived from cells as they were differentiating.

It has been suggested that the peaks observed in the stiffer elastic modulus ranges for the day 11 and day 14 could result from the presence of the nuclear regions of the cells [102]. To confirm this hypothesis, the optical images of the cells from day 11 were overlayed with the AFM QI map while set on the height channel. In the next step, the height of each location with the resulting elastic modulus for that location was compared with the other cell locations and elastic moduli in order to understand if the higher parts have the higher stiffness too. In addition, the cells on day 14 were sorted into nucleated and enucleated groups to study the effect of the nucleus on the elastic properties of the cells. The results of this study are presented and discussed fully detailed in Chapter 5, section 5.5.

To calculate the median of the Young's elastic modulus for each differentiation day, the boxplot is plotted. Fig. 4-6 is summarising the Young's elastic modulus of the cells at their differentiation days. Values represent median ± SD (60 samples for each presented day), where each box presents the distribution of data from lower and upper quartile with a line in each box shows the median. The whiskers represent the lowest and highest extreme values. Therefore, the median elastic modulus for the days 11, 14, 18 and 21 were calculated as 0.92 kPa, 0.78 kPa, 0.58 kPa and 0.53 kPa respectively. Also, obtained

results from all days are compared statistically by calculating the P-value. Investigations showed that the measured Young's elastic modulus from each day is significantly different from the other differentiation days (****p < 0.0001).

(a)

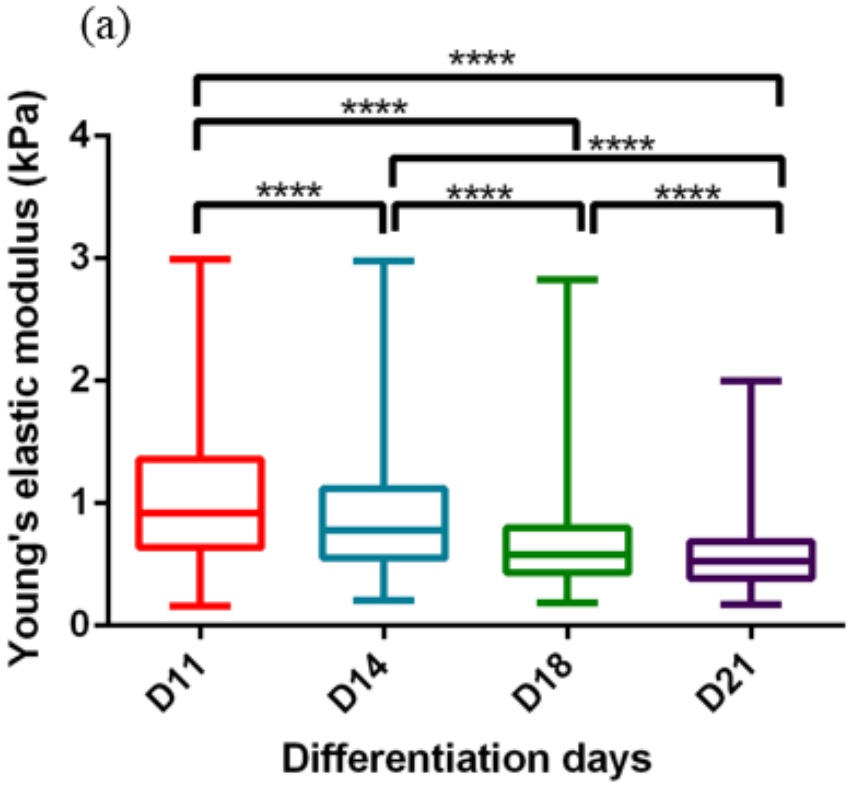

(b)

	D11 (kPa)	D14 (kPa)	D18 (kPa)	D21 (kPa)
Minimum	**0.16**	**0.204**	**0.19**	**0.17**
25% Percentile	**0.64**	**0.55**	**0.43**	**0.39**
Median	**0.92**	**0.78**	**0.58**	**0.53**
75% Percentile	**1.36**	**1.12**	**0.801**	**0.69**
Maximum	**2.99**	**2.98**	**2.83**	**2**
Mean	**1.05**	**0.91**	**0.67**	**0.56**
SD	**0.56**	**0.51**	**0.36**	**0.21**

Figure 4-6. (a) Box and whisker plot to present the Young's elastic modulus of the CD34+ cells during their differentiation process with (b) a table to summarise the derived data from lower and upper quartile with median and standard deviation.

In summary, the derived results from measuring the Young's elastic modulus of RBCs, showed that the differentiation and enucleation process can results in cells becoming softer and/or stiffer at certain specific cellular locations. The calculated mean elastic modulus from each day showed that from day 11 to day 21 there is a 0.5 kPa reduction in the total elasticity of all cells. Furthermore, a day by day comparison of the elasticity changes of the cells showed that while cell stiffness reduction from day 11 to day 14 was 0.14 kPa, this reduction increased to 0.24 kPa from day 14 to day 18. This could be

explained by the fast progression of the enucleation process. For day 18 to day 21, the stiffness reduction calculated was 0.18 kPa. The reason that the stiffness reduction is reduced between these days, could be related to the fact that the enucleation process was completed and the other remaining organelles started to vanish from the inside of the cells [97]. As it is mentioned previously, the cells were again analysed later, to test for the effects of the nucleus on their elastic modulus.

4.4 Study the changes in the size of cord CD34+ stem cells for separation purposes and its relation with the elastic modulus

It is highly probable that cells undergo multiple morphological changes during the differentiation process. Such changes include a reduction in the size of the cells, condensation of the cell nucleus with an increase in the nuclear to cytoplasm ratio, as well as changes in the membrane of the cells [97, 103]. Among all these changes, measuring the changes that occur in the size of the cells during the differentiation can provide useful cell morphological information that can later be used for selecting properly sorting and separation techniques (see section 4.1). Furthermore, the results from the cell size measurements enables us to investigate the relationship between the size of the cell and the resulting Young's elastic modulus.

To study the changes in the size of the cells, the radii of the cells (60 cells for each day of differentiation) were measured using the AFM imaging tools. To measure the radii of the cells an optical image of each cell was taken prior to cell indentation (for the elasticity quantifications). The diameter of the cells (from two different sides) was measured using the "measure the distance" function in the AFM imaging tool bar (Fig. 4-7). The radius [R_0] of each cell was obtained by using Eq. (4-1).

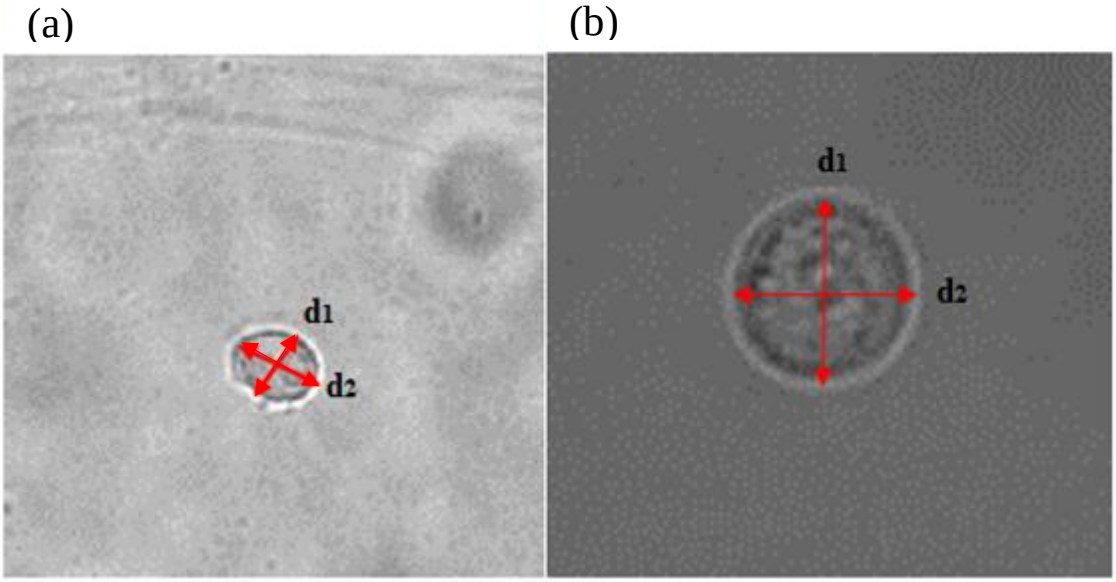

Figure 4-7. Diameter measurement of (a) non-spherical shape and (b) completely spherical shape cells for cell radius determination.

$$R_0 = \frac{1}{2}\frac{(d_1 + d_2)}{2} \tag{4-1}$$

Furthermore, to study cell shape changes and their relationship with the elastic properties and radius of the cells, the eccentricity of each cell was calculated using Eq. (4-2) and Eq. (4-3).

$$R_1 = \frac{d_1}{2} \quad and \quad R_2 = \frac{d_2}{2} \tag{4-2}$$

$$Eccentricity = \frac{2(R_1 - R_2)}{R_1 + R_2} \tag{4-3}$$

4.4.1 Size changes in the cord CD34+ stem cells during the differentiation

Radii distributions for the cells on each day of differentiation was plotted and is shown in Fig. 4-8. Referring to Fig 4-8, it can be observed that for day 11, the radius of most of the cells was in the range of 5.5-6.5 µm, with an average cell radius of 5.86 µm. For day 14 the radius peak shifted to the range of 4.5-5 µm with an average of 4.54 µm. Following further cell differentiation, at day 18, the majority of the cells had a radius in the range of 4-4.5 µm with an average of 4.24 µm. At day 21 of differentiation, most of the

reticulocytes had a radius in the ranges of 3.5-4 μm and 4.5-5 μm, with an average of 3.99 μm. Referring to Fig. 4-8, it can be seen that some of the reticulocytes are larger in size compared to day 18 cells. It should be noted that sometimes when the cells enter into natural death (apoptosis), they start to spread on the surface and as a result appear larger in diameter [104]. Therefore, the expansion in cell size can be an indication that some of the cells at day 21 were beginning to enter cell apoptosis.

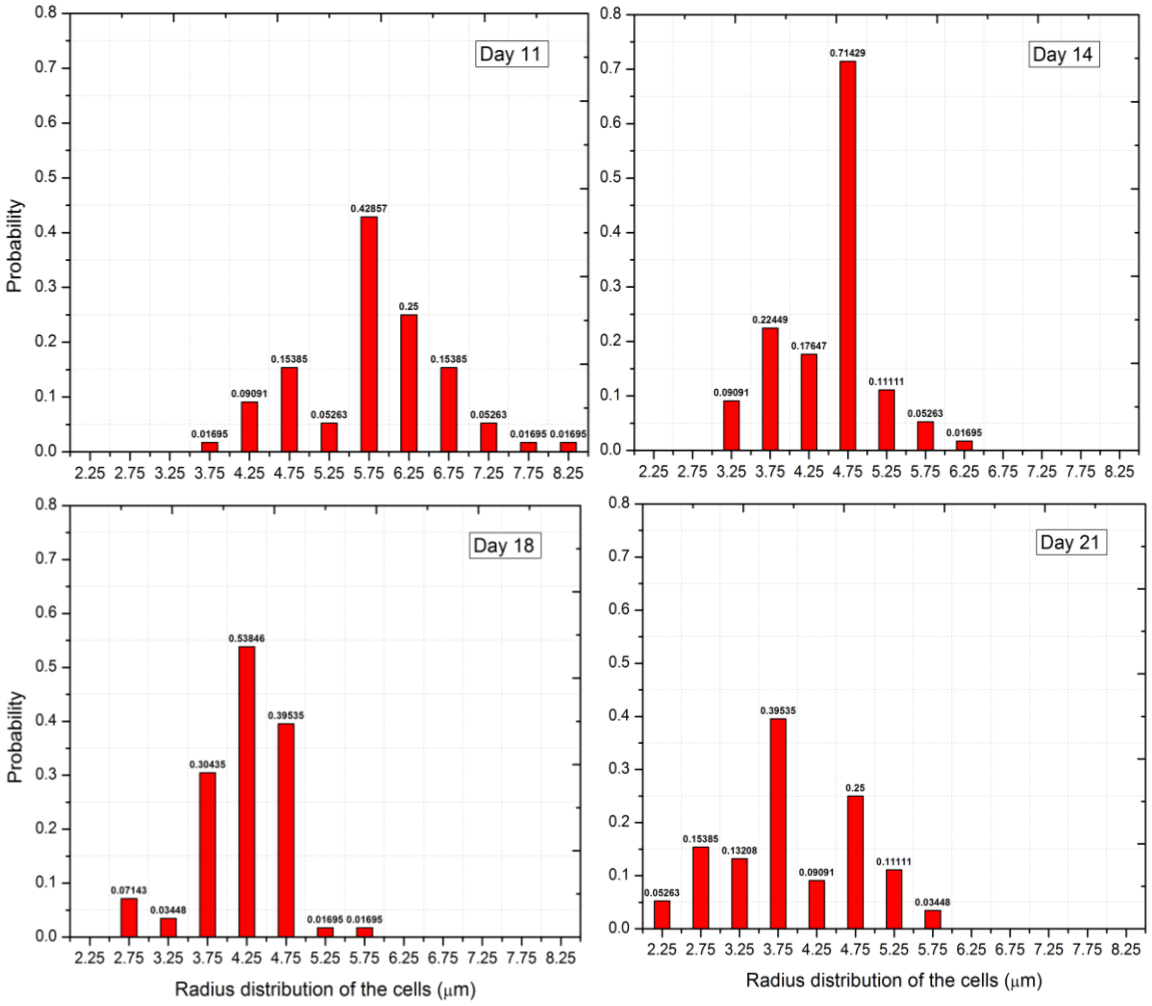

Figure 4-8. Radius distribution of the cells as they were differentiating, for days 11, 14, 18 and 21.

By comparing all four graphs, it can be seen that the size of the cells gradually shifts from across the ranges of larger sized cells to smaller size cell ranges as cells progress through the differentiation process. To statistically compare the radius changes during the differentiation process the boxplot for the radius distribution of the cells is plotted and P-value is calculated (Fig. 4-9). The statistical studies showed that the change in the radius between day 11 and all the other differentiation days is significant (****$p < 0.0001$).

However, between days 14 and 18 no significant changes observed. Also, the radius change between day 18 and day 21 is calculated as not significant.

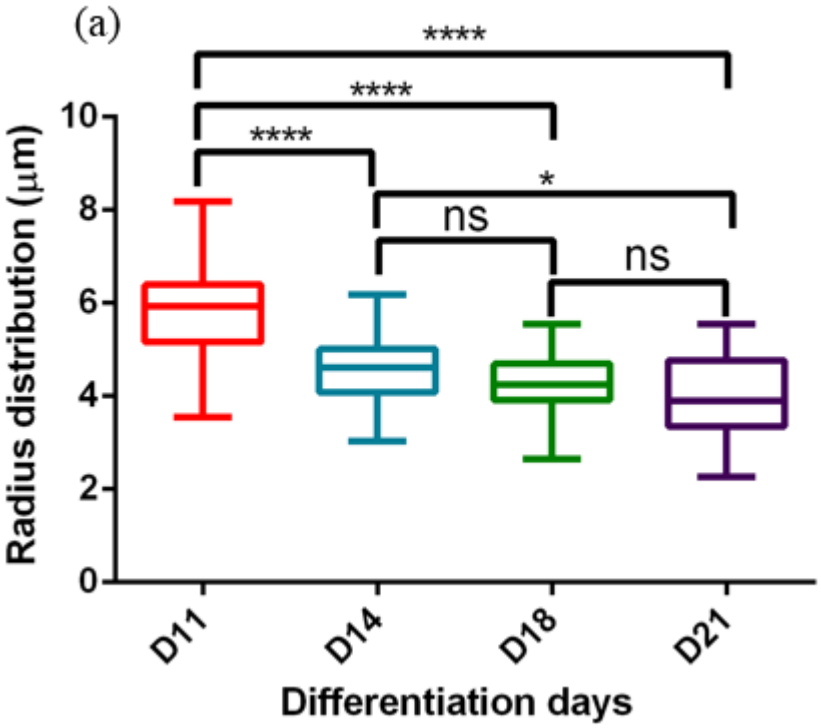

(b)

	D11 (µm)	D14 (µm)	D18 (µm)	D21 (µm)
Minimum	**3.56**	**3.03**	**2.65**	**2.27**
25% Percentile	**5.16**	**4.09**	**3.92**	**3.35**
Median	**5.92**	**4.61**	**4.25**	**3.89**
75% Percentile	**6.39**	**5.01**	**4.70**	**4.77**
Maximum	**8.17**	**6.17**	**5.55**	**5.55**
Mean	**5.86**	**4.54**	**4.24**	**3.99**
SD	**0.93**	**0.71**	**0.603**	**0.91**

Figure 4-9. (a) The radius distribution of the CD34+ cells during their differentiation process is presented using the boxplot (b) derived data from lower and upper quartile with median and standard deviation are summarised in the table.

Comparing cell radius changes between each day of differentiation using the mean values showed that, between day 11 and day 14 there was a 1.32 µm reduction in the radius of the cells, while the radius reduction between days 14 and 18 was less, calculated as 0.36 µm. From day 18 to day 21, the cell radius reduction was calculated as 0.25 µm, which shows that the reduction in radius was gradually decreasing. As explained above and showed in Fig. 4-9 (a), only radius changes from day 11 to day 14 is significant and from day 14 until end of the differentiation process no significant changes is observed in the cells. The significant changes in cells radius between days 11 and 14 is mainly due to the

fact that the enucleation process in the cells has begun. Additionally, 1.87 μm reduction in the radius of the cells was observed between days 11 and day 21. Furthermore, since the mature RBCs are expected to have diameter sizes in the range of 3.9 μm, it can be assumed that the trend in cell diameter size changes during the differentiation process was as expected [105]. Therefore, the results revealed that during the differentiation process the cells diminish in radius/size.

Moreover, to visualise the changes in the diameter of cells during differentiation, images of the cells were acquired using QI mode of the AFM, with imaging map sizes set at 32×32 μm. One acquired image per day of cell differentiation is presented in Fig. 4-10. All the images set are presented with the height channel scale. Referring to the images, changes in the height of the cells during the differentiation process can be observed. The acquired images show that there is a reduction in the height of the cells between days 11 and day 21, which could possibly be related to the nuclear condensation and enucleation processes. Furthermore, a reduction in the size of the cells during the differentiation process can be observed by the QI images.

Interestingly, referring day 18 in Fig. 4-10, the image shows an additional mass on top of the cell, which is possibly likely to be the nucleus being extruded from the cell and cell membrane not yet closed. However, additional experimental analysis would be needed to confirm this.

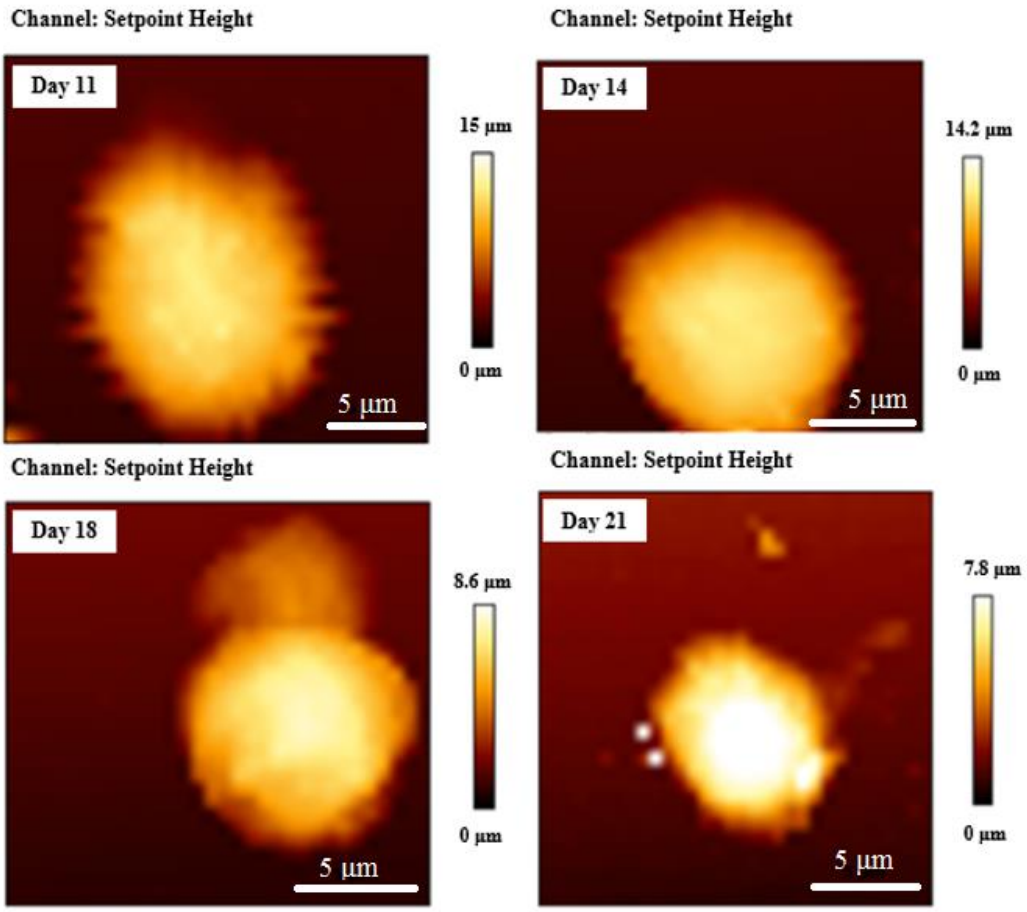

Figure 4-10. AFM QI images of the cells from days 11, 14, 18 and 21. The height channel was selected to demonstrate the images. The bars on the right side of the images shows the height range of the cell (following deformation from the probe).

In the following step, the relationship between the size of the cells and the elastic properties is studied. In Fig. 4-11, radius of all the cells from all differentiation days was plotted against the elastic moduli of the cells. As a general trend, it can be observed that, as the cells differentiate they diminish in size and become considerably softer. Referring to results from day 11, it can be seen that not all the aspects of the cells showed a similar size variation behaviour, with wide ranges of elastic moduli obtained for the cells. However, the results from day 21, revealed that all the aspects of the cells were very soft. Thus, there were no significant differences in the elastic modulus obtained from different locations on the cells. Therefore, since all the cells were attached to the petri dish under the same measurement conditions, it can be assumed that the stiffness observed on day 11 and 14 were not from the petri dish substrate/coating.

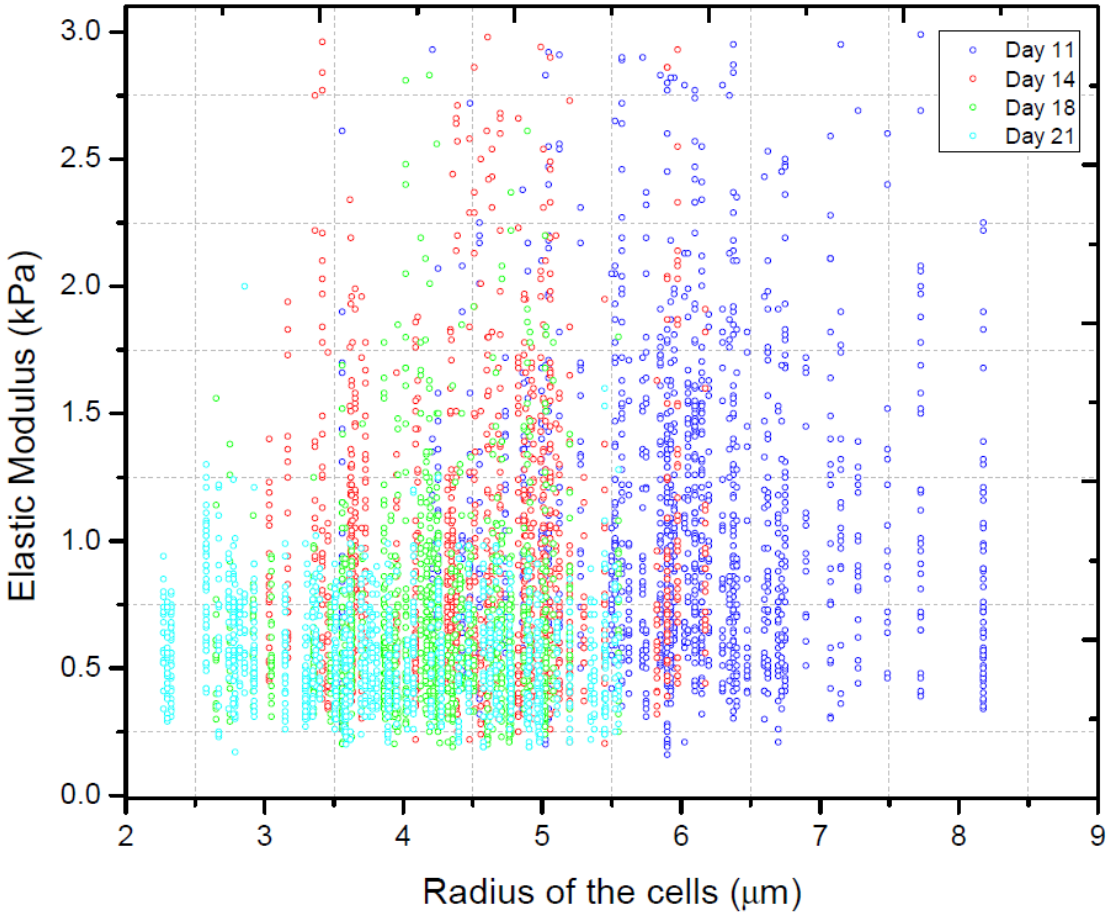

Figure 4-11. The relation between radius of the cells and derived elastic modulus from the Hertz-Sneddon contact model.

To quantify the degree of the radius and elastic modulus overlap (from Fig. 4-11), Receiver Operating Characteristic (ROC) curves were plotted and the corresponding area under the curve (AUC) calculated (Fig. 4-12). Using this approach, it can be determined that cell population classified in terms of elasticity, as day 11 cells, 42% of the cells belong to the day 14 cell population (AUC=0.58) (Fig. 4-12 (a)). For day 14 cells the AUC is 0.66, which means the 34% of the cells are from day 18 (Fig. 4-12 (b)). At day 18, the overlap with day 21 cells is 42% due to the AUC=0.58 ((Fig. 4-12 (c)). In terms of radius classification, day 11 cells have 14% overlap with the day 14 cells as the AUC=0.86 (Fig. 4-12 (d)). As day 14 cells, since AUC=0.63, 37% of the cells belong to the day 18 cells (Fig. 4-12 (e)). Also, for day 18 cells, 41% of the cells are overlapped with day 21 cells as AUC=0.59 (Fig. 4-12 (f)). For days 11 and 14 based on the AUC showed in Fig. 4-12 (a), elasticity-based separation between the cells would be possible but would result in a significant contamination. However, the radius difference between day11 and day 14 cells (Fig. 4-12 (d)) is 14%, suggesting the feasibility of size-based techniques to separate these populations. For the day 14 and 18 cell populations the obtained AUC from both elasticity (34%) and radius (37%) curves showed that while any

elasticity or size based separation techniques would result in contaminations, elasticity-based methods can be more effective for sorting and separating the cells (Fig. 4-12 (b and e)). Finally, for day 18 and day 21 cells the elasticity (42%) and radius (41%) difference showed that both elasticity and radius based separation methods would be possible but contaminations would be significant (Fig. 4-12 (c and f)).

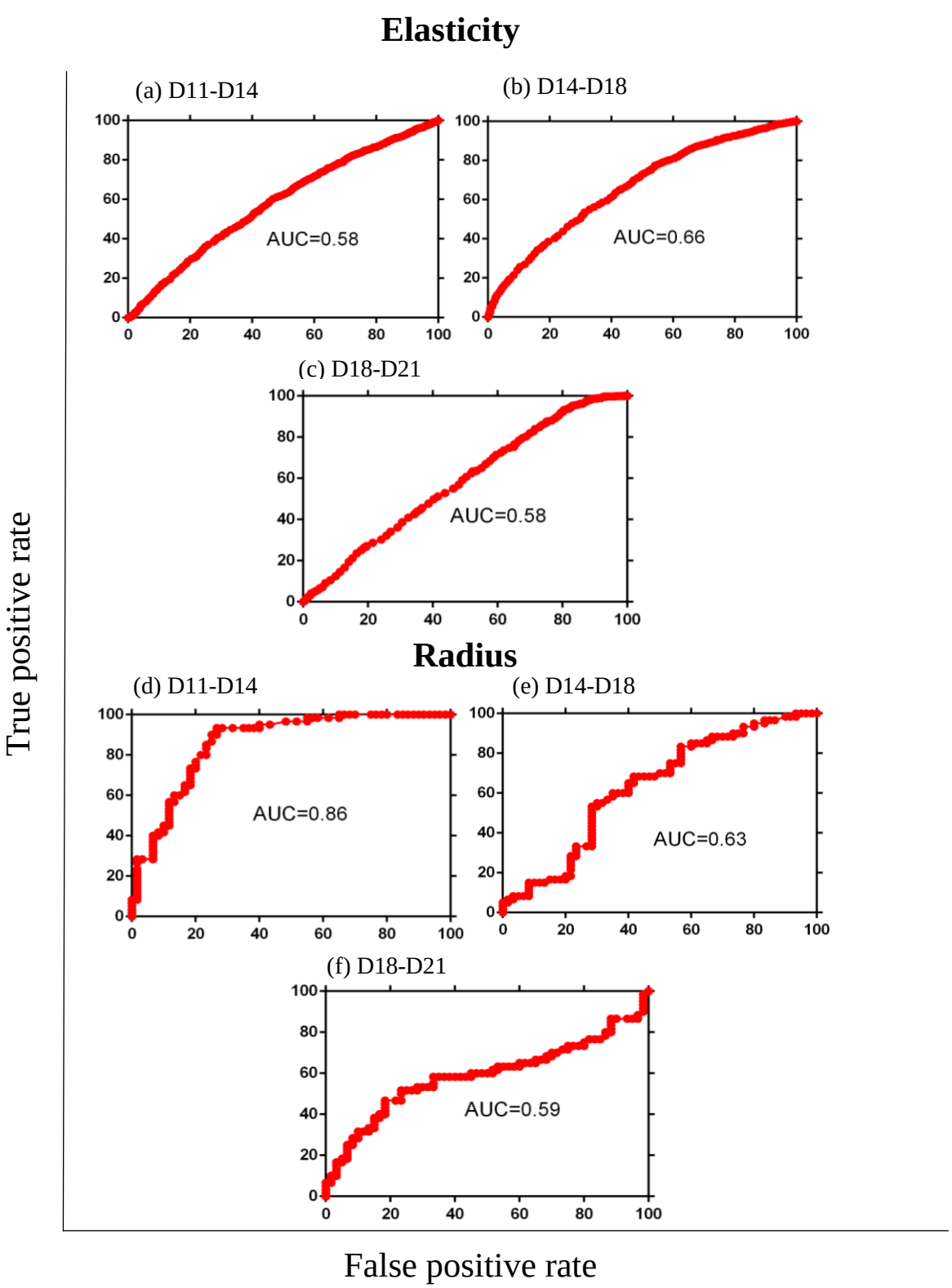

Figure 4-12. ROC curves were plotted for elasticity and radius for cells during the differentiation process. The True Positive Rate is defined as the number of the D11 (resp. D14, D18, D21) cells measured for a certain cut-off point (radius or elasticity) and divided by the total number of the D11 (resp. D14, D18, D21) cells. The False Positive Rate is the corresponding number of D11 cells (resp. D14, D18) divided by the total number of D14 cells (resp. D18, D21) for the same cut-off. The Area Under the Curve (AUC) was calculated to quantify the elasticity overlap between (a) D11 and D14 cells, (b) D14 and D18 cells, (c) D18 and D21 cells as well as radius overlap between (d) D11 and D14 cells, (e) D14 and D18 cells, (f) D18 and D21 cells.

4.4.2 Shape changes in the cord CD34+ stem cells during the differentiation and their relation with the elastic modulus

Lastly, as a final investigation, the shape changes of the cord CD34+ stem cells and its relation to their resulting derived elastic modulus was studied. The eccentricity of each cell was calculated using Eq. (4-3), and the obtained results were plotted against the Young's elastic modulus (illustrated by Fig. 4-13). Obtaining an eccentricity value equal to zero, meant that a cell has a spherical shape. An increase in the eccentricity value indicates that the shape of the cell is non-spherical/oval. Therefore, referring to the eccentricity values obtained from cells on day 11 showed that the most of the cells had spherical shape; however, from day 14, the number of the cells with non-spherical shapes increases. The change in shape of the cells as the differentiation process progresses can be related to the enucleation process. As the nucleus is extruded from the cell, the open end of the cell membrane needs time to close, which in turn will have an effect on the shape of the cell. Furthermore, the enucleated cells spread more on the surface of the substrate than the nucleated one. Moreover, as it can be seen from Fig. 4-13, the shape of the cells did not have any effect on the derived elastic modulus. Notably, the derived results agreed the expectation that since the elastic modulus of the cell is, its intensive property, it should not be affected by the size and shape of the cells [106].

In addition, the boxplot of the eccentricity of the cells during their differentiation process is plotted and the P-value is calculated for statistical analysis (Fig. 4-14). From the statistical analysis it can be seen that however cells shape tends to non-spherical/oval during the differentiation process, these changes are not significant at any days.

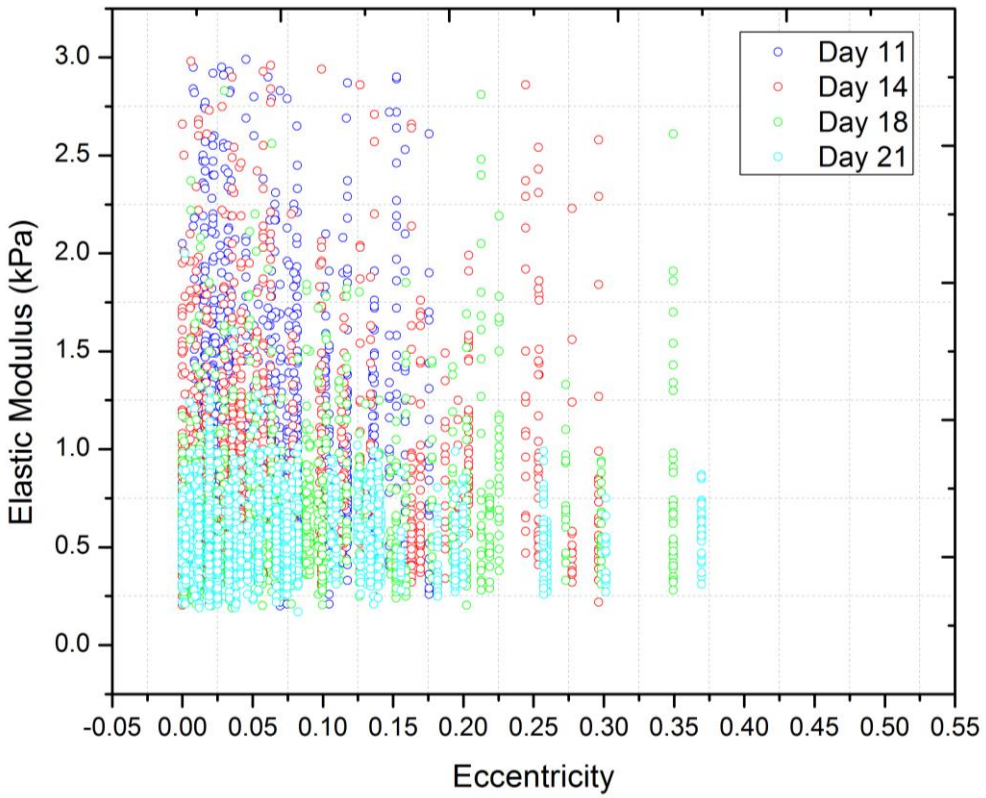

Figure 4-13. Shape of the measured RBCs determined by calculating cell eccentricity to study the relation between the shape and the elasticity of each cell.

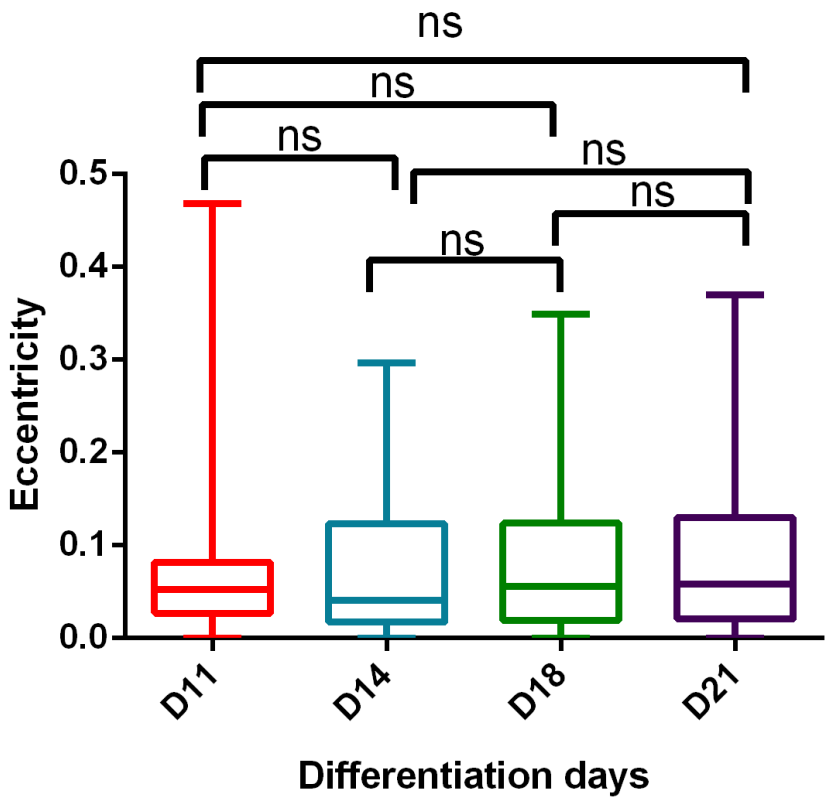

Figure 4-14. The eccentricity distribution of the CD34+ cells during their differentiation process is presented using the boxplot. Statistical calculations showed that there is no significant shape changes in the cells during their differentiation process.

4.5 Concluding remarks

Previous literature has shown that there is a massive requirement for the *in vitro* production of RBCs. Based on this necessity, proper cell purification and separating techniques are needed to improve for the "in-process" control, as well for the final products. Utilising a cell separation techniques based on the biomechanical properties of cells has the potential to produce less drawbacks and be more efficient in producing cell sorted donor blood products. Therefore, this Chapter was aimed at studying the mechanical properties of the umbilical cord blood CD34+ stem cells during their differentiation process.

The main conclusions of this study are:

- The derived Young's elastic modulus of the cells showed that during cell differentiation and enucleation processes, cells become softer. Statistical analysis showed that the changes in the Young's elastic modulus of the cells during the differentiation process is significant. Also, 0.5 kPa reduction in the total elasticity was observed from day 11 to day 21 of the cell differentiation process;

- Radius measurements of the cells, revealed that during the differentiation process cells diminish in radius. The most significant changes in cell radius occurred between days 11 and 14 of the differentiation process due to the enucleation process. An overall of 1.87 μm radius reduction was observed between day 11 and day 21;

- Investigations on the shape of the cells showed that while the majority of the cells have the spherical shape, during the differentiation and enucleation process, some of the cells present with a non-spherical shape. However, the statistical analysis showed that no significant shape changes occurs during the cells differentiation process.

The main aim of measuring elastic properties and radius of the CD34+ cell during their differentiation process, was applying the results for selecting/designing the sorting and separation techniques. Therefore, further analysis were performed with the aid of using the ROC curves to clarify the elasticity and radius overlap of each day of differentiation with the other days. Obtained results showed that size-based techniques can provide a high efficient sorted culture for separating day 11 cells from day 14 cells. However, for

sorting day 14 cells from day 18 and day 18 cells from day 21, any elasticity or sized based techniques cannot provide a highly purified/sorted culture and significant contaminations would be remained.

Moreover, it is possible to assume that the main reason for most of the observed mechanical and size/shape changes in the cells during the differentiation process, is a result from the processes that occur during the cell enucleation process. Additional investigations on this assumption were performed and the results of which presented in Chapter 5.

Obtained results from testing the mechanical properties of the cells were provided useful information, which can be used to select/design a proper and high yield sorting and separating techniques with the minimum downsides. Since, the elasticity and size of the cells were changing during the differentiation, at each step of differentiation, different techniques can be selected to achieve more efficient separation.

CHAPTER 5

Study on the mechanical and physical properties of pyrenocytes for understanding the effect of nucleus and enucleation process on mechanical properties of cord CD34+ stem cells

Contents

5.1 Introduction

The enucleation process is a critical step during the differentiation and maturation of umbilical cord blood CD34+ stem cells. The enucleation process mostly starts during the differentiation process. While producing cells *in vitro*, the enucleation process generally starts from day 14, with majority of the cells enucleated by day 21. As discussed in Chapter 4 (see Fig. 4-1), during differentiation, developing cells undergo four or five divisions to generate reticulocytes. The morphological changes that occur through each stage of differentiation show the decrease in the size of the developing cell's nucleus.

During the differentiation process, the cell's nucleus becomes denser and gradually isolated from the cytoplasm (through formation of a cytoplasmic membrane layer). The nucleus then moves to one side of the cell and stays close to the cell membrane. In Most cases, by day 18 of cell development, Orthochromatic Erythroblasts separates into two structures (1) the reticulocyte – which contains most of the remaining cell cytoplasm, and (2) the pyrenocyte, which is the condensed cell nucleus covered in a thin layer of cytoplasm. This process is called enucleation/nuclear extrusion [97, 100].

During the *in vivo* process of differentiation and maturation of RBCs, the extruded pyrenocytes are engulfed by the macrophages and transported to the bone marrow to undergo degradation and apoptosis [107]. However, when producing reticulocytes *in vitro*, there is no naturally occurring process in the cell developmental protocol to degrade the pyrenocytes. Therefore, purification, sorting and separating processes are required to separate the pyrenocytes from the culture media of the cells.

Given that there appear to be no evidence for research carried out investigating the mechanical and physical properties of the pyrenocytes. Investigating their mechanical characteristics can be used as a tool for developing more appropriate techniques for the in-process control and separation techniques of current cell separation technologies. Therefore, the work in this Chapter was designed to measure and study the physical properties of sixty pyrenocytes (elasticity, size and shape) using AFM. In addition, the effect of the nucleus on the derived elastic modulus of the cells, as well as the relationship between the height of the cells and the cell nucleus region is studied. For this purpose, the elasticity of different points on each cell from day 11 (obtained in the Chapter 4, section 4-3), along with their measured cell heights, are compared with each other. This method is used to find the nucleus region of the cell, and then compare the elastic modulus of the nucleus region with the rest of the cell. Finally, the assumption that the stiffer locations of the cells are a result of the nucleus organelle is proved by using the sorted cells (nucleated and enucleated) from day 14. The results obtained from measuring the mechanical properties of the sorted cells, was then compared with the results from measuring the mechanical properties of the mixed culture.

The studies carried out in this Chapter will hopefully provide information for optimizing the sorting and separation techniques, while improving our knowledge about the physical properties of pyrenocytes.

5.2 Elastic properties of pyrenocytes

To study the elasticity of the pyrenocytes, sixty samples from days 14, 18 and 21 were selected. All the indentations were performed using AFM QI mode with QI map sizes of 8×8 pixels, which provided 64 force curves per pyrenocyte. Any curves obtained from the culture dish coating and/or the culture media were discarded, such that only results curves for each pyrenocyte were collected. The obtained results from all pyrenocytes were then sorted into the different ranges of elasticity. Finally, to study the elastic modulus of the pyrenocytes, each range of the elasticity was plotted against the calculated probability of each elastic modulus.

The derived elastic modulus results for the measured sixty pyrenocytes are presented in Fig. 5-1. The obtained results showed that the most locations on the pyrenocytes have a derived elastic modulus in the range of 4.51-6 kPa and 3.1-4.5 kPa respectively. Interestingly, a large range of derived elastic modulus values (from 1 kPa up to 27 kPa) was observed for the pyrenocyte measurements. However, interestingly, certain locations with high stiffness values were observed only in some pyrenocytes, and not all of them (this is investigated in section 5.3). Therefore, although the majority points on the pyrenocytes produced elasticity values in the range of 4.5-6 kPa, the presence of stiffer locations on some pyrenocytes caused the average elastic modulus to vary at 7.11 kPa.

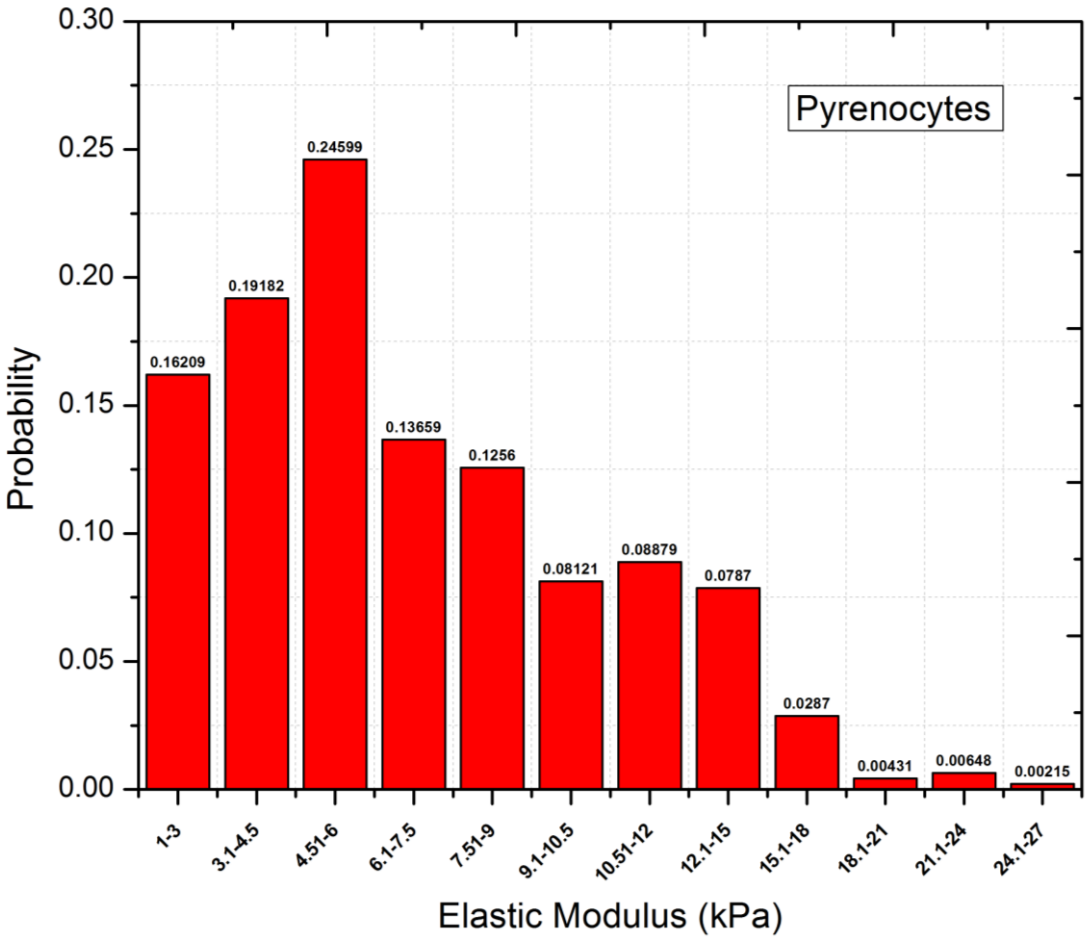

Figure 5-1. Probability distributions of the Young's elastic modulus of the pyrenocytes extruded from the cells at the differentiation days of 14, 18 and 21.

For all sixty measured pyrenocytes, the derived elastic modulus values obtained from different locations of each pyrenocyte is plotted in Fig. 5-2. Referring to the plotted results, it can be observed that the elastic modulus obtained for most of the pyrenocytes is distributed in the range of 3-6 kPa with the median derived as 5.89 kPa, while rare locations on some pyrenocytes have extremely high elastic modulus values.

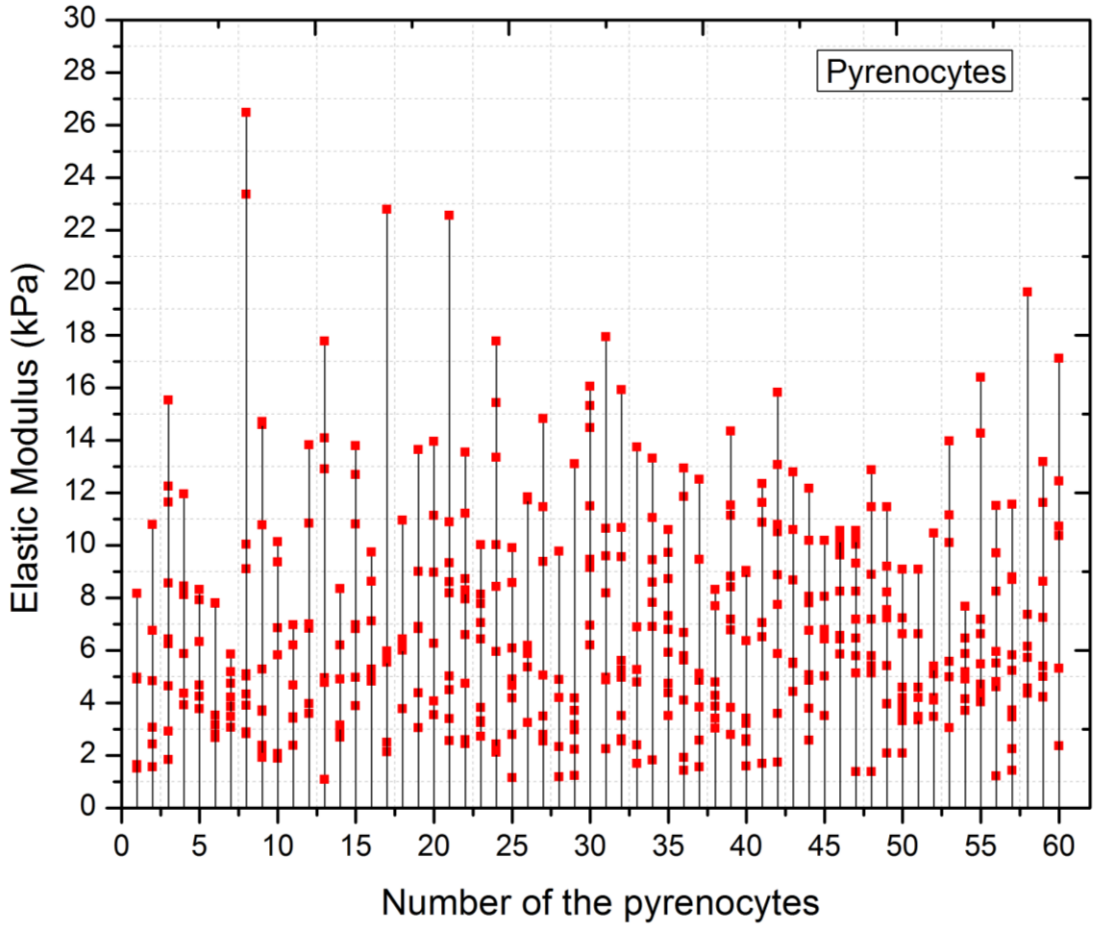

Figure 5-2. Elastic modulus values obtained from different locations on the surface of each pyrenocyte plotted to observe the distribution of the elasticity in every pyrenocyte. Each "■" represents a single measurement on the surface of a pyrenocyte. Vertical lines link points taken from the same pyrenocyte.

Following on from this, the obtained elastic distributions from all sixty pyrenocytes were then compared with the elastic distribution of every single pyrenocyte. This was carried out in an attempt to understand if every single pyrenocyte follows the same trend for the elastic distribution obtained for all pyrenocytes. The elastic trends obtained for all single pyrenocytes is presented in the Fig. 5-3 (presented as elastic probability distribution). Referring to the graphed data, it can be observed that the main peaks in Fig. 5-1 is presented in every single pyrenocyte while only few number of the pyrenocytes have the points with high stiffness on them. The reason for observing few pyrenocytes with some high elastic modulus locations on them is further investigated in the following section.

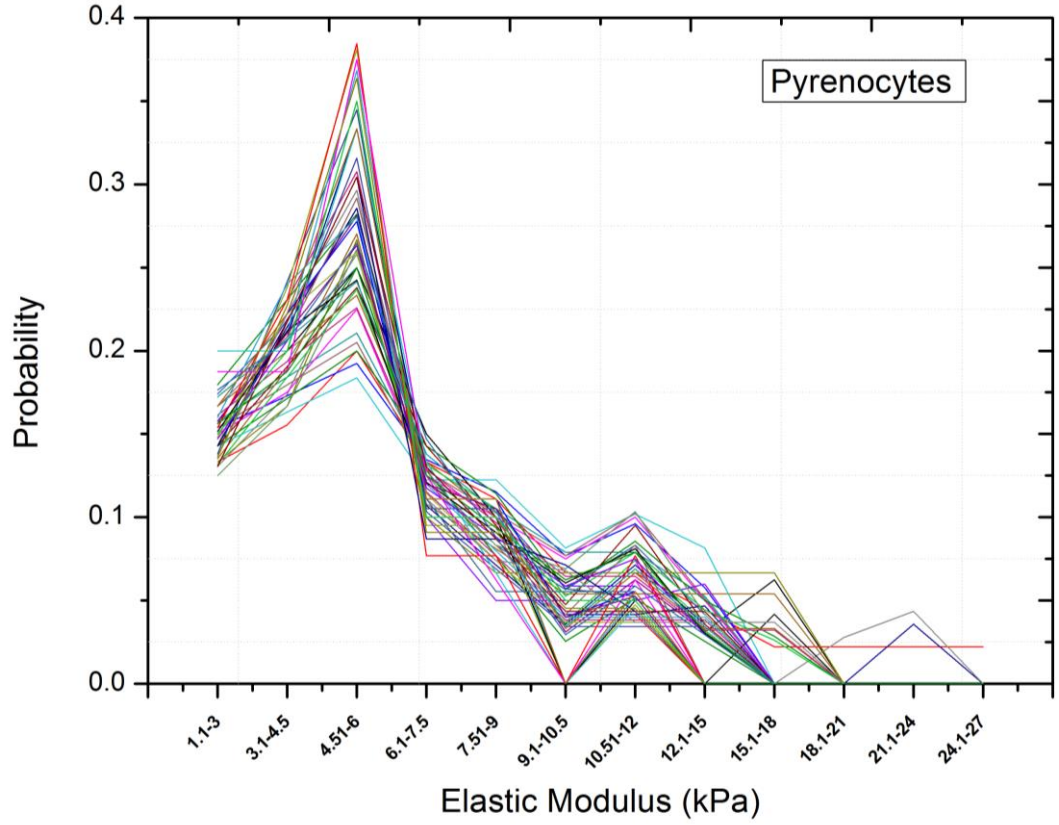

Figure 5-3. Probability distributions of the Young's elastic modulus for all sixty pyrenocytes.

5.3 Effect of time on the elasticity of pyrenocytes

As it is mentioned in the previous section, a large range of elasticity values was obtained for the pyrenocytes. To study and investigate where this trend may arise from, we sorted the derived elasticity values of each pyrenocyte based on the "indentation time". Considering the starting minute of the experiment as time = zero, allocations for the indentation time were made for every 15 minutes. The resulted in Fig. 5-4 were plotted using the median elastic modulus, as well as all the elastic moduli values obtained from the cells against the time values collected for indentation time. Also, boxplot is provided with the statistical analysis to study the effect of time on the Young's elastic modulus of the pyrenocytes. Referring to Fig. 5-4 (a), it can be observed that the median elasticity of the pyrenocytes increases gradually for the first 45 minutes of following the start of the experiment. The median elasticity trend then increases rapidly before dropping for another 15 minutes. Lastly, during the remaining end 15 minutes, the median elasticity trend increases with more speed. In Fig. 5-4 (b), the elastic modulus derived from all indented points on each pyrenocyte was plotted against the time. The obtained results showed that however majority of the points on different pyrenocytes have similar elastic

modulus, as the time passes the stiffer locations on the pyrenocytes start to appear. These stiff parts can be the locations on the pyrenocytes, where the cytoplasm starts to degrade. However, as it can be seen in Fig. 5-4 (c) the statistical analysis showed that there is no significant changes in the elastic modulus of the pyrenocytes during the indentation time. Only, between the first 15 minutes and the final 15 minutes a slight difference is observed (* $p < 0.01$).

This increase in the stiffness of the pyrenocytes could be explained by the fact that the extruded pyrenocytes have a ring of cytoplasm containing a protein matrix that surrounds them. This protein matrix and the cytoplasm membrane degrade gradually as the pyrenocyte becomes extruded to outside of the cell, until it disappears completely [100]. As the pyrenocytes are ejected to the outside of the cells, it takes time for their protein matrix to undergo complete degradation. Therefore, while the newly ejected pyrenocytes have lower elastic moduli values (due to their cytoplasmic covering), the pyrenocytes which have started to be degrade, or completely degraded, show higher elastic moduli values. However, the results of all the elastic moduli values for whole pyrenocyte sample group, showed that although the distribution of elasticity in most of the cells are quite similar, as time passes, some locations on the pyrenocytes start to become stiffer. Moreover, scanning electron microscopy (SEM) images of the pyrenocytes from a colleague (see Appendix A) shows that the newly extruded pyrenocytes have a layer of cytoplasm around them (Fig. A-1). However, the pyrenocytes which are in the dish for longer time do not have the cytoplasmic layer around them or only some parts of the cytoplasmic membrane remained on them (Fig. A-2). Therefore, obtained Young's elastic modulus from pyrenocytes is highly dependent on the indented location.

However, it is clear that much additional work (with more biological back-ups) will be required before a complete understanding of the effect of time on the elastic modulus of pyrenocytes and the effect of cytoplasmic layer on the elastic properties of pyrenocytes.

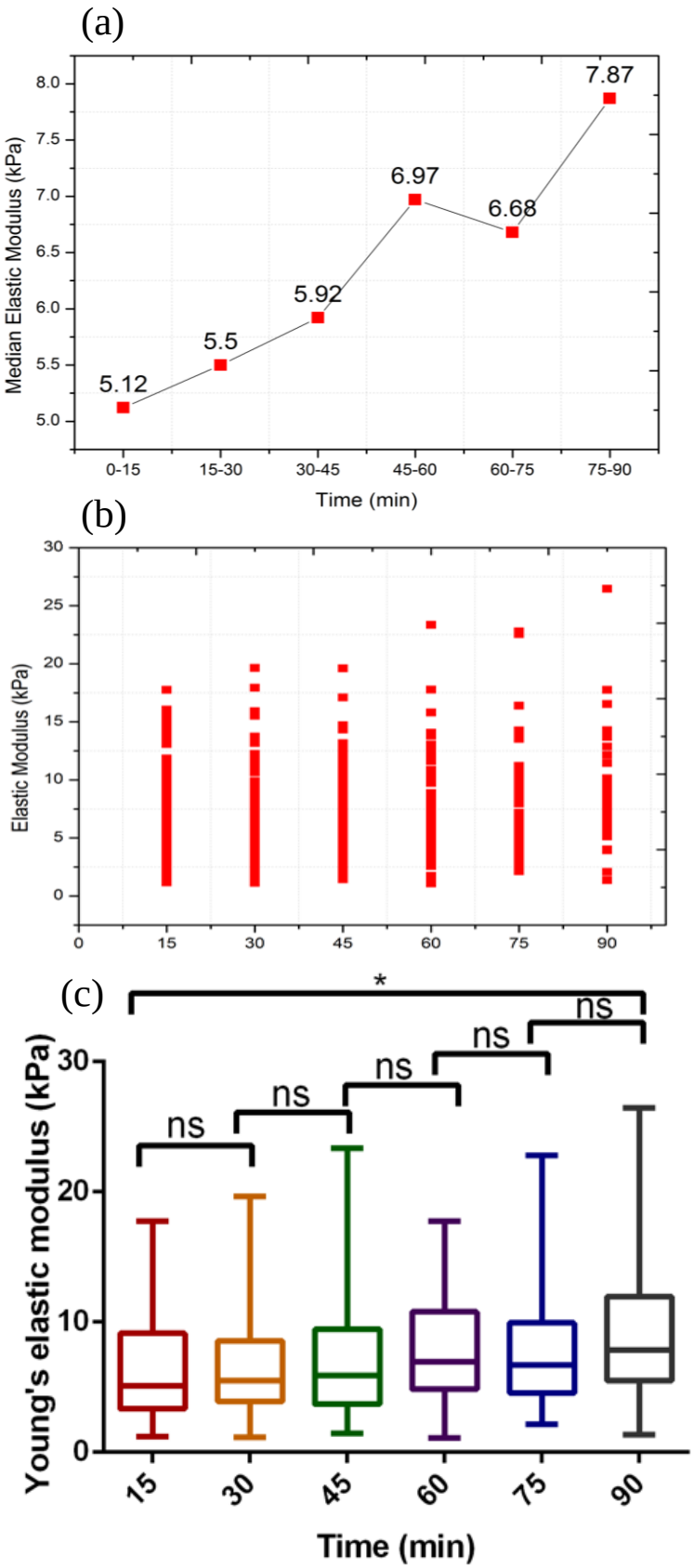

Figure 5-4. To understand the effect of the degradation of the protein matrix around the pyrenocytes on their elastic modulus, (a) median elastic moduli values derived from each pyrenocyte and (b) all the elastic modulus values from different point on each pyrenocyte are plotted against the time of indentation. (c) Boxplot is summarising the elastic distribution over the time. Also, no significant changes in elasticity of the cells derived from P-value calculations.

5.4 Size and shape studies

5.4.1 Size of the pyrenocytes and their relation with the Young's elastic modulus

Studying the size of pyrenocytes can be useful for cell separation purposes. As previously described, when producing the reticulocytes *in vitro*, the developing cells extrude their nucleus (enucleation), which they remain in the cell culture media. Therefore, the cell culture media is a mixture of the enucleated cells, nucleated cells and the pyrenocytes. Measuring the radius of the pyrenocytes, and comparing this with the radius of developing cells can provide useful information that could be highly beneficial for designing and improving cell filtration techniques. Cell sorting filters of the correct dimensions can be designed to allow the pyrenocytes to pass/filter through them; all the while keeping the remaining developing cells behind the filter. Since reticulocytes are naturally soft cells (see Chapter 4, section 4.3), designing the right size of filters for pyrenocyte sorting, is essential to prevent the cells from squeezing through filters, while the pyrenocytes can pass through the filter meshes with ease.

To investigate size effects on the elasticity measurements of pyrenocytes, size measurements i.e. measuring the radius of the sixty pyrenocytes was carried out using the AFM. The diameter of each pyrenocyte was measured from two different sides of each pyrenocyte before indenting it to acquire the elasticity measurements. Following this, the average of all measured diameters was calculated, and then divided by two to derive the radius of the pyrenocytes (see Chapter 4, section 4.4 for equation).

The size measurements done on the pyrenocytes evidenced that most of the pyrenocytes have radius in the range of between 1.9-2.0 μm, thus, the mean average radius of the pyrenocytes was calculated as 1.96 μm (Fig. 5-5). Comparing the calculated radius of the pyrenocytes with the derived radius of the cord CD34+ stem cells (see Chapter 4, section 4.4), showed that the cord CD34+ stem cells at differentiation days of 11, 14, 18 and 21 are respectively 3.9 μm, 2.58 μm, 2.28 μm and 2.03 μm larger than the pyrenocytes. As is mentioned in Chapter 4, section 4.2, reticulocytes are the final products in the *in vitro* cell production process. Therefore, cell separation processes are mainly required at the final stages of *in vitro* reticulocyte production to sort and separate the reticulocytes from the pyrenocytes. Having improved knowledge about the size differences between the pyrenocytes and the reticulocytes is essential and highly useful to design/choose proper cell sorting and separation technique with high efficiency.

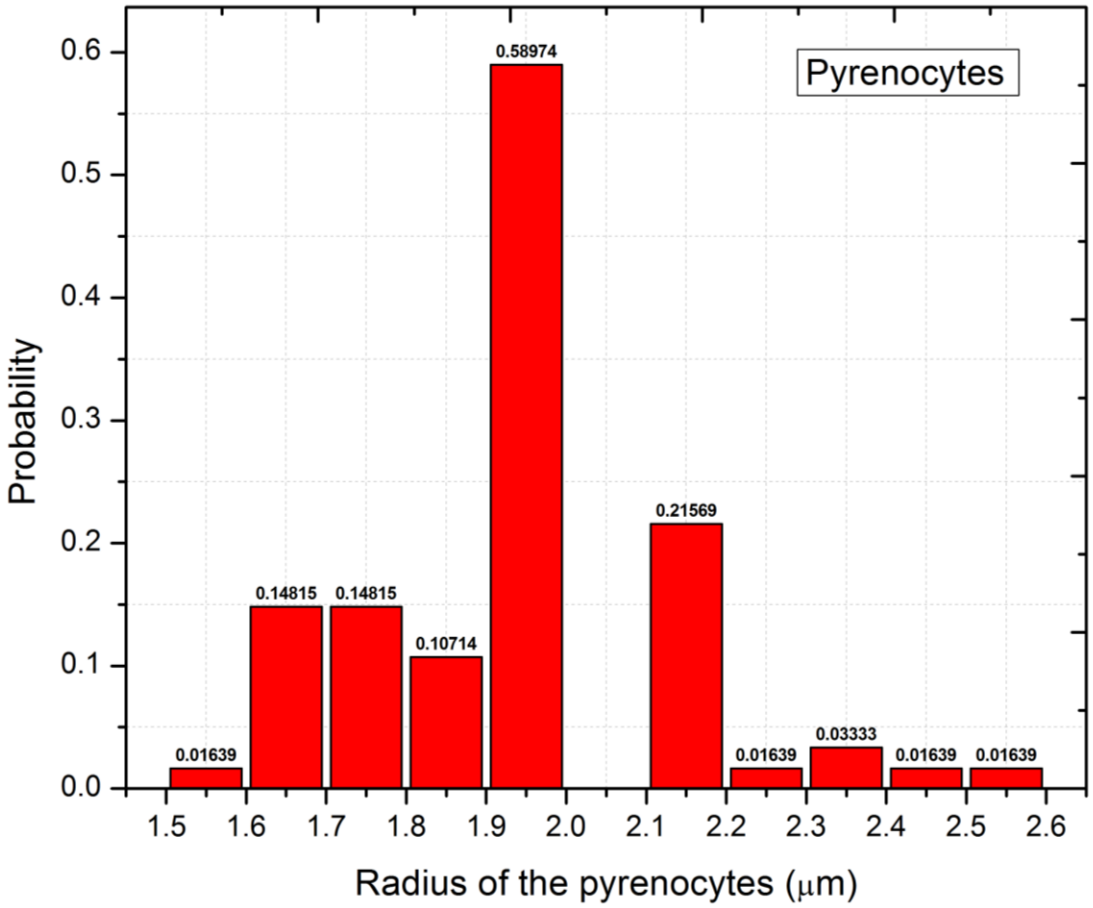

Figure 5-5. Radii distribution measurements for the sixty pyrenocytes measured with the AFM, prior the elasticity indentation measurements.

In order to understand the physical relationship between the size of the pyrenocytes and their resulting elastic modulus, the derived radius of each pyrenocyte was plotted against the obtained Young's elastic modulus. The obtained results for the cord CD34+ stem cells are also included in the analysis plot to compare cord CD34+ stem cells elasticity and size, with pyrenocyte elasticity and size. Referring to the comparison (Fig. 5-6), it can be noted that while cord CD34+ stem cells become softer and smaller in size during the differentiation process, pyrenocytes are significantly stiffer (with at smaller sizes) compared to the cord CD34+ stem cells. Therefore, this suggests that a size exclusion based techniques could be applied for sorting and separating the cells from the extruded pyrenocytes in their culture media. Furthermore, by considering the effect of time in relation to the changing elasticity of the pyrenocytes (see section 5.3), the elasticity based separation techniques can be used to sort and separate the cells from pyrenocytes.

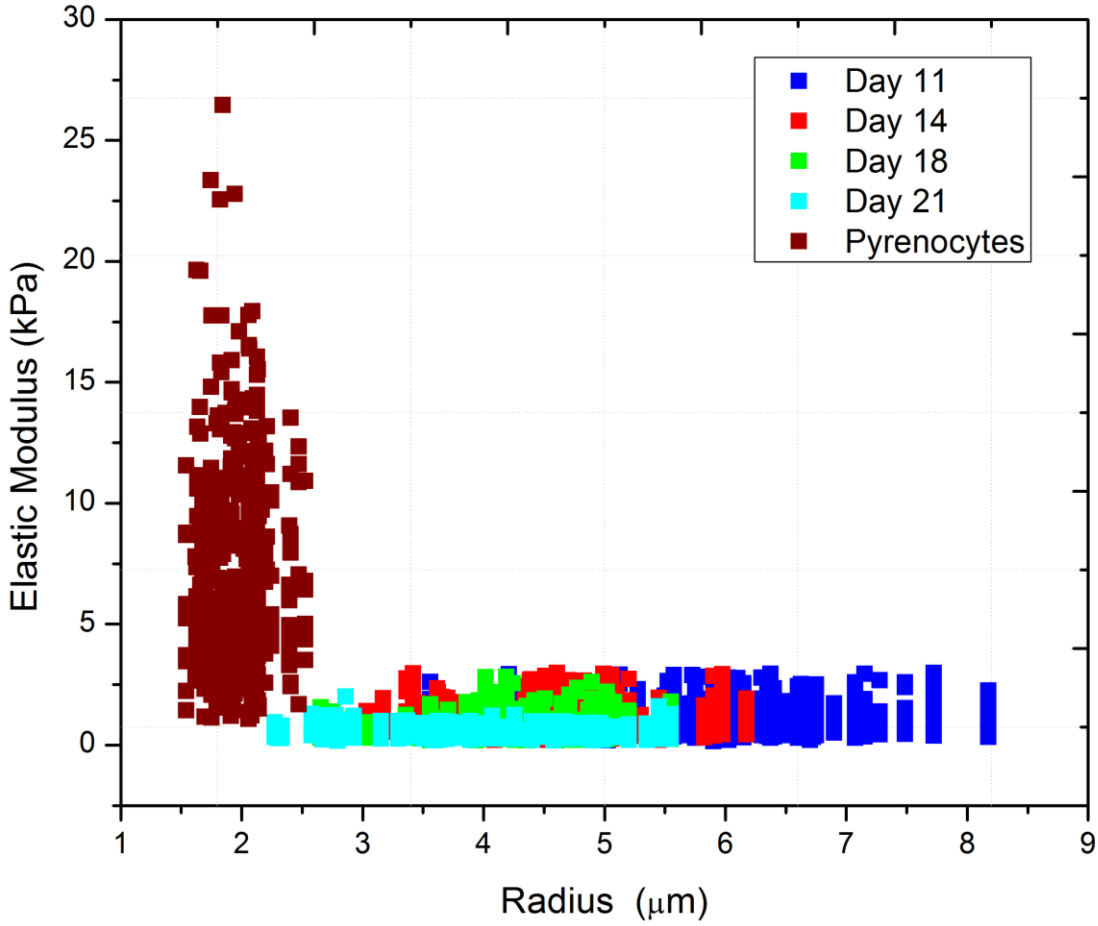

Figure 5-6. Relationship between the radius of the sixty pyrenocytes and their resulting Young's elastic modulus calculated using the Hertz-Sneddon model. The previously obtained results for the umbilical cord blood CD34+ stem cells size and elasticity measurements are also presented in the graph for comparison purposes.

5.4.2 Shape of the pyrenocytes and their relation with the Young's elastic modulus

In the case of studying the relationship between the shape of the pyrenocytes and their resulting elastic modulus, the eccentricity of each pyrenocyte was calculated and the results were plotted against their resulting derived Young's elastic modulus. Pyrenocyte eccentricity was calculated in exactly the same way as previously described in Chapter 4, section 4.4. To image a single pyrenocyte for eccentricity measurements, QI mode on the AFM was utilised, with map sizes of 32×32 μm used. The selected size of cell imaging map, which is selected for QI imaging, required roughly 20 minutes for completion. Since the pyrenocytes were able to tolerate the applied force during the imaging process, without rupturing or bursting (shape of the force-indentation curves change significantly if the indenting sample ruptures/bursts), they were imaged while they were viable (without fixation). An example image acquired of one pyrenocyte is presented in Fig. 5-

7. As the presented image is set on the height channel, it can be seen from Fig. 5-7 that there is a uniform height across the imaged pyrenocyte.

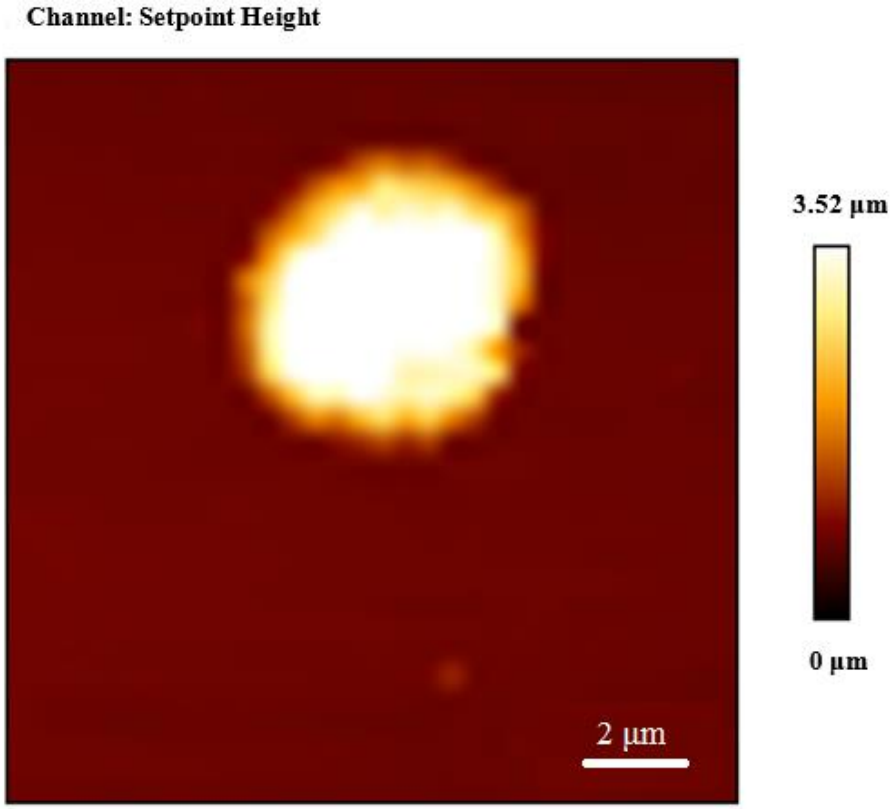

Figure 5-7. QI AFM image of a single pyrenocyte acquired while it was still viable (non-fixed state). Based on the height bar on the right side of the image, most of the surface area of the pyrenocyte had a uniform height at around ~3.5 µm.

The relationship between the shape of the pyrenocytes and their derived Young's elastic modulus, was studied by calculating the eccentricity of the pyrenocytes. The obtained results were then plotted (Fig. 5-8) and analysed. Referring to the plotted results (Fig. 5-8), it can be seen that all of the pyrenocytes are quite spherical in shape, and there is no shape variation among them. Therefore, regarding pyrenocytes shape and orientation there will not be any concern while designing filters with the same shape of the meshes for the separation purposes. Furthermore, it was found that the shape and elasticity of the pyrenocytes do not follow any trend and they are not related.

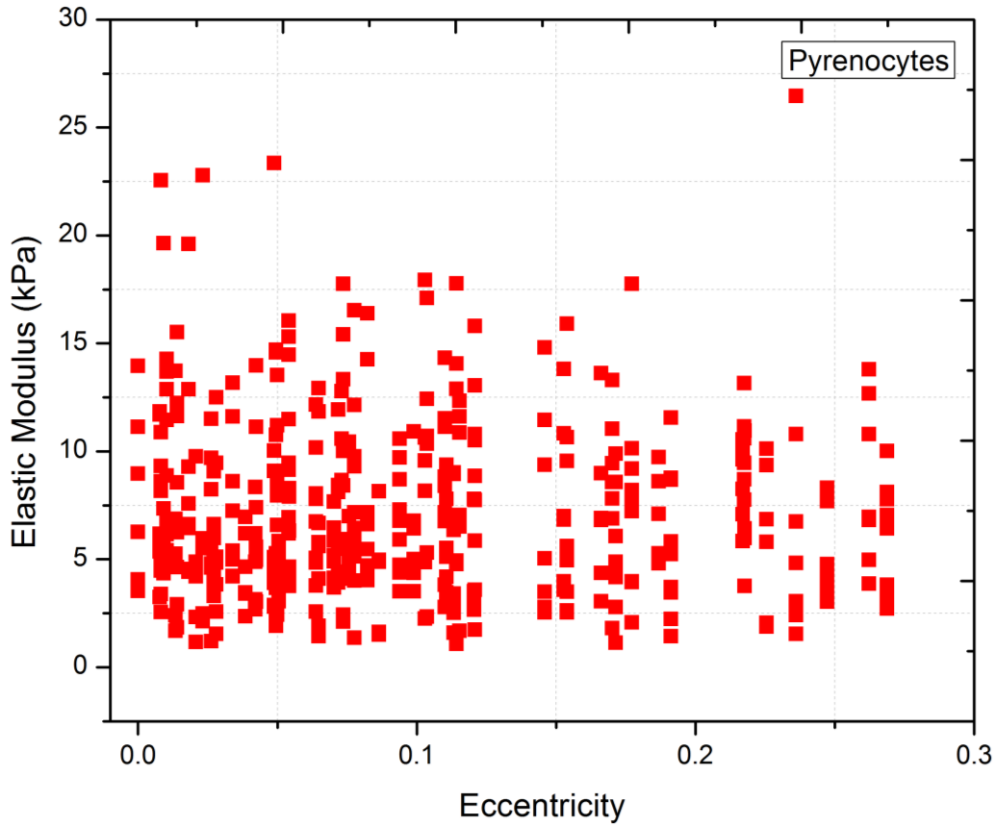

Figure 5-8. Relationship between shape and elasticity of the pyrenocytes, determined by calculating the eccentricity of each pyrenocyte and plotted against the derived Young's elastic modulus.

5.5 Study the effect of nucleus on the Young's elastic modulus of the cells

In Chapter 4, the changes in the derived elastic modulus of umbilical cord blood CD34+ stem cells during their differentiation process was tested and analysed. The obtained results from each cell showed that different locations on the cells have different elasticity outputs. This variation in elastic modulus on each cell was mainly observed in the cells on days 11 and 14 of differentiation. The difference in elasticity between the alternate locations, were considerably varied with a variation between 0.3 kPa to 2.9 kPa. However, for cells on days 18 and 21 the variations in elastic modulus reduced significantly.

While most of the cells from days 18 and 21 of differentiation are enucleated, cells on day 11, and most of the cells on day 14 still have their nucleus. Therefore, this variation in elasticity for day 11 and day 14 could be related to the presence of the cells' nucleus. Therefore, for the next analysis, a series of experiments were designed to understand if the derived variation of elastic modulus from day 11 and day 14, result from the effects of presence of the cell nucleus.

In the following section, the effect of the nucleus on the derived elastic properties of the cells was studied. Since all the cells from day 11 of the umbilical cord blood CD34+ stem cells differentiation are still nucleated, all sixty cells from day 11, with their derived elastic properties studied in the Chapter 4, section 4.3, were used for testing the effect of the nucleus on the elasticity of the cell. Furthermore, as cells on day 14 of cell differentiation are a mixture of nucleated and enucleated cells, cells from day 14 of cell differentiation were sorted into two groups of nucleated and enucleated cells using the FACS method (see Chapter 4, section 4.1). Each group was then analysed against the derived elastic properties, and compared in order to understand if the stiffer locations on the cells can be related to the cell nucleus region.

5.5.1 Analysing Young's elastic modulus of proerythroblasts for nucleus studies

The Young's elastic modulus derived from indenting different locations on a single proerythroblast (cell at day 11 of differentiation), showed that some locations are far stiffer than the others. The higher elastic modulus outputs could be an indication of the nuclear region; however, it could also result from the edges of the cells attaching to the petri dish/coating. For this reason, all sixty cells from differentiation day 11 were analysed by overlaying the microscopic images of the cells with the AFM images acquired for them. The cell AFM images were all acquired with the height channel activated. Therefore, the shallowest parts around the cell, where the cell edges are attached to the petri dish, and the higher parts of the cell (possibly the nucleus region) can be visually illustrated. For each cell, the AFM image and the overlayed image were presented together in order to clarify which area of the cell was indented. Numbering of the locations on the cells in the AFM image was based upon the index number of the acquired AFM map, and shows the locations where the elastic modulus for each cell location was calculated and used for analysis purposes. Furthermore, for each indentation location, the derived Young's elastic modulus and corresponding height of that location, noted in a table beside each image for comparison purposes (two examples of such analysis are provided in Fig. 5-9). The height of each location was derived from the force-displacement curve obtained from the AFM. In the force-displacement curve, the point where the curves starts to rise up shows the height of the indented location (see Chapter 3, Fig. 3-3).

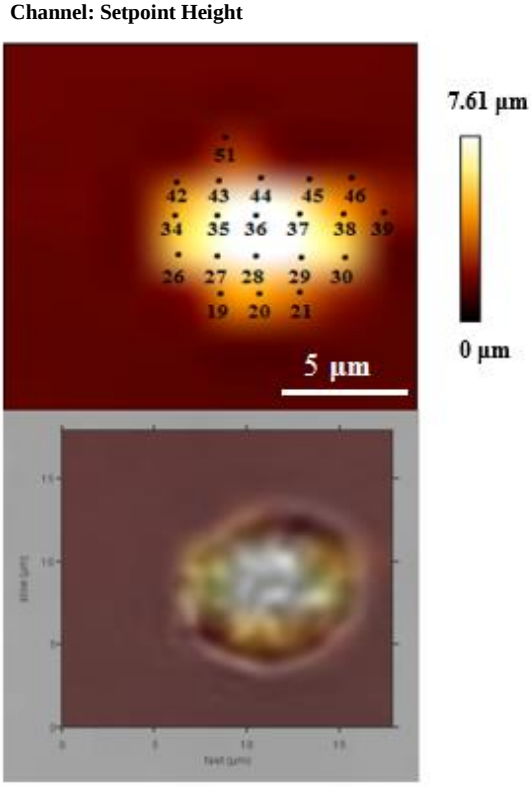

Number	Elastic Modulus (kPa)	Height (µm)
19	0.75	4.05
20	1.24	4.17
21	0.88	4.57
26	0.93	5.53
27	1.03	6.94
28	1.52	7.27
29	1.51	6.93
30	0.75	6.78
34	0.41	6.36
35	0.45	6.73
36	2.07	7.55
37	1.58	7.6
38	0.51	6.93
39	0.94	5.16
42	1.1	5.5
43	0.71	6.58
44	1.12	7.2
45	1.11	6.87
46	0.71	5.65
51	0.67	4.44

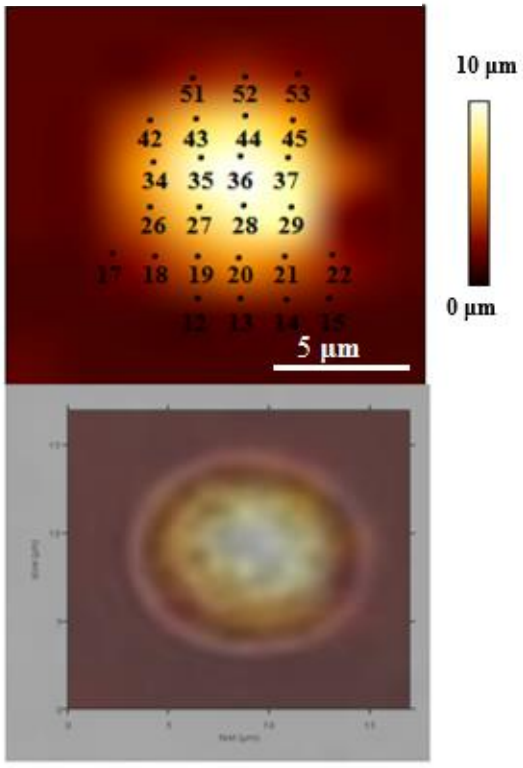

Number	Elastic Modulus (kPa)	Height (µm)
12	1.7	4.51
13	1.72	4.45
14	1.87	4.26
15	1.24	4.19
17	1.93	4.33
18	2.65	5.07
19	0.53	6.23
20	1.14	7.01
21	2.05	7.36
22	0.99	5.14
26	1.01	6.25
27	1.64	9.36
28	1.901	9.54
29	1.59	9.25
34	0.98	6.15
35	2.08	9.88
36	2.12	10
37	1.99	9.6
42	1.47	6.43
43	0.85	8.27
44	0.84	8.27
45	0.79	7.65
51	0.98	5.33
52	1.15	5.71
53	1.78	5.17

Figure 5-9. AFM images of the cells on the height channel (top images) and the overlayed images (bottom image) for each cell. The table beside each image provides information about the elastic modulus and height of each indentation location, which is indicated with each indentation number.

Referring to the images in Fig. 5-9, it can be observed that the greatest elastic modulus for each cell belongs to two different locations on the cells. The two locations are; (1) the edge of the cell, where they attached to the coating and they have minimum height, and (2), the higher parts of the cell, that is predicted to be the cell nucleus region. From the optical images of the cells, the nucleus inside each cell can be approximated. Overlaying the optical images with the AFM images clearly showed that the highest parts in the AFM image correspond to the cell nucleus region.

5.5.2 Study the Young's elastic modulus of nucleated and enucleated cells of day 14

In this section, further investigation into the effects of the cell nucleus region on the elastic modulus of the cells was performed. Cell samples were selected from day 14 of differentiation. Since the enucleation process for certain cells starts at day 14 of differentiation, it is expected that the cell culture media would be a mixture of nucleated and enucleated developing cord CD34+ stem cells. Applying the FACS method (see Chapter 4, section 4.1), day 14 cells were sorted into nucleated and enucleated groups (see Appendix A for the gating and sorting diagrams). Following this, twenty-five cells from each group were tested using the AFM for their elastic modulus, size and shape. Finally, the obtained results from each group were compared.

5.5.2.1 Elasticity measurements

For elastic modulus measurements, force mapping mode with a selected map size of 8×8 was used in all experiments. The force-displacement curves from each indentation were fitted with the Hertz-Sneddon model in order to calculate the Young's elastic modulus. The derived results from indenting nucleated and enucleated cells were collected and sorted into different elasticity ranges. The results were then plotted verses probability of the elasticity (Fig. 5-10). The results for the nucleated cells showed that there are three main peaks in the ranges of 0.71-0.8 kPa, 0.81-0.9 kPa and 0.91-1 kPa respectively. However, for the enucleated cells, most of the elastic distributions observed were in the ranges of 0.51-0.6 kPa and 0.41-0.5 kPa respectively. It is clear from the obtained results that the nucleated cells presented with more locations of higher elastic modulus than locations on enucleated cells. Therefore, while the only difference between the nucleated and enucleated cells was presence/absence of the nucleus, it can be suggested that the locations with higher elastic modulus on the nucleated cells are the nucleus region. Furthermore, graphs plotted for the elastic distributions for each cell were plotted

separately to understand if the obtained trend from all the cells can be seen in every single cell. Fig. 5-11 shows that the main peaks observed in Fig. 5-10, are observed in all single cells as well. Thus, there is a coherence between the results obtained from all the cells and every individual cell.

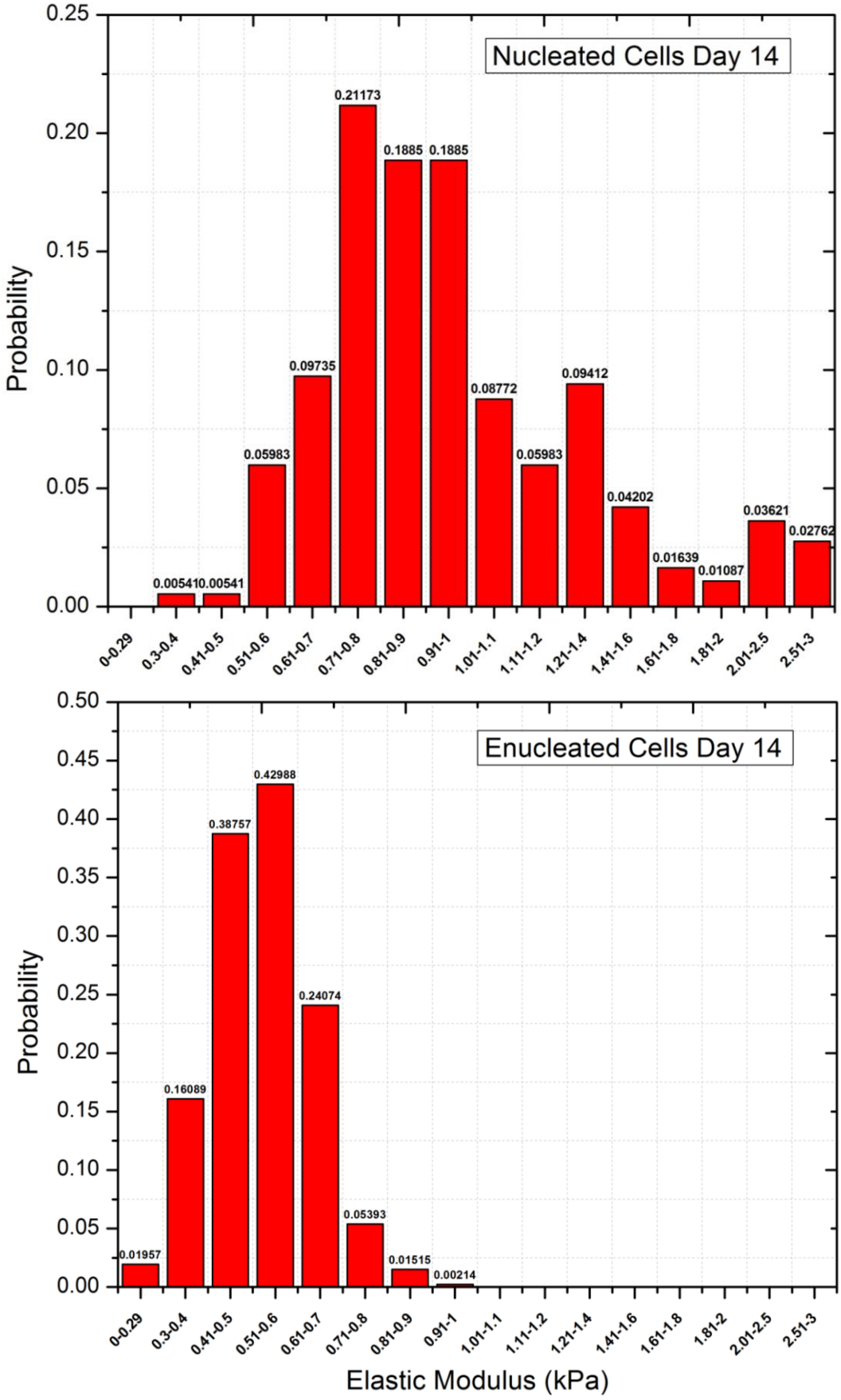

Figure 5-10. Probability distributions of the Young's elastic modulus for the nucleated and enucleated cells from day 14 of cell differentiation.

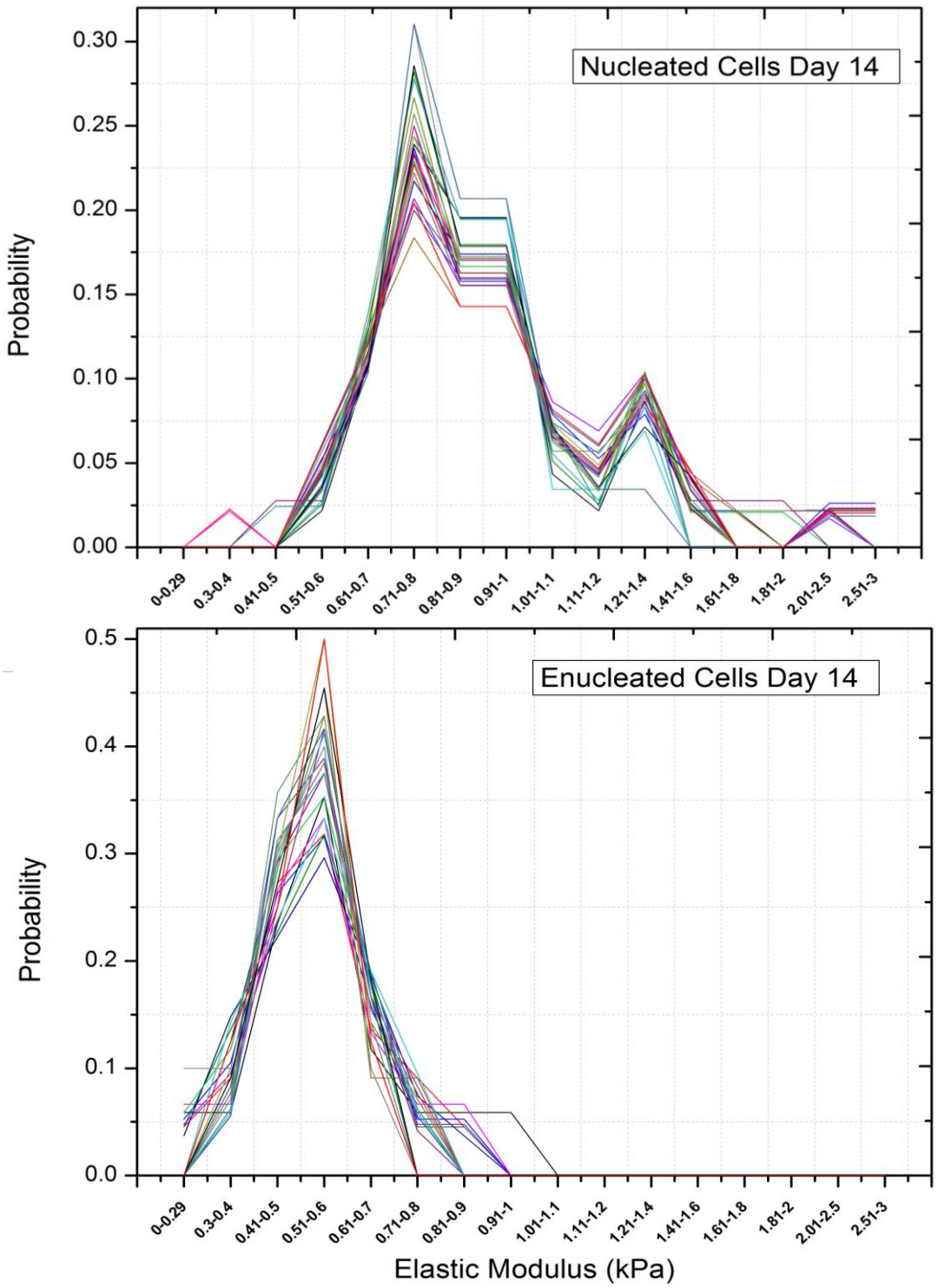

Figure 5-11. Probability distributions of the Young's elastic modulus for all twenty five nucleated cell and twenty five enucleated cell.

To compare and observe the effect of the enucleation process and/or presence of the cell nucleus on the derived elastic modulus of the cells, the obtained data from the nucleated and enucleated cells on day 14 of cell differentiation, along with the results derived from

a mixed culture of the cells on day 14 (see Chapter 4, section 4.3) were plotted together in Fig. 5-12.

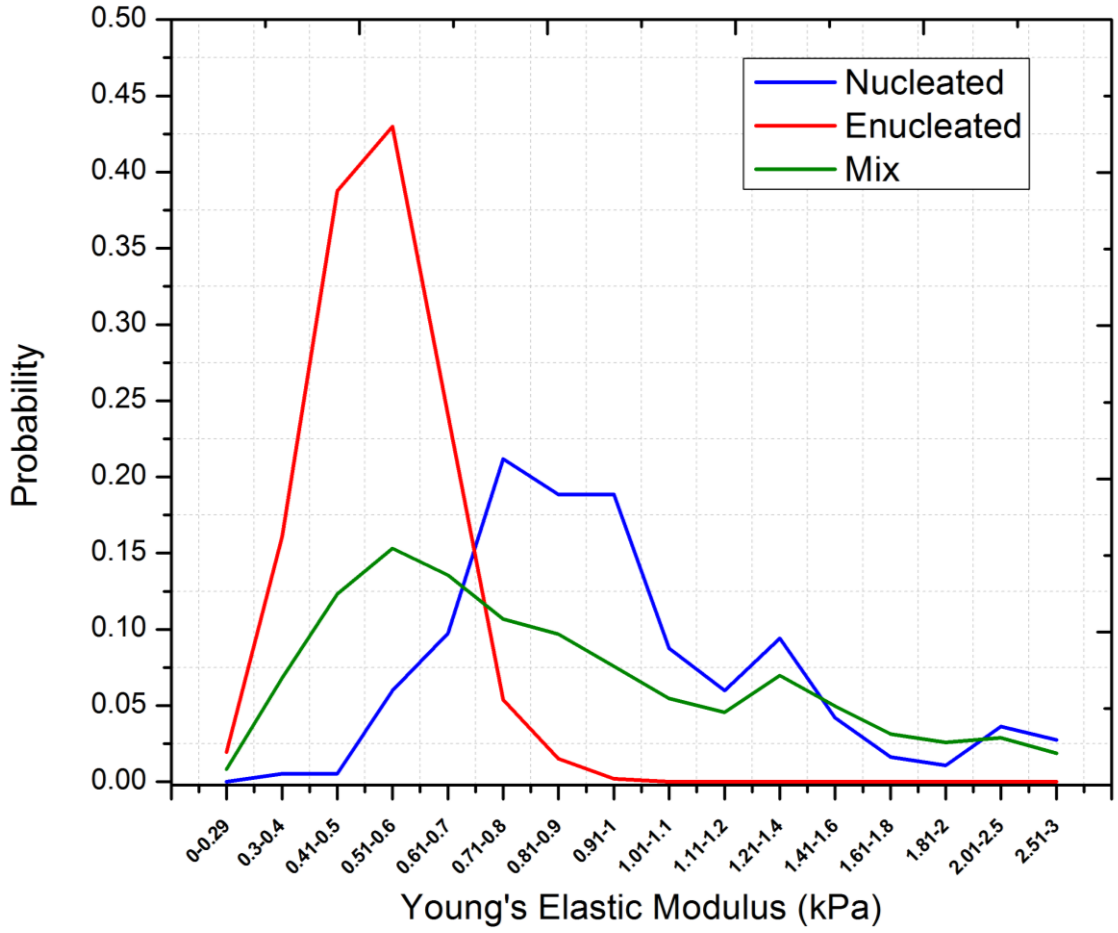

Figure 5-12. Probability distribution of the Young's elastic modulus derived from nucleated, enucleated and a mixture of nucleated and enucleated cells at day 14 of cell differentiation are compared.

Comparing the nucleated results curve with the culture mix results curve presented in Fig. 5-12, it can be noted that the stiffer section of the culture mix curve overlapped with that on the nucleated results curve. In contrast, the enucleated results curve is similar to the first section of the culture mix results curve, where the cells presented with a greater number of elastic indentation locations. Furthermore, for both enucleated and the culture mix cell samples, the main peaks of elastic modulus results were observed in the range of 0.51-0.6 kPa.

The median of the Young's elastic modulus for nucleated, enucleated and mix culture along with the nucleus are calculated by plotting the boxplot (Fig. 5-13). Values represent median ± SD (25 samples for nucleated and enucleated cells and 60 samples for the mixed culture and pyrenocytes). Therefore, the median elastic modulus for nucleated, enucleated, mixed and nuclei were calculated as 0.91 kPa, 0.54 kPa, 0.78 kPa and 5.89

kPa respectively. Also, obtained results from all cell groups are compared statistically by calculating the P-value. Statistical analysis showed that the measured Young's elastic modulus between nucleated and mix culture is not significant. However, the changes in the Young's elastic modulus between mixed and enucleated cells, nucleated and enucleated cells and all cell groups and nuclei is significant (***p<0.001, ****p < 0.0001).

(a)

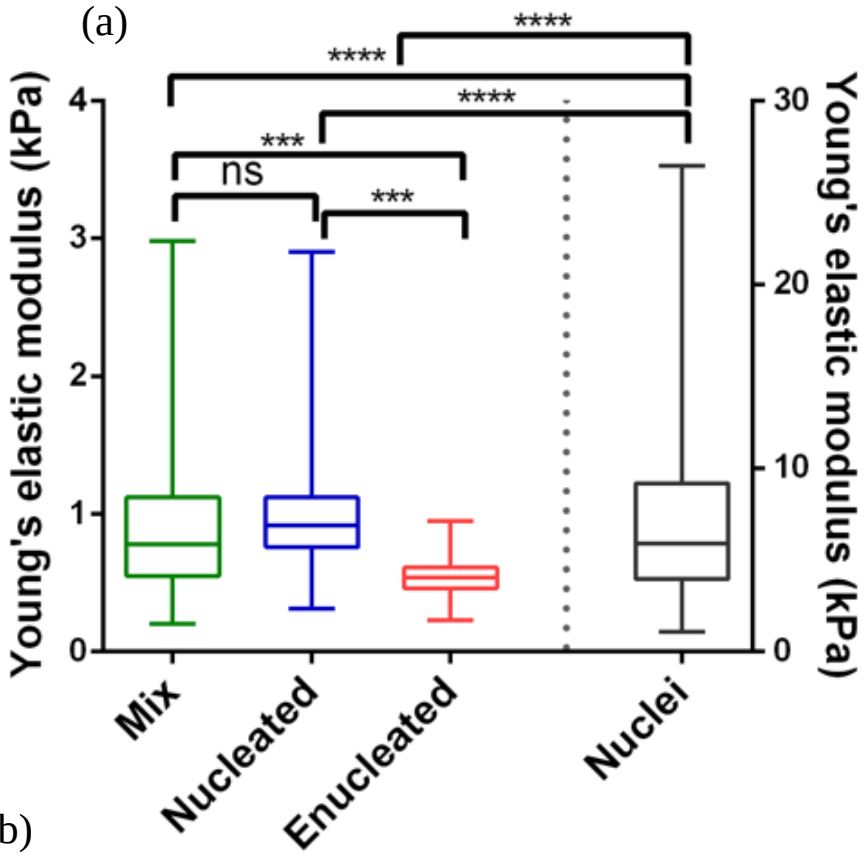

(b)

	Mix (kPa)	Nucleated (kPa)	Enucleated (kPa)	Nuclei (kPa)
Minimum	**0.204**	**0.31**	**0.23**	**1.08**
25% Percentile	**0.55**	**0.76**	**0.46**	**3.94**
Median	**0.78**	**0.915**	**0.54**	**5.89**
75% Percentile	**1.12**	**1.12**	**0.61**	**9.16**
Maximum	**2.98**	**2.9**	**0.95**	**26.47**
Mean	**0.91**	**1.04**	**0.54**	**6.88**
SD	**0.51**	**0.47**	**0.12**	**3.98**

Figure 5-13. (a) Boxplot to present the Young's elastic modulus of the sorted cells (nucleated and enucleated cells) from day 14 of differentiation process along with the mixed culture of the day 14 cells and nuclei (b) a table to summarise the derived data from lower and upper quartile with median and standard deviation.

For the next analysis, the derived results from the nucleated and enucleated cells were plotted together in Fig. 5-14. It can be seen that minimum Young's modulus derived for the nucleated cells is higher than the one measured for enucleated cells. This phenomena can be due to the presence/absence of the nucleus. Previous studies showed that for the CD34+ cells the nuclei occupy most of the cell volume. So, there is a high nuclear volume per cell volume ratio. Presence of a nucleus, changing characteristics and eventual expulsion throughout differentiation could contribute substantially to the overall cell mechanical behaviour [102]. Therefore, in the nucleated cells the location, which are not in the nucleus zone have higher elastic modulus compare to the same locations on the enucleated cell.

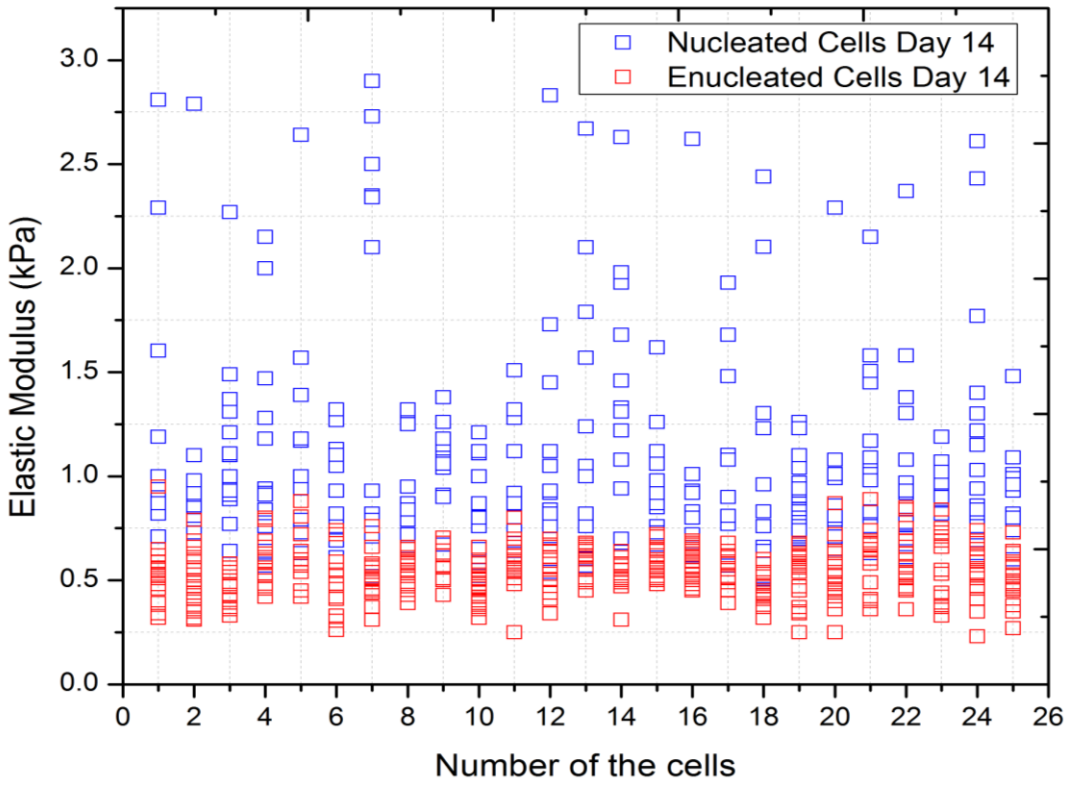

Figure 5-14. Elastic modulus distribution for each nucleated and enucleated cells from day 14 of differentiation process.

5.5.2.2 Size investigations

In this section, we investigated the size of the cells before and after the enucleation process. This study was designed in order to provide information about how cells from the same day of differentiation, can change in size based on the presence or absence of the nuclear organelle. Furthermore, the relationship between the elastic modulus of the nucleated and enucleated cells and their corresponding size was studied and compared.

A change in the size of the cells was studied by measuring the radius of twenty-five nucleated and twenty-five enucleated cells. For the size measurements, an optical image of every cell was taken before the elasticity indentation measurements. Following this, the "measure distance" function/tool on the AFM, was then used to measure and record the diameter of each cell from two different sides. Calculating the average of the measured diameter and dividing the result by two, resulted in the radius of each cell being determined.

Results from radius measurements of the cells were then analysed and plotted (Fig. 5-15). Measuring the radius of the nucleated cells showed that the radius of most of the cells lie in the range of ~ 4.5-5 μm and 4.0-4.5 μm respectively. Therefore, the average radius of the nucleated cells was calculated as 4.61 μm. Furthermore, referring to the radius measurements of the enucleated cells, most of the enucleated cells had a radius value in the range of ~ 5-5.5 μm. Therefore, the average value for the radius of enucleated cells was obtained as 5.21 μm. Based on the radius measurements, the radii measurements of the enucleated cells was on average 0.6 μm greater than the radius of the nucleated cells.

While the exact underlying cause of this difference is not completely clear, it could be explained by the effect of nucleus extrusion from the cells. Generally, during the enucleation process, the cell opens at one side. After the completion of the enucleation process, closure of the opened side takes some time, and the cell appears to be expanding from the opened side the where extrusion of nucleus has occurred.

The average cell radius from the mixed cell culture (see Chapter 4, section 4.4.1) was obtained as 4.54 μm. When comparing the mixed culture average radius with the average radius of the sorted cells, it can be suggested that most of the cells in the mixed culture were nucleated cells.

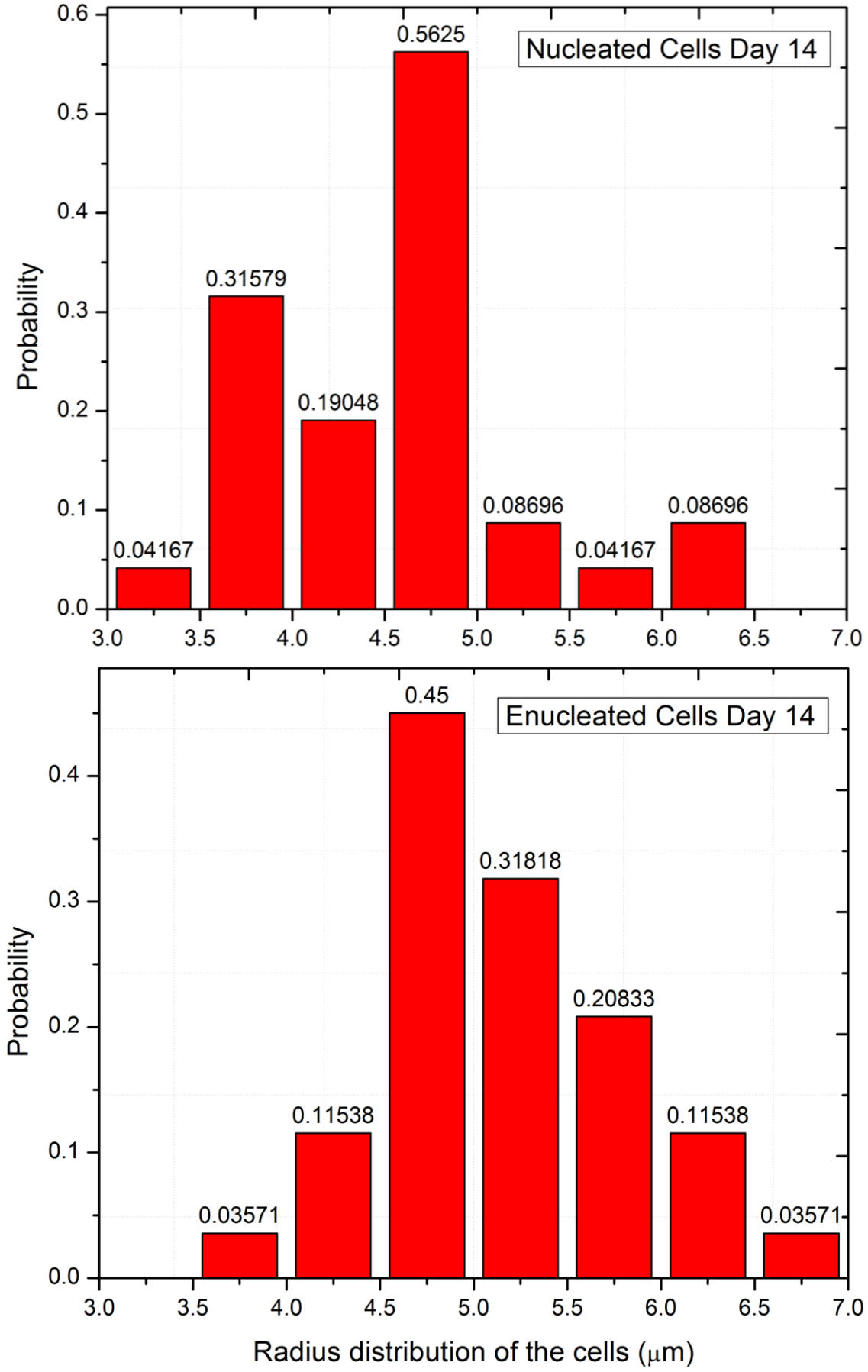

Figure 5-15. Radius distribution of the nucleated and enucleated cells.

For statistical analysis of the radius changes during the enucleation process the boxplot for the radius distribution of the nucleated and enucleated cells is plotted and P-value is calculated (Fig. 5-16). Also, the results from measuring the nucleus is included for comparison and sorting and separation purposes. The statistical studies showed that the change in the radius between the nucleated and enucleated cells is not significant. However, a significant difference between nucleated cells and nucleus and enucleated cells and nucleus is observed (****p < 0.0001).

(a)

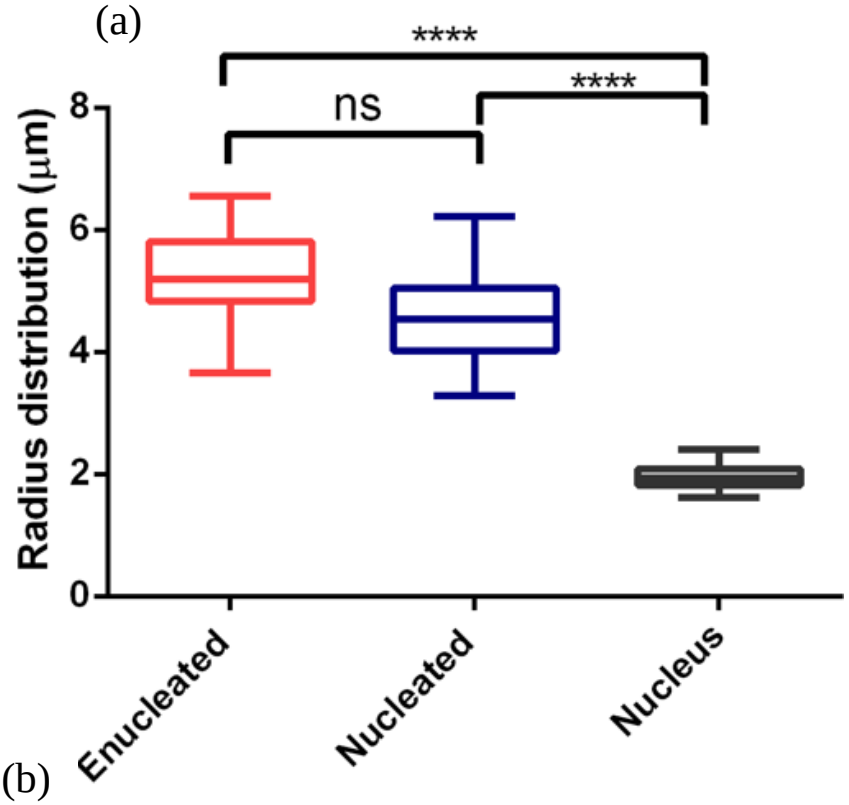

(b)

	Enucleated (μm)	Nucleated (μm)	Nucleus (μm)
Minimum	**3.66**	**3.29**	**1.62**
25% Percentile	**4.83**	**4.02**	**1.81**
Median	**5.19**	**4.53**	**1.94**
75% Percentile	**5.8**	**5.04**	**2.08**
Maximum	**6.55**	**6.22**	**2.405**
Mean	**5.27**	**4.61**	**1.95**
SD	**0.69**	**0.705**	**0.19**

Figure 5-16. (a) The radius distribution of the nucleated cells, enucleated cells and nucleus are presented using the boxplot (b) derived data from lower and upper quartile with median and standard deviation are summarised in the table.

To classify the nucleated, enucleated cells and nuclei in terms of elasticity and radius, ROC curves were plotted and the corresponding area under the curve (AUC) calculated (Fig. 5-17). Referring to Fig. 5-17 (a) as enucleated cells there is only 6% overlap with the nucleated cell population in terms of the elasticity (AUC=0.94). For the enucleated and nuclei the calculated AUC is equal to 1, which means there is no overlap between the enucleated cell population and nuclei (Fig. 5-17 (b)). In terms of radius classification, the enucleated cells have 24% overlap with the nucleated cells as the AUC=0.76 (Fig. 5-17 (c)). Also, for enucleated cells and nuclei the AUC for the radius is derived as 1, so no overlap between enucleated cells and nucleus is observed (Fig. 5-17 (d)).

Free-floating nuclei and undifferentiated cells constitute the two main contaminants that must be removed from the sample, prior to clinical application, to leave purified manufactured RBCs. Using these approaches it can be determined that enucleated cells are 100% separated (AUC=1) from the nuclei population in terms of elasticity and radius (Fig. 5-17 (b and d)). Therefore, elasticity and/or size based separation techniques can be applied safely. Also, for the enucleated and nucleated cell populations, comparing the elasticity (6%) and radius (24%) difference showed that the elasticity-based separation techniques can be more effective than the size-based techniques. However, elastic-based methods can remain small amount of contaminations while the size-based separation methods would be possible but contamination would be significant (Fig. 5-17 (a and c)).

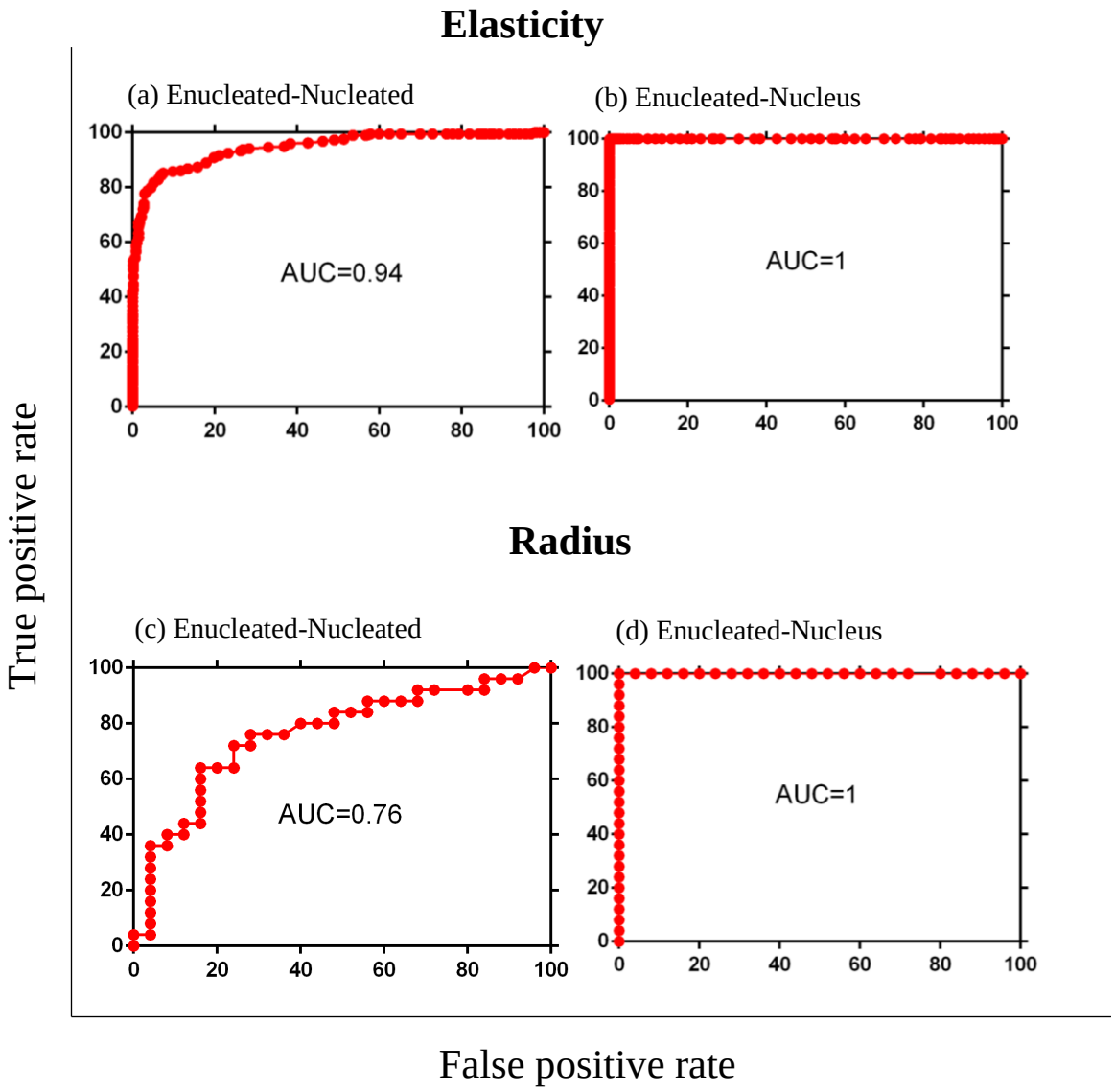

Figure 5-17. ROC curves were plotted for elasticity and radius for enucleated, nucleated and nucleus. The True Positive Rate is defined as the number of the enucleated cells (resp. nucleus) measured for a certain cut-off point (radius or elasticity) and divided by the total number of the enucleated cells (resp. nucleus). The False Positive Rate is the corresponding number of D11 cells (resp. nucleus) divided by the total number of the enucleated cells (resp. nucleus) for the same cut-off. The Area Under the Curve (AUC) was calculated to quantify the elasticity overlap between (a) enucleated and nucleated cells, (b) enucleated cells and nucleus, as well as radius overlap between (c) enucleated and nucleated cells, (d) enucleated cells and nucleus.

5.5.2.3 Shape investigations

Finally, to study the shape changes that occur in the nucleated and enucleated cells, the eccentricity of each cell was calculated. Eccentricity was calculated as described in Chapter 4, section 4.4. Cells with an eccentricity value equal to zero have a near perfect spherical shape. Thus, as the eccentricity value tends away from zero, it indicates that the shape of the cells has changed from a spherical shape to an oval shape.

The results obtained from calculating the eccentricity of the cells was plotted using the boxplot and presented in Fig. 5-18. Referring to Fig. 5-18, it can be noted that while the eccentricity of most of the nucleated and enucleated cells was close to a spherical shape, there were some enucleated cells with shape tending to more oval. Therefore, no significant shape changes were observed between the nucleated and enucleated cells. Observing no significant difference in the shape of the nucleated and enucleated cells also indicates that selecting sorting and separating techniques based on the elastic modulus of the cells are the best option.

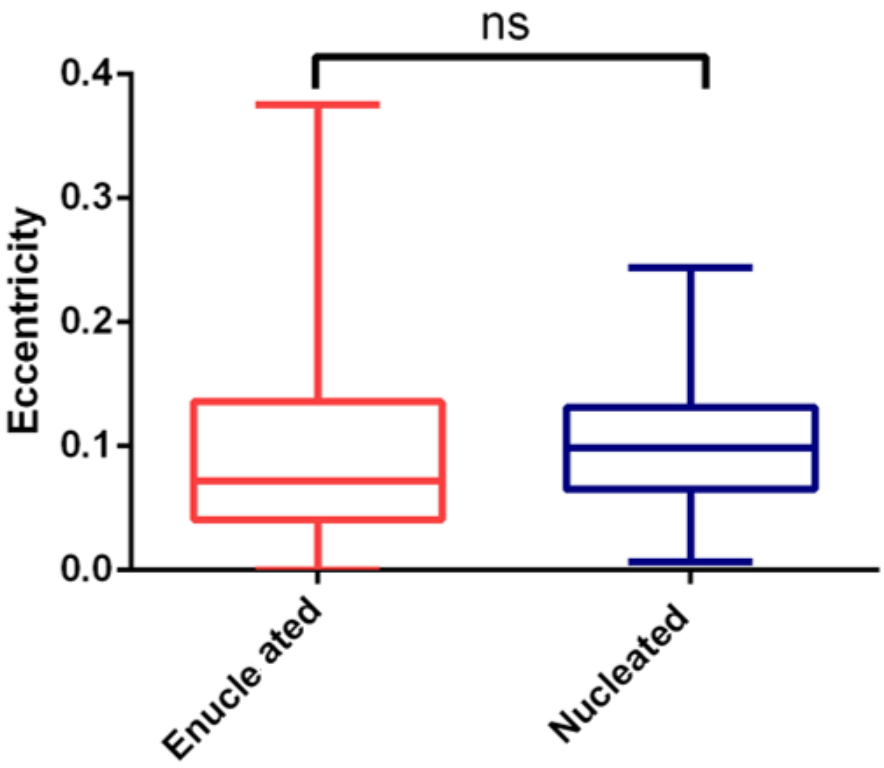

Figure 5-18. Derived eccentricity values of the sorted cells, obtained to study the shape changes between the nucleated and enucleated cells.

5.6 Concluding remarks

In this Chapter, we aimed to study the mechanical properties of pyrenocytes for the purpose of improving the manufactured cell sorting and separation applications. Furthermore, based on the works carried out in Chapter 4, this Chapter presented the quantitative work and results for day 11 of the umbilical cord blood CD34+ stem cells differentiation (nucleated cells) to study the relationship between the height and elasticity of the cells with the presence of the cell nucleus. Moreover, on day 14 of cell

differentiation, cells were sorted into nucleated and enucleated groups to investigate the relationship between the elastic modulus of the cells and the presence of the nucleus.

The following key conclusions of this chapter are highlighted below:

- Comparing the elastic properties of the pyrenocytes with the cord CD34+ cells at different stages of the differentiation process showed that the pyrenocytes are considerably stiffer than the cord CD34+ cells;
- Experiments showed that there is a direct relationship between time and elastic modulus of the pyrenocytes. As the time was passing the pyrenocytes showed more stiffness due to the degradation of the cytoplasmic layer around them;
- Size measurements showed that pyrenocytes are smaller than the cord CD34+ cells (e.g. the pyrenocytes are roughly 2 μm smaller than the reticulocytes);
- Obtained results from analysing the proerythroblasts, revealed that the higher and stiffer locations on the cells are the nucleus region;
- Results obtained from comparing day 14 sorted cells showed that the nucleated cells are stiffer than the enucleated cells. However, the enucleated cells were slightly larger than the nucleated cell.

The obtained results presented in this study could be applied to designing useful and more efficient cell sorting and separating techniques. As mentioned previously to provide a purified manufactured RBCs for the clinical applications it is important to remove the free-floating nuclei and undifferentiated cells as the two main contaminants from the culture media. Mechanical testing of the nucleus and sorted cells from day 14 of cell differentiation and further statistical analysis (boxplots and ROC curves) showed that there is a significant difference between the elastic modulus of the nucleated and enucleated cells and also these sorted cells with nucleus (Fig. 5-13). Moreover, the radius studies also showed that while there is no significant difference between the nucleated and enucleated cells radius, both groups are significantly different from the nucleus in terms of radius. Further analysis were performed using the ROC curve to clarify the elasticity and radius overlap of the nucleated and enucleated cells along with the enucleated and nucleus (Fig. 5- 17). Derived results revealed that to separate the free-floating nucleus from the enucleated cells elasticity and size-based techniques can provide a high efficient sorted culture since the obtained AUC was equal to 1 (100% separation). Yet, for sorting the enucleated and nucleated cells elasticity-based techniques can provide more pure culture since the overlap between the enucleated and nucleated

cells derived as 6% (AUC=0.94). In addition, the size-based methods for sorting the enucleated and nucleated cells cannot provide a highly purified/sorted culture and significant contaminations would be remained.

Furthermore, the provided results obtained from analysing the relationship between the nucleus of the cells with cells elastic modulus and heights, clearly demonstrated that the nuclear regions of the cells are the highest locations with the largest elastic modulus. These finding could also be used to identify nucleated cells from the enucleated ones in mixed cell cultures.

CHAPTER 6

Looking Back and Working Forward

Contents

6.1 looking back

As mentioned at the outset of this research thesis, the contribution and interplay between biological scientists and engineers has already led to significant improvements in clinical practice, specifically in areas such as diagnostics and therapy. Such multidisciplinary research projects continually aim at improving overall clinical therapies improving quality of life. The aim of this doctoral thesis is to continue such interdisciplinary contributions, by working in the field of modelling and quantifying events in cell mechanics for diagnostics and therapy, as well as cell sorting and separation techniques. In particular, the main aim is to investigate and develop an appropriate mathematical model in order to quantify the elastic properties of biological samples. Analysing the effect of external forces on size changes of biological cells - by applying the appropriate mathematical model - was another main aim of this thesis. Moreover, quantifying the mechanical and physical properties (elastic modulus, size and shape of biological cells) of umbilical cord blood CD34+ stem cells during their expansion and differentiation, as well as the processes for selecting/designing better cell purification and separation techniques was also a major objective of this thesis. Studying the mechanical and physical properties of umbilical cord blood CD34+ stem cells is closely linked to the presence of the cells' nucleus and the enucleation process (pyrenocyte extrusion). The final goal of this research was to study the mechanical and physical properties of pyrenocytes to understand their contributing effect on the elasticity of cord CD34+ cells. Furthermore, by utilising the obtained results from measuring the mechanical and physical properties

of pyrenocytes, selecting and improving a cell sorting purification and separation technique can be done more precisely and wisely.

The specific conclusions that have been made in this thesis are summarised as follows:

Chapter 3: Mechanical modelling of biological samples

- A mathematical model was developed to quantify the elastic properties of biological samples, based on the elastic shell theory. The thickness of the cell membrane, size changes and geometry of the tip were also considered in the model calculations;
- Size changes of the cells after indentation deformation due to an external force were measured, and reliable results were obtained;
- All results derived from calculating the Young's elastic modulus of cells using the developed contact mathematical model are from the surface lipid bilayer of the cells and are in the mega pascal range.

Comparing the obtained results from the developed model with the Hertz-Sneddon model showed that there is a significant difference in the Young's elastic modulus derived from each model. This difference is understandable due to the different nature of each model. Although, the Hertz-Sneddon model is widely applying to calculate the Young's elastic modulus of the biological samples, it cannot provide a precis results. However, it is an accurate model for calculating the Young's elastic modulus of the solid samples. Whilst, the newly developed model quantified the Young's elastic modulus of the lipid bilayer of the cells in the range as it was proposed previously in other researches. Also, it can provide acceptable information about changes in the size of the cells through cell development. Due to the complexity of the biological environment as cell undergo development, it is probable that the developed model has certain limitations. Consequently, the proposed methodology is seen to require more modifications to quantify the elastic properties of biological samples accurately.

Chapter 4: Investigation of the mechanical properties of umbilical cord blood CD34+ stem cells during their differentiation and maturation process for sorting and separating purposes

- First work, which aimed at quantifying the mechanical and physical properties of umbilical cord blood CD34+ stem cells during their maturation and differentiation process;
- Quantification of the mechanical and physical properties of the cells showed that the differentiation and enucleation process resulting in the cells presenting as more elastic and smaller in the size;
- The derived results could be applied to select and improve current cell sorting and separating methods.

In this chapter, the elastic modulus, size and shape changes of cord CD34+ cells were studied. The effect of maturation and differentiation on the physical and mechanical properties of cord CD34+ cells were also investigated. Due to the current high demand for donor RBCs, the *in vitro* study and production of these cells is increasing rapidly. Therefore, this study could provide useful information for selecting and improving proper purification and separation methods. To be able to use the manufactured RBCs for human donor transfusions, the applied sorting and separating techniques must be high yield with minimum drawback in order to obtain the healthiest desired/wanted cells. Therefore, cell physical sorting methods, which operate based on the elasticity and size of the cells, could be the right choice, as they could potentially decrease the extra processes and overall process time and cost associated with current cell sorting techniques. The results obtained in this chapter can be used as a reliable reference to select or design cell physical/mechanical sorting methods, purely based on the physical and mechanical characteristics of the cord CD34+ cells for both in-process and final product separation.

Chapter 5: Study on the mechanical and physical properties of pyrenocytes for understanding the effect of nucleus and enucleation process on mechanical properties of cord CD34+ stem cells

- First work done to quantify the mechanical and physical properties of pyrenocytes;
- Experiments were carried out to analyse the effect of the cells' nucleus and enucleation process on the elastic modulus of cord CD34+ cells;
- Derived results showed that pyrenocytes are significantly stiffer than cord CD34+ cells. Furthermore, size-wise the pyrenocytes are smaller than cord CD34+ cells;

- Studies on the effect of the nucleus and enucleation process on the elastic modulus of cord CD34+ cells, showed that nucleated cells are stiffer than the enucleated CD34+ cells;
- The results obtained from measuring the mechanical and physical properties of pyrenocytes, could be used for improving current cell purification and separation purposes.

Two main experimental objectives were carried out for this chapter. Firstly, the elastic properties, size and shape of pyrenocytes were measured. The obtained results can provide useful information, which along with the ones derived from the cord CD34+ cells in the previous chapters, could lead to improving current reticulocyte purification and separation methods. Secondly, the additional research was carried out in an attempt understand the effect of the nucleus and enucleation process on the mechanical properties of the cord CD34+ cells. The results here showed that the nucleated cells presented with a higher elastic modulus than enucleated cell, which were considerably softer. In addition, investigations on the effect of the nucleus on the elastic modulus of the cells clearly showed that the nucleus regions of the cells presented with the largest elastic modulus, as well as the greatest overall height. The results of this study could be used as a tool for the identification and purification of nucleated cells and enucleated in a mixed culture using the elasticity-based techniques. Also, free-floating nucleus can be separated from the culture media using elasticity and/or size based methods.

6.1.1 Limitations

There are limitations to take in to consideration however, beginning with the mechanical modelling of biological samples, the model developed based on the information can be obtained from the AFM measurements. Therefore, for example for calculating the bending energy the obtained data from the AFM, only shows the bending in the z-direction and data for bending in the vertical direction is missing. Also, the adhesion force between the tip and the sample is neglected, which in reality cells have viscoelastic behaviour rather than the elastic behaviour. Moreover, the developed model is highly tip shape dependent and it required to modify for all different shapes of tips.

Regarding to the mechanical measurements of CD34+ cells and pyrenocytes, derived elastic modulus is directly dependent to the geometry of the tip. The tip geometry can have a significant effect on the derived value for the Young's elastic modulus from force-indentation curves even if all other experimental conditions are kept constant. It is

therefore important that when comparing elasticity values from the literature or from previous experiments that this be taken in to consideration. This can explain the reason of the wide range of values published for elasticity of various cell types. In the work presented here, conical indenters were chosen to provide more information about the elastic modulus of the cells by indenting them at more points (different locations on the cells). In addition, all the prepared CD34+ cells and pyrenocytes for the elastic measurements are attached to the petri dish using the PDL. Although as it discussed in Chapter 2 section 2.2.2 low concentration of PDL does not effect on the elastic properties of the cell, the elastic behaviour of the attached cells is different from the free floating cells. Since, the mechanical testing of the CD34+ cells are regarding to produce the manufactured RBCs for clinical applications, it is necessary to consider the abovementioned limitation. Also, the shear stress exposed on the cells in the lab condition is different from the shear stress in the body, which means that cells need to be elastic enough to resist this stress without bursting or rupturing. Therefore, this needs to take into consideration when cells are preparing for the human applications.

6.2 Working forward

Based on the outcome of this thesis research project, the results presented show great promise and scope for future investigations. Specifically, the results presented could help improve the methods and techniques currently used for mechanical studies on soft biological samples. The following works are proposed for future investigations to advance this thesis into greater depth for biological mechanical measurements;

Further investigations in mathematical modelling of mammalian cells:

The work presented in Chapter 3 was formulated and based on developing the elastic shell theory for a conical indenter, to calculate the Young's elastic modulus of mammalian cells. Although the results derived from the model were in an acceptable range, there are still some extra works/modifications that can be done to improve the model, namely;

(1) **Modifications on the model for obtaining better fit:** it worth to do further investigations to modify the developed model by changing the variables in the equations to get the better fitting curve.
(2) **Bending energy:** To develop the new model it is assumed that bending energy is quite smaller than the stretching energy and therefore it is neglected from calculations. However, in reality, bending happens in the deformed area. For

further investigations, it will be worth investigating if the bending energy is relevant by including it in the calculations.

(3) Geometry of the tip: It has been shown that elasticity and size calculations are geometry dependant. Therefore, the current calculations can be updated for other indenter geometries such as cylindrical and triangular tips.

Further investigations related to *in vitro* production of RBCs:

Considering the effect of biological changes on the mechanical properties of cells: In Chapter 4, the mechanical and physical properties of the umbilical cord blood CD34+ stem cells during their expansion and maturation process are quantified. It discussed that most of the changes in the cells can be related to the effect and presence of the cell's nucleus and enucleation process. However, it is possible that numerous biological changes during the differentiation process have an effect on the elastic properties of the cells. For example, testing the cells for changes in the structure of the intracellular actin cytoskeleton and also, changes in the size of the organelles and elimination of them during the differentiation process could provide valuable information about the effect that biological changes have on the mechanical properties of cells.

Comparing the mechanical and physical properties of manufactured reticulocytes with primary donor derived RBCs: Since the aim of producing manufactured reticulocytes is for attempting alleviate the current shortage of donated RBCs for human transfusion, it is important to understand the difference between the mechanical and physical properties of manufactured cells with donor derived primary RBC. Since RBCs are responsible for transporting and transferring oxygen in the body, they must be elastic enough to be able to pass through the veins and capillaries in the body. Comparing the elastic properties of manufactured cells with primary RBCs will provide useful information about the feasibility of using manufactured RBCs for donor cell transfusion with respect to how the mechanical properties of the cells is affected during the *in vitro* production process. Manufactured RBCs need to not only mimic the biological and gaseous exchange functions of RBCs, but they also need to function and respond to the physical events that occur as RBCs move through the veins and capillaries of the body. For example, if the manufactured RBCs are softer than the donor primary RBCs, they could have the capacity to deform more easily through capillaries and transfer more oxygen to the target organs in the body. In contrast, stiffer manufactured RBCs, could result in a reduced rate of oxygen delivery and diffusion to target organs, with stiffer less

deformable cells taking longer to move through the bodies' veins and capillaries. Therefore, comparing the elastic modulus of manufactured RBCs to donor primary RBCs will demonstrate what optimal physical properties are required to allow for appropriate cell deformation and optimal oxygen delivery to target organs. This could be used to validate the applicability of the manufactured cells for human transfusion.

Further investigations on the pyrenocytes:

Study the biological changes in pyrenocytes: The effect of time on the elastic properties of pyrenocytes was discussed in Chapter 5. However, the exact underlying cause for the changes was not investigated. Therefore, as there has been much research carried out investigating the mechanical properties of pyrenocytes, additional studies on the biological changes in pyrenocytes with respect to the effect of time, could provide useful information, which could be used in designing and improving the current cell purification and separation techniques.

References

1. Binnig, G., C.F. Quate, and C. Gerber, *Atomic Force Microscope.* Physical Review Letters, 1986. **56**(9): p. 930-933.
2. Binnig, G. and H. Rohrer, *Scanning tunneling microscopy.* Surface science, 1983. **126**(1): p. 236-244.
3. Braet, F., et al., *Comparison of fixed and living liver endothelial cells by atomic force microscopy.* Applied Physics A: Materials Science & Processing, 1998. **66**: p. S575-S578.
4. Le Grimellec, C., et al., *Imaging of the surface of living cells by low-force contact-mode atomic force microscopy.* Biophysical journal, 1998. **75**(2): p. 695-703.
5. Kuznetsova, T.G., et al., *Atomic force microscopy probing of cell elasticity.* Micron, 2007. **38**(8): p. 824-833.
6. Senapati, S. and S. Lindsay, *Recent Progress in Molecular Recognition Imaging Using Atomic Force Microscopy.* Accounts of chemical research, 2016. **49**(3): p. 503-510.
7. Powell, L., N. Hilal, and C. Wright, *Atomic force microscopy study of the biofouling and mechanical properties of virgin and industrially fouled reverse osmosis membranes.* Desalination, 2017. **404**: p. 313-321.
8. Hilal, N., et al., *A Review of Atomic Force Microscopy Applied to Cell Interactions with Membranes.* Chemical Engineering Research and Design, 2006. **84**(4): p. 282-292.
9. Richard Bowen, W., et al., *Visualisation of an ultrafiltration membrane by non-contact atomic force microscopy at single pore resolution.* Journal of Membrane Science, 1996. **110**(2): p. 229-232.
10. Barrow, M.S., et al., *A study of the tensile properties of liquids in confined spaces using an atomic force microscope.* Proceedings of the Royal Society of London. Series A: Mathematical, Physical and Engineering Sciences, 2003. **459**(2039): p. 2885-2908.
11. Thomas, G., et al., *Measuring the mechanical properties of living cells using atomic force microscopy.* J Vis Exp, 2013(76).
12. Mozafari, M.R., et al., *A review of scanning probe microscopy investigations of liposome-DNA complexes.* J Liposome Res, 2005. **15**(1-2): p. 93-107.
13. Alessandrini, A. and P. Facci, *AFM: a versatile tool in biophysics.* Measurement science and technology, 2005. **16**(6): p. R65.

14. Charras, G., P.P. Lehenkari, and M. Horton, *Atomic force microscopy can be used to mechanically stimulate osteoblasts and evaluate cellular strain distributions.* Ultramicroscopy, 2001. **86**(1): p. 85-95.

15. Ando, T., et al., *High-speed AFM and nano-visualization of biomolecular processes.* Pflügers Archiv-European Journal of Physiology, 2008. **456**(1): p. 211-225.

16. Seo, Y. and W. Jhe, *Atomic force microscopy and spectroscopy.* Reports on Progress in Physics, 2007. **71**(1): p. 016101.

17. Alonso, J.L. and W.H. Goldmann, *Feeling the forces: atomic force microscopy in cell biology.* Life sciences, 2003. **72**(23): p. 2553-2560.

18. Prater, C., et al., *Tappingmode imaging applications and technology.* Digital Instruments Nanonotes, Santa Barbara, California, USA, 1995.

19. Friedbacher, G. and H. Fuchs, *Classification of scanning probe microscopies.* Pure and applied chemistry, 1999. **71**(7): p. 1337-1357.

20. Kumar, S. and V.M. Weaver, *Mechanics, malignancy, and metastasis: the force journey of a tumor cell.* Cancer and Metastasis Reviews, 2009. **28**(1-2): p. 113-127.

21. Guck, J., et al., *Optical deformability as an inherent cell marker for testing malignant transformation and metastatic competence.* Biophysical journal, 2005. **88**(5): p. 3689-3698.

22. Rotsch, C. and M. Radmacher, *Drug-Induced Changes of Cytoskeletal Structure and Mechanics in Fibroblasts: An Atomic Force Microscopy Study.* Biophysical Journal, 2000. **78**(1): p. 520-535.

23. *Data processing software manual, JPK instruments, version 4.2*. 2012.

24. Butt, H.-J. and M. Jaschke, *Calculation of thermal noise in atomic force microscopy.* Nanotechnology, 1995. **6**(1): p. 1.

25. Hertz, H., *über die berührung fester elastischer körper.* Journal fur die Reine und Angewandte Mathematik, 1881. **92**: p. 156-171.

26. Johnson, K.L., *Contact mechanics*. 1987: Cambridge university press.

27. Sneddon, I.N., *The relation between load and penetration in the axisymmetric boussinesq problem for a punch of arbitrary profile.* International Journal of Engineering Science, 1965. **3**(1): p. 47-57.

28. Johnson, K.L., K. Kendall, and A.D. Roberts, *Surface Energy and the Contact of Elastic Solids.* Proceedings of the Royal Society of London. A. Mathematical and Physical Sciences, 1971. **324**(1558): p. 301-313.

29. Derjaguin, B., V. Muller, and Y.P. Toporov, *Effect of contact deformations on the adhesion of particles.* Journal of Colloid and interface science, 1975. **53**(2): p. 314-326.

30. Lin, D.C., E.K. Dimitriadis, and F. Horkay, *Robust strategies for automated AFM force curve analysis—II: adhesion-influenced indentation of soft, elastic materials.* Journal of biomechanical engineering, 2007. **129**(6): p. 904-912.

31. Mahaffy, R.E., et al., *Quantitative Analysis of the Viscoelastic Properties of Thin Regions of Fibroblasts Using Atomic Force Microscopy.* Biophysical journal, 2004. **86**(3): p. 1777-1793.

32. Tabor, D., *A simple theory of static and dynamic hardness.* Proceedings of the Royal Society of London. Series A. Mathematical and Physical Sciences 1948. **192**(1029): p. 247-274.

33. Popov, V., *Contact mechanics and friction: physical principles and applications*. 2010: Springer Science & Business Media.

34. Ladjal, H., et al. *Atomic force microscopy-based single-cell indentation: Experimentation and finite element simulation*. in *Intelligent Robots and Systems, 2009. IROS 2009. IEEE/RSJ International Conference on*. 2009.

35. Libai, A. and J.G. Simmonds, *The nonlinear theory of elastic shells*. 2005: Cambridge university press.

36. Dikmen, M., *The general theory of thin elastic shells.* International Journal of Engineering Science, 1979. **17**(3): p. 235-250.

37. Turner, C.E., *Introduction to plate and shell theory*. 1965: Longman, 1965.

38. Altenbach, H. and P.A. Zhilin, *The theory of simple elastic shells*, in *Theories of Plates and Shells*. 2004, Springer. p. 1-12.

39. Lulevich, V.V., D. Andrienko, and O.I. Vinogradova, *Elasticity of polyelectrolyte multilayer microcapsules.* The Journal of chemical physics, 2004. **120**: p. 3822.

40. González-Cruz, R.D., V.C. Fonseca, and E.M. Darling, *Cellular mechanical properties reflect the differentiation potential of adipose-derived mesenchymal stem cells.* Proceedings of the National Academy of Sciences, 2012. **109**(24): p. E1523-E1529.

41. Starodubtseva, M.N., *Mechanical properties of cells and ageing.* Ageing Research Reviews, 2011. **10**(1): p. 16-25.

42. Darling, E.M., et al., *A thin-layer model for viscoelastic, stress-relaxation testing of cells using atomic force microscopy: do cell properties reflect metastatic potential?* Biophysical journal, 2007. **92**(5): p. 1784-1791.

43. Schanila, N., et al., *Cell Visco-Elasticity Measured with AFM and Optical Trapping at Sub-Micrometer Deformations.* PLoS ONE, 2012. **7**(9).

44. Clark, A.G. and E. Paluch, *Mechanics and regulation of cell shape during the cell cycle.* Results Probl Cell Differ, 2011. **53**: p. 31-73.

45. Collinsworth, A.M., et al., *Apparent elastic modulus and hysteresis of skeletal muscle cells throughout differentiation.* Am J Physiol Cell Physiol, 2002. **283**(4): p. C1219-27.

46. Lu, Y.-B., et al., *Viscoelastic properties of individual glial cells and neurons in the CNS.* Proceedings of the National Academy of Sciences, 2006. **103**(47): p. 17759-17764.

47. Lekka, M., et al., *Elasticity of normal and cancerous human bladder cells studied by scanning force microscopy.* Eur Biophys J, 1999. **28**(4): p. 312-6.

48. Rosenbluth, M.J., W.A. Lam, and D.A. Fletcher, *Force microscopy of nonadherent cells: a comparison of leukemia cell deformability.* Biophys J, 2006. **90**(8): p. 2994-3003.

49. Mathur, A.B., G.A. Truskey, and W.M. Reichert, *Atomic force and total internal reflection fluorescence microscopy for the study of force transmission in endothelial cells.* Biophysical Journal, 2000. **78**(4): p. 1725-1735.

50. Sato, M., et al., *Local mechanical properties measured by atomic force microscopy for cultured bovine endothelial cells exposed to shear stress.* J Biomech, 2000. **33**(1): p. 127-35.

51. Takai, E., et al., *Osteoblast elastic modulus measured by atomic force microscopy is substrate dependent.* Ann Biomed Eng, 2005. **33**(7): p. 963-71.

52. Kiss, R., et al., *Elasticity of human embryonic stem cells as determined by atomic force microscopy.* J Biomech Eng, 2011. **133**(10): p. 101009.

53. Zhang, J.S., W.E. Kraus, and G.A. Truskey, *Stretch-induced nitric oxide modulates mechanical properties of skeletal muscle cells.* Am J Physiol Cell Physiol, 2004. **287**(2): p. C292-9.

54. Mathur, A.B., et al., *Endothelial, cardiac muscle and skeletal muscle exhibit different viscous and elastic properties as determined by atomic force microscopy.* J Biomech, 2001. **34**(12): p. 1545-53.

55. Dulińska, I., et al., *Stiffness of normal and pathological erythrocytes studied by means of atomic force microscopy.* Journal of Biochemical and Biophysical Methods, 2006. **66**(1–3): p. 1-11.

56. Yamane, Y., et al., *Quantitative analyses of topography and elasticity of living and fixed astrocytes.* J Electron Microsc (Tokyo), 2000. **49**(3): p. 463-71.

57. Laurent, V.M., et al., *Gradient of Rigidity in the Lamellipodia of Migrating Cells Revealed by Atomic Force Microscopy.* Biophysical journal, 2005. **89**(1): p. 667-675.

58. Radmacher, M., et al., *Measuring the viscoelastic properties of human platelets with the atomic force microscope.* Biophysical Journal, 1996. **70**(1): p. 556-567.

59. Rotsch, C., et al., *AFM imaging and elasticity measurements on living rat liver macrophages.* Cell Biol Int, 1997. **21**(11): p. 685-96.

60. Tolomeo, J.A., C.R. Steele, and M.C. Holley, *Mechanical properties of the lateral cortex of mammalian auditory outer hair cells.* Biophysical Journal, 1996. **71**(1): p. 421-429.

61. Costa, K.D., *Single-cell elastography: probing for disease with the atomic force microscope.* Disease markers, 2004. **19**(2-3): p. 139-154.

62. Zhou, J. and I. Papautsky, *Fundamentals of inertial focusing in microchannels.* Lab on a Chip, 2013. **13**(6): p. 1121-1132.

63. Connon, C.J., *Bioprocessing for Cell-Based Therapies*. 2016: John Wiley & Sons.

64. *Risks of a blood transfusion* 2015; Available from: http://www.nhs.uk/Conditions/Blood-transfusion/Pages/Risks.aspx.

65. Hur, S.C., et al., *Deformability-based cell classification and enrichment using inertial microfluidics.* Lab on a Chip, 2011. **11**(5): p. 912-920.

66. Morita, H., et al., *Cytokine production by the murine macrophage cell line J774. 1 after exposure to lactobacilli.* Bioscience, biotechnology, and biochemistry, 2002. **66**(9): p. 1963-1966.

67. Lu, S.-J., et al., *Biologic properties and enucleation of red blood cells from human embryonic stem cells.* Blood, 2008. **112**(12): p. 4475-4484.

68. *Poly-D-lysine hydrobromide*. 2016; Available from: http://www.sigmaaldrich.com/catalog/product/sigma/p6407?lang=en&region=GB.

69. Lu, H., et al., *Effects of poly(L-lysine), poly(acrylic acid) and poly(ethylene glycol) on the adhesion, proliferation and chondrogenic differentiation of human mesenchymal stem cells.* J Biomater Sci Polym Ed, 2009. **20**(5-6): p. 577-89.

70. Li, M., et al., *Atomic force microscopy imaging and mechanical properties measurement of red blood cells and aggressive cancer cells.* Sci China Life Sci, 2012. **55**(11): p. 968-73.

71. Landau, L.D. and E.M. Lifshitz, *Course of Theoretical Physics Vol 7: Theory and Elasticity*. 1959: Pergamon Press.

72. Moreno-Flores, S., et al., *Stress relaxation and creep on living cells with the atomic force microscope: a means to calculate elastic moduli and viscosities of cell components.* Nanotechnology, 2010. **21**(44): p. 445101.

73. Kuptsov, L.P., *"Einstein rule" in Hazewinkel, Michiel, Encyclopedia of Mathematics*. 2001: Springer

74. Sackmann, E., *Membrane bending energy concept of vesicle- and cell-shapes and shape-transitions.* FEBS Letters, 1994. **346**(1): p. 3-16.

75. Picas, L., F. Rico, and S. Scheuring, *Direct measurement of the mechanical properties of lipid phases in supported bilayers.* Biophys J, 2012. **102**(1): p. L01-3.

76. Lam, J., et al., *Baseline mechanical characterization of J774 macrophages.* Biophysical journal, 2009. **96**(1): p. 248-254.

77. Souza, S.T., et al., *Macrophage adhesion on fibronectin evokes an increase in the elastic property of the cell membrane and cytoskeleton: an atomic force microscopy study*. Eur Biophys J, 2014. **43**(12): p. 573-9.

78. Sjöstrand, F.S., *A comparison of plasma membrane, cytomembranes, and mitochondrial membrane elements with respect to ultrastructural features.* Journal of ultrastructure research, 1963. **9**(5): p. 561-580.

79. Nishi, D., et al. *Measurement of the mechanical properties of living cell using micro hand and developed AFM system*. in *2005 IEEE/RSJ International Conference on Intelligent Robots and Systems*. 2005.

80. Et-Thakafy, O., et al., *Mechanical Properties of Membranes Composed of Gel-Phase or Fluid-Phase Phospholipids Probed on Liposomes by Atomic Force Spectroscopy.* Langmuir, 2017.

81. Mason, C. and P. Dunnill, *Assessing the value of autologous and allogeneic cells for regenerative medicine.* Regenerative medicine, 2009. **4**(6): p. 835-853.

82. Mountford, J.C. and M. Turner, *In vitro production of red blood cells.* Transfusion and Apheresis Science, 2011. **45**(1): p. 85-89.

83. Baek, E.J., et al., *In vitro clinical-grade generation of red blood cells from human umbilical cord blood CD34+ cells.* Transfusion, 2008. **48**(10): p. 2235-2245.

84. Giarratana, M.-C., et al., *Proof of principle for transfusion of in vitro–generated red blood cells.* Blood, 2011. **118**(19): p. 5071-5079.

85. Mittra, J., et al., *Identifying viable regulatory and innovation pathways for regenerative medicine: a case study of cultured red blood cells.* N Biotechnol, 2015. **32**(1): p. 180-90.

86. Huang, L.R., et al., *Continuous particle separation through deterministic lateral displacement.* Science, 2004. **304**(5673): p. 987-90.

87. Yamada, M., M. Nakashima, and M. Seki, *Pinched flow fractionation: continuous size separation of particles utilizing a laminar flow profile in a pinched microchannel.* Anal Chem, 2004. **76**(18): p. 5465-71.

88. Sajeesh, P. and A.K. Sen, *Particle separation and sorting in microfluidic devices: a review.* Microfluidics and nanofluidics, 2014. **17**(1): p. 1-52.

89. Darling, E.M. and D. Di Carlo, *High-Throughput Assessment of Cellular Mechanical Properties.* Annu Rev Biomed Eng, 2015. **17**: p. 35-62.

90. Warkiani, M.E., et al., *Slanted spiral microfluidics for the ultra-fast, label-free isolation of circulating tumor cells.* Lab Chip, 2014. **14**(1): p. 128-37.

91. Miller, B., M. Jimenez, and H. Bridle, *Cascading and Parallelising Curvilinear Inertial Focusing Systems for High Volume, Wide Size Distribution, Separation and Concentration of Particles.* 2016. **6**: p. 36386.

92. Nathamgari, S.S.P., et al., *Isolating single cells in a neurosphere assay using inertial microfluidics.* Lab on a chip, 2015. **15**(24): p. 4591-4597.

93. Martel, J.M. and M. Toner, *Inertial focusing dynamics in spiral microchannels.* Physics of Fluids (1994-present), 2012. **24**(3): p. 032001.

94. Hou, H.W., et al., *Deformability based cell margination—a simple microfluidic design for malaria-infected erythrocyte separation.* Lab on a Chip, 2010. **10**(19): p. 2605-2613.

95. Faivre, M., et al., *Geometrical focusing of cells in a microfluidic device: an approach to separate blood plasma.* Biorheology, 2006. **43**(2): p. 147-159.

96. Sajeesh, P., et al., *Characterization and sorting of cells based on stiffness contrast in a microfluidic channel.* RSC Advances, 2016. **6**(78): p. 74704-74714.

97. Keerthivasan, G., A. Wickrema, and J.D. Crispino, *Erythroblast enucleation.* Stem cells international, 2011. **2011**.

98. Hebiguchi, M., et al., *Dynamics of human erythroblast enucleation.* International journal of hematology, 2008. **88**(5): p. 498-507.

99. Bouhassira, E.E., *Toward the manufacture of red blood cells?* Blood, 2008. **112**(12): p. 4362-4363.

100. Migliaccio, A.R., *Erythroblast enucleation.* Haematologica, 2010. **95**(12): p. 1985-1988.

101. Di Carlo, D., et al., *Equilibrium separation and filtration of particles using differential inertial focusing.* Analytical chemistry, 2008. **80**(6): p. 2204-2211.

102. Ribeiro, A.S. and K.N. Dahl, *The nucleus as a central structure in defining the mechanical properties of stem cells.* Conf Proc IEEE Eng Med Biol Soc, 2010. **2010**: p. 831-4.

103. Chen, K., et al., *Resolving the distinct stages in erythroid differentiation based on dynamic changes in membrane protein expression during erythropoiesis.* Proceedings of the National Academy of Sciences, 2009. **106**(41): p. 17413-17418.

104. Lloyd, Alison C., *The Regulation of Cell Size.* Cell, 2013. **154**(6): p. 1194-1205.

105. Olivier, E.N., et al., *Large-scale production of embryonic red blood cells from human embryonic stem cells.* Experimental hematology, 2006. **34**(12): p. 1635-1642.

106. Carl, P. and H. Schillers, *Elasticity measurement of living cells with an atomic force microscope: data acquisition and processing.* Pflügers Archiv-European Journal of Physiology, 2008. **457**(2): p. 551-559.

107. Nakamura, Y., *In vitro production of transfusable red blood cells.* Biotechnology and Genetic Engineering Reviews, 2008. **25**(1): p. 187-202.